Laser-Based High-Voltage Metrology with ppm Accuracy

Laserbasierte Hochspannungsmetrologie mit ppm Genauigkeit
Zur Erlangung des Grades eines Doktors der Naturwissenschaften (Dr. rer. nat.)
genehmigte Dissertation von Kristian Lars König aus Bad Nauheim
Tag der Einreichung: 13.11.2018, Tag der Prüfung: 10.12.2018
Darmstadt — D 17

1. Gutachten: Prof. Dr. Wilfried Nörtershäuser
2. Gutachten: Prof. Dr. Thorsten Kröll

TECHNISCHE
UNIVERSITÄT
DARMSTADT

Fachbereich Physik
Institut für Kernphysik
AG W. Nörtershäuser

LASER
SpHERe

ALIVE

Laser-Based High-Voltage Metrology with ppm Accuracy
Laserbasierte Hochspannungsmetrologie mit ppm Genauigkeit

Genehmigte Dissertation von Kristian Lars König aus Bad Nauheim

1. Gutachten: Prof. Dr. Wilfried Nörtershäuser
2. Gutachten: Prof. Dr. Thorsten Kröll

Tag der Einreichung: 13.11.2018
Tag der Prüfung: 10.12.2018

Darmstadt — D 17

Erklärung zur Dissertation

Hiermit versichere ich, die vorliegende Dissertation ohne Hilfe Dritter nur mit den angegebenen Quellen und Hilfsmitteln angefertigt zu haben. Alle Stellen, die aus Quellen entnommen wurden, sind als solche kenntlich gemacht. Diese Arbeit hat in gleicher oder ähnlicher Form noch keiner Prüfungsbehörde vorgelegen.

Darmstadt, den February 13, 2019

(K. König)

Bitte zitieren Sie dieses Dokument als:
URN: urn:nbn:de:tuda-tuprints-84014
URL: http://tuprints.ulb.tu-darmstadt.de/8401

Abstract

A beamline for high-precision collinear laser spectroscopy was designed, constructed and commissioned within this work. The main aspect was the development of a technique for a precise high-voltage determination with an accuracy in the sub-ppm regime. It is based on the laser-spectroscopic measurement of an ion velocity after acceleration with the high-voltage of interest by the determination of the Doppler shifted transition frequency. With an accurate knowledge of the rest-frame transition frequency f_0 and the mass m, the high-voltage of interest U can be traced back on natural constants like the speed of light c and the elementary charge $q = n \cdot e$ as well as on the measurement of a laser frequency f_L

$$U = \frac{mc^2}{2q} \frac{(f_0 - f_\mathrm{L})^2}{f_0 f_\mathrm{L}} \,. \tag{1}$$

Since the laser frequency can be accurately determined with a frequency comb, this technique fulfills the requirements for the definition of a quantum standard.

In first measurements with Ca^+ and In^+ ions, accuracies in the determination of high voltages between 1 kV and 20 kV of the order of 5 ppm were demonstrated. This corresponds to an increase in precision by a factor of 20 compared to earlier attempts and is mainly achieved by the improved experimental setup and the newly developed two-chamber approach with reference measurements. Further improvements of the laser stabilization scheme and of the laser-ion beam superposition that have been realized within this work, have the potential to enable laser-based high-voltage evaluations with uncertainties below 1 ppm. This would outperform the conventional technique based on high-voltage dividers and yield an unprecedented accuracy whereof several applications in metrology and science can benefit.

Zusammenfassung

Die kollineare Laserspektroskopie bietet neben vielfältigen wissenschaftlichen Anwendungen die Möglichkeit eine Spannungsmessung auf eine Frequenzmessung dopplerverschobener Spektrallinien zurückzuführen und eignet sich somit zur Definition des fehlenden Quantenstandards in der Hochspannungsmetrologie. Mit diesem Ziel wurde im Rahmen dieser Arbeit ein experimenteller Aufbau für hochpräzise, kollineare Laserspektroskopie entworfen, aufgebaut und in Betrieb genommen.
Die mit der zu messenden Hochspannung U beschleunigten Ionen erfahren bei der Wechselwirkung mit dem Spektroskopielaser eine geschwindigkeitsabhängige Dopplerverschiebung. Die resonante Laserfrequenz f_L kann dank der Frequenzkammtechnologie mit hoher Genauigkeit bestimmt werden, sodass die über Naturkonstanten verknüpfte, anliegende Spannung U akkurat ermittelt werden kann

$$U = \frac{mc^2}{2q} \frac{(f_0 - f_\mathrm{L})^2}{f_0 f_\mathrm{L}} \,. \tag{2}$$

Da sich die Masse m der Ionen und deren Übergangsfrequenz f_0 im Ruhesystem in Fallenexperimenten präzise bestimmen lässt und die Ladung $q = n \cdot e$ sowie die Lichtgeschwindigkeit c bekannt sind, eignet sich dieser Ansatz zur Definition eines Quantenstandards.
Erste laserspektroskopische Hochspannungsmessungen zwischen 1 kV und 20 kV mit Ca^+ und In^+ Ionen konnten mit resultierenden Unsicherheiten von etwa 5 ppm durchgeführt werden. Dies entspricht einer Genauigkeitssteigerung um einen Faktor 20 gegenüber bisherigen Versuchen. Insbesondere der verbesserte experimentelle Aufbau und ein neu entwickelter Ansatz, der auf einem Zwei-Kammer Prinzip mit Referenzmessungen basiert, trugen zu den Verbesserungen bei. Seit den ersten Messungen wurden weitere Entwicklungen in der Stabilisierung der Lasersysteme sowie in der Überlagerung von Laser- und Ionenstrahl verwirklicht, sodass in Zukunft Hochspannungsmessungen mit Unsicherheiten unter 1 ppm möglich sein sollten. Diese Genauigkeit würde das Limit der konventionellen, auf Spannungsteilern basierten Technik durchbrechen und so neue Möglichkeiten für präzise Anwendungen in Metrologie und Wissenschaft bieten.

Contents

List of Figures

List of Tables

1 Motivation

The accurate measurement and definition of (base) units always has been the interest of mankind since science, economy and the every day life benefit from improved means and methods of metrology - the science of measurement. Already at the end of the 18th century first attempts to define a unified system of measures were made by the French Academy of Sciences to overcome the challenges of several, local measure quantifications. To establish a universal and reproducible system, e.g., a fraction of the Earth's meridian was proposed to define the length whereof other units could be derived. The underlying concepts have been proposed even a century earlier demonstrating the high interest in a rational unit definition [1].

The early metric system was improved, clarified and expanded to the International System of Units (SI, Système International d'unités) which has been adopted nowadays by most countries. But still a lot of effort is taken to further enhance its accuracy. Especially by tracing back the measures to quantum effects, it became possible to establish a new level of reproducibility and precision. In particular, the time/frequency measurement reaches outstanding results with relative uncertainties of 10^{-16} thanks to atomic clocks [2, 3]. Nevertheless, different approaches are pursued to further improve the accuracy of frequency measurements [4, 5, 6] which enable new scientific experiments like the accurate test of the time dilation [7] or the time and space dependence of fundamental constants such as the fine structure constant α [8]. Beside science, several other applications like the Global Positioning System (GPS) are based on precise time measurements leading to benefits for the whole society.

The accuracy of frequency measurements was the base of a redefinition of the meter by defining the speed of light as $c = 299\,792\,458\,\mathrm{m/s}$ and quantifying the meter as the length that light travels in vacuum in $1/299\,792\,458\,\mathrm{s}$. However, there are measures which could not be traced back to quantum effects so far. For example the kg is still defined by the *International Prototype of the Kilogram*, a cylinder of platinum-iridium alloy. To refine this state, attempts like the Avogadro project [9] and the Kibble balance [10] are ongoing to define the missing measures on natural constants. It is expected that on May 20th 2019 the new SI will take effect, in which a network of natural constants will be declared to have fix numbers, which then define the size of the so-far-called base units.

The measurement of high voltages is still based on conventional methods limiting its uncertainty to the ppm (parts-per-million) level. On the contrary, small voltages can be traced back to a quantum effect with a relative uncertainty of 10^{-10} [11] since they can be generated by Josephson junctions consisting of two superconductors separated by a few nm thick isolator. To create potential differences of up to 10 V, several thousand junctions are connected in series and irradiated with a microwave of the frequency $f_\mathrm{J} \approx 70\,\mathrm{GHz}$ generating a small but discrete voltage difference between the superconducting layers

$$U_n = n\frac{h}{2e}f_\mathrm{J} = n \cdot 150\,\mu\mathrm{V} \tag{1.1}$$

where e and h are the electric charge and the Planck constant. The generated voltage U_n depends only on the amount of Josephson junctions n, the irradiated frequency f_J that can be precisely traced back to the frequency standard and fundamental constants, fulfilling the requirements of a quantum standard.

However, it is infeasible to extend this technique to higher voltages or even into the kV range due to its technical complexity. Instead high-voltage dividers realized as a chain of similar resistors are used to convert these potential differences with an accurately known divider ratio into the range of some V where it becomes possible to compare them with a Josephson voltage standard. However, these dividers have the inherent disadvantage of being susceptible to changes of ambient conditions and the inner structure of the building parts, which can cause slow changes of the divider ratio. An active stabilization of temperature, grouping of resistors with opposite characteristic thermal behavior, shielding of external fields and preaging of the resistors can partially compensate these effects. Nevertheless, the high-voltage dividers have to be regularly traced back to the low-voltage Josephson standard by a stepwise calibration of voltage references and reference dividers, to exclude remaining drifts in the range of ppm/year. This procedure requires many steps and has numerous sources of systematic errors [12] setting a natural uncertainty limit of 1 ppm [13].

In many cases, applications as well as metrology in general would gain from a technique for a direct and absolute high-voltage measurement. In the 1980th several ideas came up for its very realization. For example, it was proposed to use a cavity resonator as a speed filtering system for electrons accelerated with the voltage of interest [14]. Depending on irradiated microwave frequency only one velocity class is able to pass the resonator. However, due to technical problems the achieved accuracy was limited to 10^{-4} [15]. Another approach was introduced by Poulsen in 1982 [16]. He proposed to use the high voltage for accelerating ions with well-known mass and atomic transition frequency and to measure the relativistic Doppler shift of the transition frequency with collinear laser spectroscopy. Based on this principle, Poulsen and Riis accomplished to stabilize a high-voltage of interest to the 10^{-6} level but the absolute voltage determination was limited by lack of absolute laser frequency measurements [17, 18]. Following this approach and using modern wavemeters as well as a caesium transition as reference, Götte et al. were able to demonstrate high-voltage measurements in the 10^{-4} regime by measuring the potential difference between ion source and fluorescence detection chamber [19, 20]. In this case the accuracy was limited mainly by systematic uncertainties due to the undefined starting potential inside the ion source and by collisions of the ions with residual gas during transport. Further attempts to measure high voltages were performed at ISOLDE at CERN during collinear laser spectroscopy measurements on beams of on-line mass-separated isotopes. A frequency-comb referenced laser system was employed to measure the acceleration voltage of the ions with a relative accuracy of a few times 10^{-5} [21], though the setup was not designed for voltage measurements.

To further increase the accuracy, a setup with two consecutive interaction chambers for resonant collinear laser excitation was already proposed by Poulsen and Riis [18] and later again by Götte et al. [19] to eliminate systematic uncertainties caused in the ion production process. Following this approach, a prestudy experiment was realized in 2013 at the University of Mainz [22]. With the experience gained there, a new setup was designed at the TU Darmstadt in particular to perform laser-based high-voltage measurements in the range of 1 to 100 kV aiming for accuracies in the sub-ppm regime.

At the ALIVE (Accurate Laser Involved high Voltage Evaluation) project the experimental setup consists of two laser systems and an ion source connected to an ultra-high vacuum beamline equipped with detection and interaction regions which have been assembled within this work. Subsequently, a detailed commissioning has been executed since highly-accurate voltage measurements are only possible after a precise understanding of the systematic uncertainties. Hence, for the first stage of the project $^{40}Ca^+$ ions have been chosen since their characteristics are well understood from previous attempts [19, 22]. Although this ion species is not offering best conditions for a laser-based high-voltage evaluation, accuracies on the 5-ppm level could be demonstrated [23, 24]. After this first successful demonstration of a two-chamber pump-and-probe approach for laser-based high-voltage measurements, the experimental setup was improved further and the feasibility of narrow-linewidth transitions was investigated. In^+ offers an intercombination transition which reduces the linewidth by two orders of magnitude compared to Ca^+ which leads to a increased sensitivity for high-voltage measurements.

These developments allow to target the sub-ppm regime which is of interest for many applications. For example at the KATRIN experiment [25] in Karlsruhe a voltage of -18.6 kV is needed to be measured with a precision of at least one ppm. This experiment searches for a finite neutrino mass by measuring precisely the beta-spectrum of tritium near its endpoint at about 18.6 keV using a so called MAC-E-Filter (Magnetic Adiabatic Collimation combined with an Electrostatic Filter). The importance of precise high-voltage measurements in this range is underlined by recent efforts to improve the technique in connection with the KATRIN experiment: At WWU Münster a new approach was used to improve the calibration by tracing the linearity of the dividers with a measurement at $U_{\text{tot}} = U_1 + U_2$ where a variable and precisely known voltage U_2 is generated on top of a high-voltage U_1 [26]. Furthermore, the MAC-E-Filter was used to measure the precisely known conversion lines of ^{83m}Kr during the commissioning phase of the KATRIN experiment, serving as a natural standard for the high-voltage measurement. There, an uncertainty of 5 ppm was achieved which is in good agreement with previous calibrations [27]. The laser based approach presented here has the potential to increase the accuracy of high-voltage measurements even further. Besides KATRIN, other high-precision experiments, e.g., at storage rings [28] or at ISOL-facilities [29, 30] as well as metrology in general would benefit from more accurate high-voltage measurements.

2 Theoretical background

Different approaches have been suggested to measure high voltages via laser spectroscopy. These will be discussed in this chapter together with the basics of Doppler velocimetry. Possible systematic uncertainties will be introduced and quantified in a way that their influence on the accuracy of the high-voltage measurement can be estimated. Since this strongly depends on the ion species used, possible candidates are presented and compared in terms of their relevant properties.

2.1 Collinear laser spectroscopy

'Never measure anything but frequency!' - this advice from Arthur Schawlow [31] states precisely that in modern physics nothing can be measured more accurately than frequencies. Starting from several Hertz over the radio frequencies up to optical frequencies an outstanding precision is achieved since the establishment of atomic clocks [3] and frequency combs [32].

In laser spectroscopic experiments this is used to measure atomic and nuclear properties with high precision. This is often done in traps or by collinear laser spectroscopy. The latter technique is particularly useful to determine the properties of exotic nuclei with lifetimes of only a few milliseconds.

2.1.1 Relativistic Doppler shift

In classical collinear laser spectroscopy ions with mass m are extracted from an ion source and accelerated to typically $E_{\mathrm{kin}} = 10-60\,\mathrm{keV}$ kinetic energy to compress the initial, longitudinal velocity distribution Δv which is possible due to the quadratic energy-velocity relation. In the non-relativistic limit this can be directly identified:

$$E_{\mathrm{kin}} = \frac{1}{2}mv^2 \Rightarrow \Delta v = \frac{\Delta E_{\mathrm{kin}}}{mv} \,. \tag{2.1}$$

This Doppler compression is the key to extract precise transition frequencies with collinear laser spectroscopy since a large velocity spread would cause a significant broadening of the transition linewidth. The fast ion beam is collinearly superimposed with a laser beam. In an interaction chamber resonant laser excitation can take place if the laser frequency in the ion's rest frame matches its transition frequency f_0. This condition can be identified by observing the fluorescence light emitted by the ions being maximal in case of resonant excitation. Since the ion is moving with a velocity $\beta = v/c$, this frequency is shifted with respect to f_0 and the laser frequency f_{L} in the laboratory frame has to be set to

$$f_{\mathrm{L}} = f_0 \frac{1}{\gamma(1-\beta\cos\alpha)} \tag{2.2}$$

to obtain the resonance condition. Here, α is the angle between laser and ion beam and $\gamma = 1/\sqrt{1-\beta^2}$ the relativistic time dilation factor.

There are three special cases which can be used for laser spectroscopy: In the orthogonal case the angle between laser and ion beam is $\alpha = \pi/2$. Here the Doppler shift nearly vanishes

$$f_{\perp} = f_0 \frac{1}{\gamma} \tag{2.3}$$

but since it is experimentally difficult to realize an angle of exactly 90° between both beams, large systematic uncertainties come along with this approach. Moreover, the transverse velocity component is not compressed by the acceleration leading to large Doppler broadening and the short interaction time will cause transit-time broadening. Therefore, in collinear laser spectroscopy the beams are either copropagating (c) ($\alpha = 0$) or counterpropagating (a) ($\alpha = \pi$). This leads to

$$f_\mathrm{c} = f_0 \frac{1}{\gamma(1-\beta)} = f_0 \gamma (1+\beta) \quad \text{if} \quad \alpha = 0 \tag{2.4}$$

$$f_\mathrm{a} = f_0 \frac{1}{\gamma(1+\beta)} = f_0 \gamma (1-\beta) \quad \text{if} \quad \alpha = \pi \ . \tag{2.5}$$

Here, both beams are superimposed along a large distance and the angle α can be controlled much better. Furthermore, the transition frequency of an ion can be directly determined without knowledge of the ion velocity, if the ion beam is superimposed with a laser beam collinearly and anticollinearly (quasi) simultaneously. In this particular case, the product of both laser frequencies which can excite the ion yields

$$f_\mathrm{c} \cdot f_\mathrm{a} = f_0^2 \gamma^2 (1+\beta)(1-\beta) = f_0^2 \ . \tag{2.6}$$

This makes collinear laser spectroscopy a powerful tool to investigate ions or atoms very precisely even without accurate knowledge of the ion velocity which is usually determined through a measurement of the voltage applied to the ion source. Since such a voltage measurement usually contributes with a relatively large uncertainty, the accuracy of the determination of transition frequencies can be improved drastically [30, 33, 34, 35].

2.1.2 Doppler velocimetry

Applying Doppler velocimetry, it is the velocity of the ions and not the transition frequency that is investigated. This can then be related to the corresponding acceleration voltage U. For this purpose, ions with well-known mass m and transition frequency f_0 are chosen and either f_a or f_c is measured. Solving Eq. 2.4 and Eq. 2.5 for the velocity β yields

$$\beta = \frac{f_\mathrm{c}^2 - f_0^2}{f_\mathrm{c}^2 + f_0^2} \quad \text{if} \quad \alpha = 0 \tag{2.7}$$

$$\beta = \frac{f_0^2 - f_\mathrm{a}^2}{f_\mathrm{a}^2 + f_0^2} \quad \text{if} \quad \alpha = \pi \ . \tag{2.8}$$

The acceleration voltage U is linked to the velocity via the kinetic energy gained by the ions while passing through the electric acceleration field

$$E_\mathrm{kin} = mc^2 \left(\frac{1}{\sqrt{1-\beta^2}} - 1 \right) = qU \ . \tag{2.9}$$

In the case of singly-charged ions the charge is $q = e$. Solving the equation for U leads to

$$U = \frac{mc^2}{2q} \frac{(f_0 - f_\mathrm{c/a})^2}{f_0 f_\mathrm{c/a}} \ . \tag{2.10}$$

This shows that a voltage measurement can be transformed into a measurement of a laser frequency $f_\mathrm{c/a}$ by collinear laser spectroscopy connected via fundamental physical constants, which is a favorable condition for high-accuracy measurements.

Even without a precise knowledge of the transition frequency f_0, the applied high voltage can be accurately determined if the collinear/anticollinear approach is chosen, since the velocity β can be identified as

$$\beta = \frac{f_\mathrm{c} - f_\mathrm{a}}{f_\mathrm{c} + f_\mathrm{a}} = 1 - \frac{2}{f_\mathrm{c}/f_\mathrm{a} + 1} \,. \tag{2.11}$$

For this kind of measurements an additional laser system is needed which would increase the complexity of the experimental setup. On the other hand, the measurement of the absolute laser frequency is not critical anymore in this case as long as the frequency ratio between both lasers can be precisely identified as demonstrated in [20].

In the more general case where $\cos\alpha \neq 0$, the determined velocity strongly depends on the angle between ion beam and laser with the frequency f_L in the laboratory frame. Solving Eq. 2.2 for the velocity β yields

$$\beta = \frac{f_\mathrm{L}^2 \cos\alpha - \sqrt{f_\mathrm{L}^2 f_0^2 \cos^2\alpha + f_0^4 - f_\mathrm{L}^2 f_0^2}}{f_0^2 + f_\mathrm{L}^2 \cos^2\alpha} \tag{2.12}$$

$$\text{if } \; f_\mathrm{L} \geq f_0, \alpha \in \left[-\cos^{-1}\sqrt{\frac{f_0^2 f_\mathrm{L}^2 - f_0^4}{f_0^2 f_\mathrm{L}^2 - f_\mathrm{L}^4}}, \cos^{-1}\sqrt{\frac{f_0^2 f_\mathrm{L}^2 - f_0^4}{f_0^2 f_\mathrm{L}^2 - f_\mathrm{L}^4}} \right] \approx \left[\frac{-\pi}{2}, \frac{\pi}{2} \right] \text{ if } \; f_\mathrm{L} \approx f_0$$

$$\beta = \frac{f_\mathrm{L}^2 \cos\alpha + \sqrt{f_\mathrm{L}^2 f_0^2 \cos^2\alpha + f_0^4 - f_\mathrm{L}^2 f_0^2}}{f_0^2 + f_\mathrm{L}^2 \cos^2\alpha} \tag{2.13}$$

$$\text{if } \; f_\mathrm{L} < f_0, \alpha \in \left(\cos^{-1}\sqrt{\frac{f_0^2 f_\mathrm{L}^2 - f_0^4}{f_0^2 f_\mathrm{L}^2 - f_\mathrm{L}^4}}, 2\pi - \cos^{-1}\sqrt{\frac{f_0^2 f_\mathrm{L}^2 - f_0^4}{f_0^2 f_\mathrm{L}^2 - f_\mathrm{L}^4}} \right) \approx \left(\frac{\pi}{2}, \frac{3\pi}{2} \right) \text{ if } \; f_\mathrm{L} \approx f_0$$

which has two reasonable solutions. In the upper case, the ion moves towards the light source whereas it has a velocity component away from the light source in the lower case. These solutions are not symmetric due to the transverse Doppler effect which leads to a shift caused by the time dilation that can usually be neglected if $\beta \ll 1$.

With these equations, the uncertainty due to a remaining angle between both beams resulting from a misalignment will be estimated below.

2.1.3 Doppler tuning

Up to now, the laser frequency in the laboratory frame has been adjusted to match the resonance condition and excite the ions which had a fixed velocity. For a total acceleration potential U_tot the laser frequency $f_\mathrm{c/a}$ has to be set to

$$f_\mathrm{c/a} = f_0 \left[1 + \frac{qU_\mathrm{tot}}{mc^2} \left(1 \pm \sqrt{1 + 2\frac{mc^2}{qU_\mathrm{tot}}} \right) \right] \tag{2.14}$$

with a positive sign in case of collinear and a negative sign for anticollinear superposition. The resonance can be identified by varying the laser frequency and collecting the fluorescence photons. But performing accurate scans of the laser frequency is more complex than stabilizing the laser to a fixed frequency. Hence, collinear laser spectroscopy is regularly performed by keeping the laser frequency constant but changing the ion velocity (Doppler tuning). This can be realized by applying an additional voltage

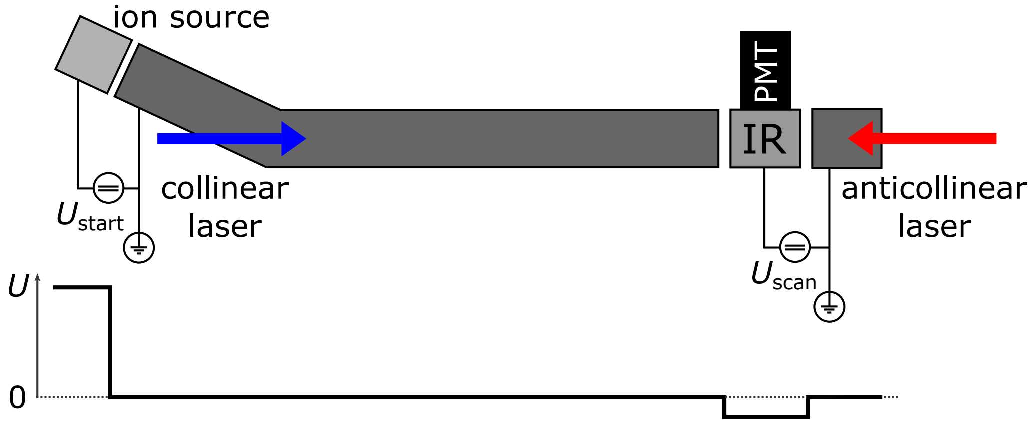

Figure 2.1: Simplified schematic of the measurement principle for a high-voltage evaluation in the one-chamber approach. The ions are accelerated between source and ground potential (beamline) with the high-voltage of interest U_{start} and are superimposed with a collinear or anticollinear laser beam. Ion optics along the beamline are not shown. The interaction region (IR) equipped with a fluorescence detection unit based on a photo multiplier tube (PMT) can be floated on a small, scannable potential U_{scan} to perform fast Doppler tuning for recording the resonance line and to avoid resonant interactions between ions and laser along the complete beamline.

U_{scan} to the interaction region, where the resonant laser excitation takes place. This additional scanning potential has to be added to the starting potential $U_{\text{tot}} = U_{\text{start}} + U_{\text{scan}}$ to obtain the total acceleration potential that is extracted by Eq. 2.10.

The required scanning potential to excite the ions for given laser and transition frequencies as well as a fixed starting potential can be calculated as

$$U_{\text{scan}} = U_{\text{tot}} - U_{\text{start}} = \frac{mc^2}{2q}\frac{(f_0 - f_{\text{c/a}})^2}{f_0 f_{\text{c/a}}} - U_{\text{start}}\,. \tag{2.15}$$

2.1.4 One-chamber approach

Since the acceleration voltage is directly linked by Eq. 2.9 to the velocity of the ions, Doppler velocimetry can be used to perform accurate high-voltage measurements. The most obvious way to accelerate the ions with the voltage of interest is by floating the ion source on a positive potential while the beamline is on ground potential. When leaving the source, the ions are accelerated and the gained kinetic energy can be precisely determined by Doppler velocimetry. To extract the resonance condition, either the laser frequency can be scanned or an additional voltage which is applied to the interaction region can be varied to perform Doppler tuning.

The principle of such a setup is illustrated in Fig. 2.1. The ion source and the beamline are separated by an insulator which allows to float the ion source on the high voltage U_{start} with respect to the beamline on ground potential. After acceleration, the ion beam is superimposed with the laser beam in either collinear or anticollinear geometry. Usually an electrostatic bender is used and combined with additional deflectors and quadrupoles (not shown) to achieve a good superposition of both beams. The interaction region is floated by a small and scannable voltage U_{scan} to perform Doppler tuning. Another advantage of applying this additional voltage is that resonant laser-ion interactions take place in the interaction region only since excitations along the complete beamline could lead to uncontrolled momentum transfer and optical pumping. A fluorescence detection unit is attached to the interaction region to detect the fluorescence light emitted by the ions, if the Doppler shifted laser frequency matches the transition frequency. The resonance condition can be identified by varying U_{scan}. Resolving Eq. 2.15 for the acceleration potential U_{start} yields

$$U_{\mathrm{start}} = \frac{mc^2}{2q}\frac{(f_0 - f_{\mathrm{L}})^2}{f_0 f_{\mathrm{L}}} - U_{\mathrm{scan}} \tag{2.16}$$

which is valid for both, a copropagating and a counterpropagating laser beam. Therefore, the laser frequency in the laboratory frame is called f_{L}.
Applying laser spectroscopy, only the total velocity and hence, the total acceleration potential U_{tot} can be measured. Since U_{scan} is small and can be determined with high accuracy, the high voltage U_{start} can be accurately identified if the fundamental physical constants mass m, transition frequency f_0 and electric charge q as well as the laser frequency f_{L} are well known and if all systematic effects are well under control. While the former requirements are fulfilled, thanks to accurate mass measurements in ion traps and the availability of frequency combs, systematic uncertainties limit the accuracy of this approach. Especially the conditions in the ion source and contact potentials lead to large uncertainties which will be discussed in section 2.2.10 and 2.2.11 in more detail. High-voltage measurements following this approach were realized in the 1980's by Poulsen and Riis [18] and in the 2000's by Götte et al. [19] but in both cases the voltage measurement was limited to relative uncertainties beyond 10^{-4} due to systematic contributions.

2.1.5 Two-chamber approach

To avoid these systematic uncertainties Poulsen [18] and later Götte [19] proposed a two-chamber approach. In this case two laser-ion interactions take place in two different parts of the beamline. The high-voltage of interest is applied between the first interaction region (IR1) and the second one (IR2). Furthermore, a second laser system is required if arbitrary voltages are to be measured. Otherwise, two different transitions of the ions have to be used in the two interaction regions which limits the measurable high voltages to a few certain values.
In this setup the ions still leave the source with a broadly distributed and not precisely known starting velocity and are accelerated by a first high voltage U_{start}. Nevertheless, the resulting ion velocity in IR1 can be accurately determined via Doppler velocimetry. This well-defined velocity can now be used as the starting velocity before the acceleration with the voltage of interest U_{HV}. After the second acceleration, the velocity can be measured again in IR2. Subtracting the voltages measured in IR1 and IR2 leads to

$$\begin{aligned} U_{1\to 2} &= U_{\mathrm{start}} + U_{\mathrm{HV}} + U_{\mathrm{scan2}} - (U_{\mathrm{start}} + U_{\mathrm{scan1}}) \\ &= U_{\mathrm{HV}} + U_{\mathrm{scan2}} - U_{\mathrm{scan1}} \end{aligned} \tag{2.17}$$

$$U_{\mathrm{HV}} = \frac{mc^2}{2q}\left(\frac{(f_0 - f_{\mathrm{L2}})^2}{f_0 f_{\mathrm{L2}}} - \frac{(f_0 - f_{\mathrm{L1}})^2}{f_0 f_{\mathrm{L1}}}\right) - U_{\mathrm{scan2}} + U_{\mathrm{scan1}}\ . \tag{2.18}$$

There are generally two possibilities to realize high-voltage measurements in the two-chamber approach: First, one can install a fluorescence detection unit at both interaction regions to measure the velocity distribution before and after acceleration. The drawback is that the line profile in both interaction regions will depend on the ion velocity distribution delivered by the ion source which can lead to asymmetric resonance signals. This can be avoided in the second case by performing optical pumping of a narrow velocity class in IR1 with a fixed frequency laser. Ions with a velocity that corresponds to the correct Doppler shift will be pumped into a specific atomic state that can be probed after the acceleration in IR2. Applying Doppler tuning, IR1 can stay on a fixed potential and only the voltage applied to IR2 has to be varied. This approach leads to a much better resolution because the first laser addresses

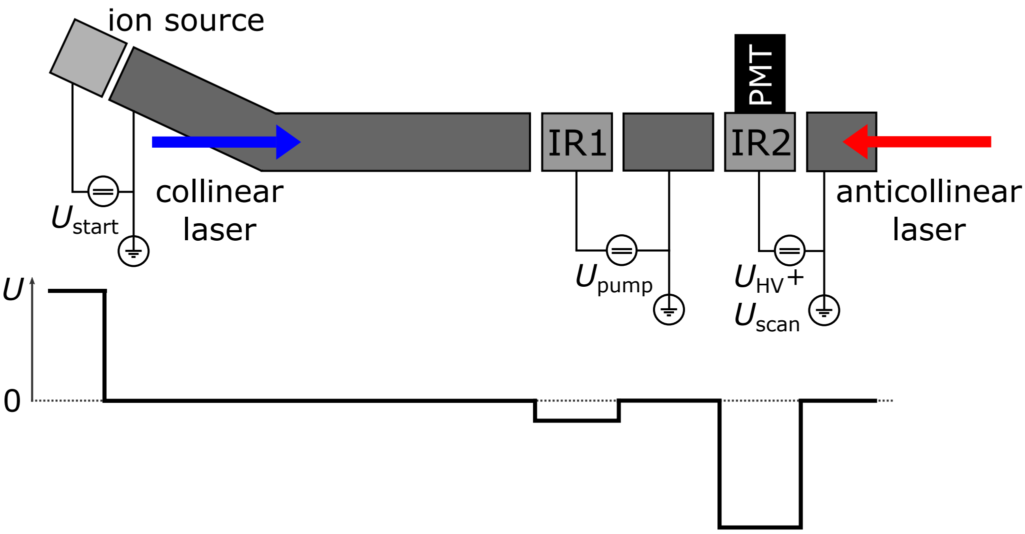

Figure 2.2: Simplified schematic of the measurement principle in the two-chamber approach. After the production and initial acceleration of the ions, they are superimposed with two lasers either in collinear or in anticollinear geometry (several configurations are possible). In the first interaction region (IR1) the population of one velocity class which can be chosen by the combination of laser frequency and the applied voltage U_{pump}, is optically pumped into a specific level or sub-state before the acceleration with the high-voltage of interest U_{HV} takes place. In the second interaction region (IR2) another laser is used to detect the population transfer. Applying an additional scan voltage U_{scan} at IR2, the Doppler shifted resonance frequency of the transferred population can be identified by a spectral feature (peak or dip) in the fluorescence signal recorded with a photo multiplier tube (PMT).

only a small velocity class determined by the convolution of the transition linewidth and the spectral width of the laser. However, this demands a suitable excitation scheme which limits the available ion species. Furthermore, several interactions are needed to pump one velocity class into this dedicated state and since every interaction causes a photon recoil, this will lead to systematic shifts in the ion velocity. Depending on the level scheme of the used ion species, it can be necessary to use two different atomic transitions with frequencies f_{0_1} and f_{0_2} for pumping and probing. In section 2.1.7 the possible schemes for optical pumping will be discussed in more detail. Keeping the potential U_{pump} of IR1 constant, the high voltage can be determined by

$$U_{\mathrm{HV}} = \frac{mc^2}{2q}\left(\frac{(f_{0_2}-f_{\mathrm{L2}})^2}{f_{0_2}f_{\mathrm{L2}}} - \frac{(f_{0_1}-f_{\mathrm{L1}})^2}{f_{0_1}f_{\mathrm{L1}}}\right) - U_{\mathrm{scan}} + U_{\mathrm{pump}} \,. \tag{2.19}$$

The geometry of the laser beams can be chosen arbitrarily collinear, anticollinear or mixed relative to the ion beam but the frequencies of laser L1 and laser L2 have to be chosen to be resonant with the ions in IR1 and IR2 respectively.

The advantage of a two-chamber setup is that all systematic uncertainties due to the ion source can be eliminated. But on the other hand, the experimental setup becomes more complex and more expensive since an additional laser setup is needed if arbitrary voltages are to be measured. Furthermore, there are still systematic uncertainties remaining. Will et al. performed a prestudy for high-voltage measurements with such a two-chamber approach in 2013 at the TRIGA-Laser experiment in Mainz [22] and could demonstrate an accuracy of some 100 ppm. Since this setup was not designed for pump-and-probe measurements and vacuum conditions as well as contact potentials caused large uncertainties this does not represent the limit of this method. Vacuum conditions can be easily improved and also the contact potentials can be minimized by manufacturing both interaction regions from the same material. The experience gained in [22] was considered when the design presented here was developed.

2.1.6 Reference-measurement approach

To exclude systematics due to interactions in different sections, it is favorable to perform all relevant measurements in one chamber while still following the pump-and-probe scheme. Proceeding with this idea, the applied high voltage U_{HV} can be measured more accurately, if two probe measurements are performed in IR2, one with and one without U_{HV} applied while the ions are still optically pumped in IR1. The measurement without U_{HV} will be called reference measurement. Subtracting the resulting voltages which both are measured in IR2 from each other yields

$$\begin{aligned} U_{\mathrm{tot}} - U_{\mathrm{tot}_{\mathrm{ref}}} &= U_{\mathrm{start}} + U_{\mathrm{HV}} + U_{\mathrm{scan}} - (U_{\mathrm{start}} + U_{\mathrm{scan}_{\mathrm{ref}}}) \\ &= U_{\mathrm{HV}} + U_{\mathrm{scan}} - U_{\mathrm{scan}_{\mathrm{ref}}} \,. \end{aligned} \tag{2.20}$$

For applying this approach two laser systems are necessary. The laser for the optical pumping needs to be stabilized on a fixed frequency f_{L1}, whereas the probe laser requires to be variable in frequency since the probing transition frequency f_0 has to be excited for two different ion velocities: At a laser frequency $f_{\mathrm{L2}_{\mathrm{ref}}}$ it excites the ions when $U_{\mathrm{HV}} = 0$, while at the frequency f_{L2} ions are excited when U_{HV} is applied. From these frequencies U_{HV} can be identified as

$$U_{\mathrm{HV}} = \frac{mc^2}{2q}\left(\frac{(f_0 - f_{\mathrm{L2}})^2}{f_0 f_{\mathrm{L2}}} - \frac{(f_0 - f_{\mathrm{L2}_{\mathrm{ref}}})^2}{f_0 f_{\mathrm{L2}_{\mathrm{ref}}}}\right) - U_{\mathrm{scan}} + U_{\mathrm{scan}_{\mathrm{ref}}} \,. \tag{2.21}$$

Since both interactions take place in the same chamber, systematic uncertainties which originate from the place of the interaction cancel. These are, for example, contact and thermal potentials but can also be caused from the laser-ion beam overlap. But to do so, regular changes between high-voltage measurements and reference measurements have to be realized. Therefore, the demands on laser L2 are higher in this approach since fast frequency changes are required while keeping a high stability and repeatability of the frequency set point.

2.1.7 Optical pumping

In the two-chamber and the reference-measurement approach, the information of the ion velocity before the acceleration can be stored through a preparation of a dedicated electronic state via optical pumping. After the acceleration with the voltage of interest this state is probed to determine the final velocity.

The two most basic concepts of optical pumping are performed in a Λ or a V-system as depicted in Fig. 2.3. In the Λ-system (e.g., Rb, Ca^+, $\mathrm{Ba}^+, \ldots$) the electron is excited from the pump level which can be the ground state, to the transfer level during optical pumping. This transfer level has (at least) two decay channels. Besides the decay into the initial pump level, a transfer into a metastable probe level is possible. Ions with a velocity fulfilling the resonance condition of transition frequency and Doppler-shifted laser frequency can be transferred into this state through several excitations with the laser for optical pumping. After the acceleration, the probe laser can drive the transition from the probe level to the transfer level. When decaying into the lower states, fluorescence light will be emitted which can be recorded with a photomultiplier.

In the V-system (e.g., Li^+, Be^+, $\mathrm{In}^+, \ldots$) usually the population in magnetic substates in the transfer level which can be the ground state, is manipulated. Using a pump level with a large amount of magnetic substates and circularly-polarized light, the highest or the lowest magnetic substates will become strongly populated in the transfer level in case of σ^+ or σ^- light, respectively. These are dark states when probing with light of the same polarization into a probe level with less magnetic substates (see Fig. 2.3b). Performing optical pumping of one velocity class with a fixed-frequency laser will lead to a dip in the observed fluorescence spectrum when scanning across the ion velocity distribution in the probing process.

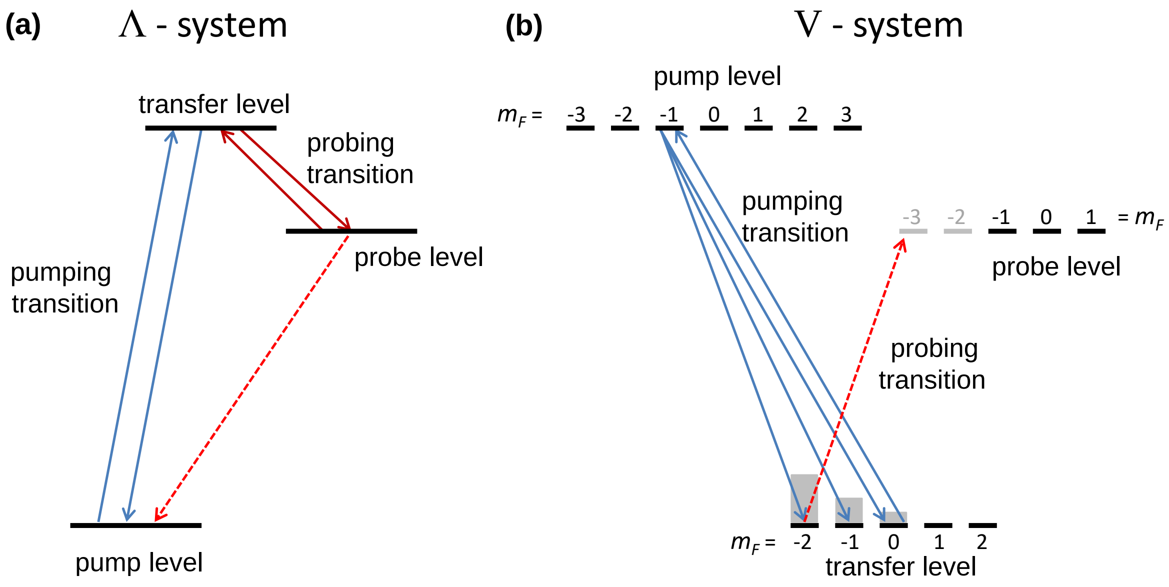

Figure 2.3: Optical pumping in a Λ (a) and a V-system (b). By populating the metastable probe level via a transfer level with a fixed-frequency pump laser, the information of the initial ion velocity can be stored in the Λ-System. After the acceleration the probing transition is driven to determine the final velocity. In the V-system the population of the magnetic substates m_F is manipulated. Here a possible excitation from the transfer level to the pump level with circularly-polarized σ^- light is depicted. Since the magnetic quantum number of the excited state is changed by $\Delta m_F = -1$ and decay channels with $\Delta m_F = -1, 0, +1$ are possible, the states with lower magnetic quantum numbers will be stronger populated after several excitations. Ions prepared like this are in a "dark" state for the probing transition if σ^- light is used again, since the probe level has less magnetic substates.

2.2 Influence of systematic uncertainties

As mentioned before, various systematic uncertainties occur in the different approaches to measure high voltages with collinear laser spectroscopy. These will have to be taken into account if accurate results are targeted. Based on Doppler velocimetry, only the total velocity and therefore the total acceleration potential can be determined with a single laser-ion interaction. The total acceleration potential can be a sum of different voltages to which also the impact of the systematics δU_{sys} has to be added

$$U = \frac{mc^2}{2q}\frac{(f_0 - f_{\text{L}})^2}{f_0 f_{\text{L}}} = U_1 + U_2 + \ldots + U_n + \delta U_{\text{sys}} \,. \tag{2.22}$$

This contribution of the systematics δU_{sys} was neglected so far. To estimate its impact on the accuracy of the high-voltage evaluation in the one-chamber, the two-chamber and the reference-measurement approach, all uncertainties considered so far in the experiments will be discussed in this section.

2.2.1 Fundamental constants

First of all, Eq. 2.22 has to be analyzed in terms of possible sources for uncertainties. The high voltage U is linked by some fundamental constants to the measured frequency f_{L}. These are the mass m of the ion, the speed of light c, the electric charge $q = n \cdot e$ and the rest-frame transition frequency f_0.
The speed of light is defined to $c = 299792458\,\text{m/s}$ and has no uncertainty. The mass and the charge are directly proportional and anti-proportional respectively. Hence, their relative uncertainty has to be

smaller than the demanded accuracy. Mass measurements can be performed very precisely for example in ion traps with uncertainties less than 10^{-10} [36] and since only singly-charged ions are used $q = e = 1.602\,176\,620\,8\,(98) \cdot 10^{-19}\,\mathrm{C}$ which has a relative standard uncertainty of $6 \cdot 10^{-9}$ [37]. Therefore, these demands are satisfied for a aspired accuracy of 1 ppm.

The dependency of the rest-frame transition frequency and of the laser frequency from the measured high voltage is more complicated and depending on both frequencies. In the non-relativistic limit the relation can be approximated by a simple relation depending on the rest-frame transition frequency only:

$$\frac{\partial U}{\partial f_0} = \frac{mc^2}{2 f_\mathrm{L} q} \frac{f_0^2 - f_\mathrm{L}^2}{f_0^2} \approx \frac{\sqrt{2qUmc^2}}{f_0 q} \approx \frac{\partial U}{\partial f_\mathrm{L}} \; . \tag{2.23}$$

Since the rest-frame transition frequency f_0 and the laser frequency f_L are in the same regime, this approximation holds for both frequencies. Quantifying the demands on a voltage measurement better than 1 ppm for $U = 14\,\mathrm{kV}$, $m = 40\,\mathrm{u}$ and $f_0 = 350\,\mathrm{THz}$ (850 nm) yields $\delta f < 150\,\mathrm{kHz}$ which corresponds to a required accuracy in the rest-frame transition frequency as well as in the laser frequency measurement of $2 \cdot 10^{-10}$. Rest-frame transition frequencies can be precisely measured in traps. Here, accuracies of 10^{-10} [38, 39, 40] can be achieved for dipole transitions[1], but not every ion species has been investigated with that precision so far. Therefore, the ion species has to be chosen in that respect, otherwise a term δU_{f_0} has to be considered in the high-voltage evaluation.

In the two-chamber measurement approach where optical pumping is performed, it can be beneficial to use different transitions. Both have to be precisely known, to avoid an additional uncertainty. Contrary, if the same transition is used twice, which is especially the case in the reference-measurement approach, the demands on the rest-frame transition frequency are reduced to

$$\frac{\partial U}{\partial f_0} = \frac{mc^2}{2q} \left(\frac{f_\mathrm{L2} - f_\mathrm{L1}}{f_\mathrm{L1} f_\mathrm{L2}} + \frac{f_\mathrm{L2} - f_\mathrm{L1}}{f_0^2} \right) \approx \frac{mc^2}{q} \frac{f_\mathrm{L2} - f_\mathrm{L1}}{f_0^2} \tag{2.24}$$

which is about a factor 3 less than in the one-chamber approach for typical conditions. This is not the case for the determination of the laser frequency since it differs in both interactions. Here, the requirements stated in Eq. 2.23 apply to both absolute frequency measurements.

In summary, the accurate determination of the resonance frequencies f_0 and f_L are the most critical contribution to the total measurement accuracy. Therefore, the following analysis on possible uncertainties will focus on potential influences in the determination of the frequencies f_0 and f_L.

2.2.2 Zeeman effect

The rest-frame transition frequency f_0 is a fundamental constant but caused by external magnetic fields, the degeneracy of the magnetic fine structure or hyperfine structure substates can be lifted. The Zeeman effect splits the line which leads to state dependent shifts of the transition frequency. Due to the earth magnetic field, magnets or ferromagnetic parts near the beamline, there is always a weak magnetic field B inside the interaction regions which can cause a broadening and/or a shift of the transition frequency, depending on the level scheme, the strength of the field and the polarization of the laser light.

In case of ions without nuclear spin $I = 0$, there will be a Zeeman splitting of the degenerated fine structure states. For each magnetic substate m_J of the total angular momentum $\vec{J} = \vec{S} + \vec{L}$ where $\vec{S}$ is the spin and $\vec{L}$ the orbital angular momentum, the energy of the state is shifted by [43]

$$\Delta E_\mathrm{Zeeman} = g_J m_J \mu_\mathrm{B} B \; . \tag{2.25}$$

---

[1] Much higher accuracies of up to 10^{-17} can be achieved for dipole-forbidden clock transitions [8, 41, 42]

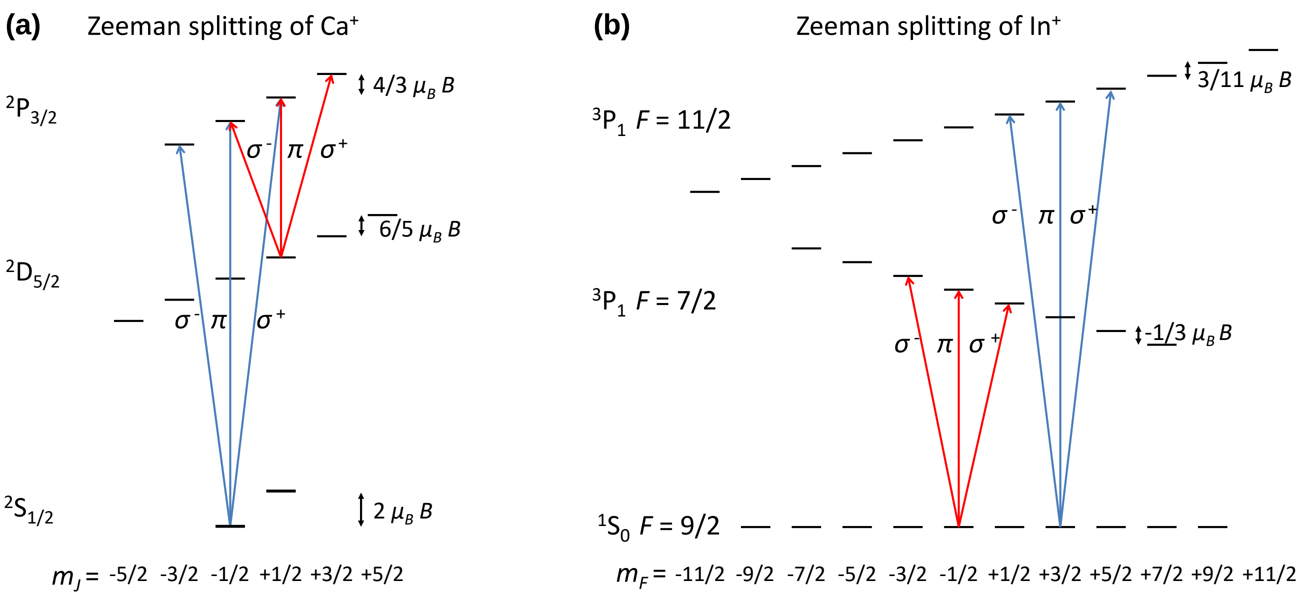

Figure 2.4: Zeeman splitting of fine structure and hyperfine structure levels with exemplary laser excitations for different laser polarizations. (a): Splitting of the $^2\mathrm{S}_{1/2}$, the $^2\mathrm{P}_{3/2}$ and the $^2\mathrm{D}_{5/2}$ level of Ca$^+$. (b): Splitting of the $^1\mathrm{S}_0$ $F = 9/2$, the $^3\mathrm{P}_1$ $F = 7/2$ and the $^3\mathrm{P}_1$ $F = 11/2$ levels of In$^+$. The splittings are not to scale. The small influence of the nuclear magnetic moment contribution in case of In$^+$ has been neglected.

Here, $\mu_\mathrm{B} = \frac{e\hbar}{2m_\mathrm{e}}$ is the Bohr magneton which corresponds to 14 MHz/mT and g_J the Landé factor

$$g_J = 1 + \frac{J(J+1) - L(L+1) + S(S+1)}{2J(J+1)} \,. \tag{2.26}$$

In Fig. 2.4a this is shown for the $^2\mathrm{S}_{1/2}$, the $^2\mathrm{P}_{3/2}$ and the $^2\mathrm{D}_{5/2}$ level of singly-charged calcium ions. For a magnetic field of $B = 48\,\mu\mathrm{T}$ which corresponds to the earth magnetic field in central Europe, this leads to a splitting of 1.3 MHz in the $^2\mathrm{S}_{1/2}$ state, 900 kHz in the $^2\mathrm{P}_{3/2}$ and 810 kHz in the $^2\mathrm{D}_{5/2}$ state between adjacent m states.

In case of ions with nuclear spin, I and J couple to the total angular momentum F which defines the hyperfine levels. A weak, external magnetic field will split the degenerated magnetic substates m_F by [44]

$$\Delta E = g_F m_F \mu_\mathrm{B} B \tag{2.27}$$

where

$$g_F = g_J \frac{F(F+1) + J(J+1) - I(I+1)}{2F(F+1)} - g_\mathrm{N} \frac{\mu_\mathrm{N}}{\mu_\mathrm{B}} \frac{F(F+1) + I(I+1) - J(J+1)}{2F(F+1)} \tag{2.28}$$

with the nuclear magneton $\mu_\mathrm{N} = \frac{e\hbar}{2m_\mathrm{p}}$ and the nuclear g-factor g_N.

This is illustrated in Fig. 2.4b for the case of the $^1\mathrm{S}_0$ $F = 9/2$, the $^3\mathrm{P}_1$ $F = 7/2$ and the $^3\mathrm{P}_1$ $F = 11/2$ levels of singly-charged indium ions. Here, the $^1\mathrm{S}_0$ state stays almost degenerated since for $J = 0$ only the nuclear moment contributes to the splitting, which is typically three orders of magnitude smaller than the electronic contribution and can be neglected at the present level of accuracy. However, the upper $^3\mathrm{P}_1$ levels split into 8 and 12 Zeeman states respectively with a difference of $\Delta f_{7/2} = -220$ kHz and $\Delta f_{11/2} = 180$ kHz between adjacent m-states for the earth magnetic field. Moreover, the direction of the energy shift depends on the specific hyperfine structure level which will increase systematic uncertainties if transitions to different F-levels are involved for pumping and probing purposes.

To resolve the Zeeman splitting, the natural linewidth of the transition and the spectral width of the laser have to be smaller than the Zeeman splitting which is usually not the case for the earth magnetic field. The Zeeman effect will nevertheless have an impact on the measurement. In the ground state, the population of the Zeeman levels is equally distributed because $\Delta E_{\text{Zeeman}} \ll k_{\text{B}}T$ for any ion source. Since the splitting is symmetric, there is no shift of the transition frequency if linearly-polarized light is used to excite the ions. But due to the different excitation energies, the transition is broadened and will also change its lineshape since it is now a superposition of several Lorentzians with different center frequencies. If the ions are irradiated with circularly-polarized light instead, only $\Delta m = +1$ transitions are allowed for σ^+ light and only $\Delta m = -1$ transitions for σ^- light. This will lead to a shift of the transition frequency. Therefore, the rest-frame transition frequency f_0 has to be corrected if circularly-polarized light is used. This correction will have a large uncertainty δU_{Zeeman} since the exact magnetic field inside the interaction region is not known. For elliptically polarized light, which is a mixture of circular and linear polarization, the shift is smaller but the ratio has to be precisely known to correct the transition frequency.

2.2.3 Stark effect

Analogously to the Zeeman splitting due to external magnetic fields, the Stark effect describes the consequences of external electric fields. But even though there are strong electric fields in the acceleration section, it is very unlikely that the D.C. Stark effect will have an impact on the measurement since there is no static electric field inside the interaction regions and the laser transition is between two low-lying states which are only weakly affected by the D.C. Stark effect at all. Also no contributions due to the A.C. Stark effect are expected. In each interaction region only one laser is in resonance with the ions. The other laser frequency is off by at least some GHz and since only very small laser powers are used, this will not affect the lineshape.

2.2.4 Determination of the laser frequency

The accurate measurement of the laser frequencies is as important as the well-known rest-frame transition frequency since its impact δU_{Laser} on the high-voltage measurement is identical. Therefore, an accurate absolute determination of the laser frequency with $\Delta f_{\text{L}}/f_{\text{L}} < 10^{-10}$ is required.
Wavemeters are flexible in frequency and can cover all possible laser frequencies but as they can achieve only accuracies of 10^{-9}, this technique is not sufficient to perform high-voltage measurements in the 1-ppm regime. More accurate is the stabilization of the laser system to well-known spectral lines for example in iodine cells. Although there is a huge amount of possible spectral lines, this technique is not as flexible as required for the measurement of arbitrary high voltages. An elegant solution is the optical frequency-comb technology, which is nowadays well established and able to measure optical frequencies with accuracies of up to 10^{-17} [8, 32] with a reasonable effort, provided that the spectral width of the laser is sufficiently small. Using this technique, δU_{Laser} can be reduced to the required level of accuracy.

2.2.5 Angular misalignment of ion and laser beam

Up to now, it was assumed that the angle α between laser and ion beam is either 0° for a collinear or 180° for an anticollinear setup. Since angles between both beams contribute with the cosine (see Eq. 2.2) any angle will lead to a smaller Doppler shift. Hence, an angular deviation α causes a frequency shift which can be estimated from Eq. 2.12 and 2.13. To achieve an uncertainty $\delta U_{\text{angle}} < 1\,\text{ppm}$ in the one-chamber approach, an alignment of $\alpha < 1\,\text{mrad}$ is required. Looking at a typical setup shown in Fig. 2.5 which consists of a pair of diaphragms with the diameter D in the distance L, the laser beam

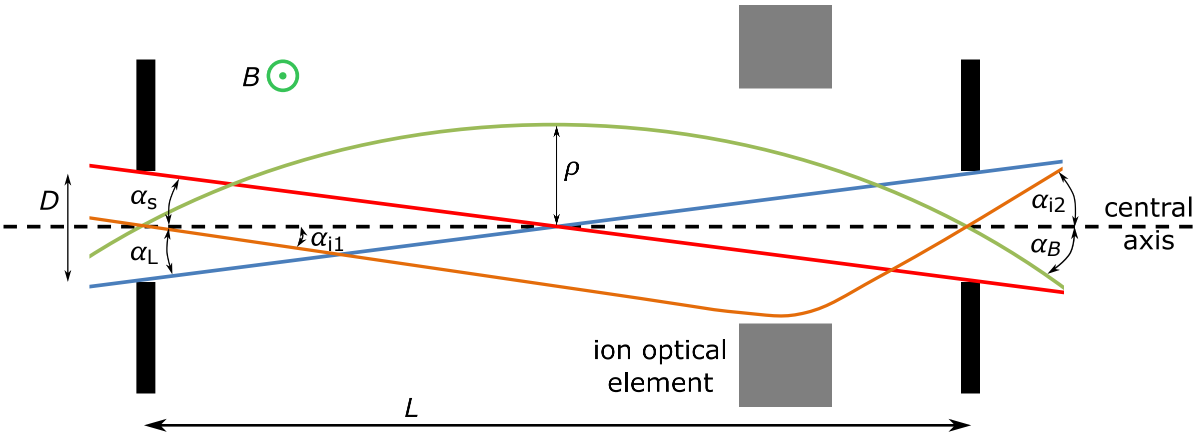

Figure 2.5: Possible angular deviations α of laser and ion beam between two apertures with diameter D in the distance L. If both beams travel straight through the apparatus (red and blue) the maximal angular deviation would arise from $\alpha = \alpha_\mathrm{s} + \alpha_\mathrm{L}$. But since the ion beam can be deflected by misaligned ion optical elements (orange) or by external magnetic fields B (green) even larger deviations are possible as indicated in exaggerated manner.

as well as the ion beam can deviate from the central axis by α_L and α_s. The largest possible angle α between both beams can be calculated as

$$\alpha = \alpha_\mathrm{s} + \alpha_\mathrm{L} = 2 \arctan \frac{D}{L} \approx 2 \frac{D}{L} \, . \tag{2.29}$$

For a given length of $L = 2.6\,\mathrm{m}$ an aperture of $D = 1.3\,\mathrm{mm}$ is necessary to satisfy $\alpha < 1\,\mathrm{mrad}$. This uncertainty can be reduced with a longer distance L between the diaphragms or smaller apertures D. However, the assumption that the beam travels like a straight line between the diaphragms is only a good approximation for the laser beam (neglecting diffraction) but not necessarily for the ion beam which can be deflected by electric and magnetic fields. Hence, ion optical elements between these diaphragms can lead to significant larger angles α_i. In particular, any misalignment of these elements can cause unforeseen ion beam trajectories as indicated in Fig. 2.5. With ion beam simulations its impact can be estimated. Any uncertainty in the alignment of the ion optics needs to be considered in these simulations as well, since misaligned ion optical elements can deflect the ion beam from the central axis.
Magnetic fields with a component vertical to the ion beam axis will cause a curved trajectory due to the Lorentz force. Hence, an angle of

$$\alpha_B = L \cdot B \cdot \sqrt{\frac{q}{8Um}} \tag{2.30}$$

will be acquired along the path between the two apertures. For the typical earth magnetic field in central Europe of $B = 48\,\mu\mathrm{T}$ and $^{40}\mathrm{Ca}^{+}$ ions at 14 keV, this yields $\alpha_B = 0.6\,\mathrm{mrad}$ which is close to the demand of $\alpha < 1\,\mathrm{mrad}$. This angle is largest at the diaphragms and would increase for a longer distance L in contrast to the case of α_s. Since the total systematic error due to the angular misalignment is the sum of the uncertainties arising from α_L, α_s, α_i and α_B, the optimal distance L has to be chosen by taking these effects as well as the diameter and the divergence of the beams into account. However, the impact of the earth magnetic field can be significantly reduced by placing the interaction region in the center between both diaphragms, where α_B would vanish. Here, the ion beam would be simply displaced by the distance ρ from the central axis

$$\rho = \frac{1}{B} \cdot \sqrt{\frac{2mU}{q}} \cdot (1 - \cos(\alpha_B)) \, . \tag{2.31}$$

For the above defined conditions this would lead to a misalignment of $\rho = 0.4\,\mathrm{mm}$.
In the pump-and-probe approaches a second laser is used. Both lasers can be superimposed with much smaller uncertainties since longer distances are available by placing additional apertures outside of the beamline. Therefore, the uncertainty of the relative angle between both laser beams is much smaller than the uncertainty of the angle between laser and ion beam. Since both laser frequencies are similar in particular in the reference-measurement approach, the frequency shift due to an angular deviation of the ion beam will be similar in the reference and high-voltage measurements, which partially compensates the resulting uncertainty as discussed in section 2.2.1. For perfectly aligned laser beams the resulting uncertainty can be reduced by about a factor of three compared to the resulting uncertainty in the one-chamber approach as derived in Eq. 2.24. In the two-chamber approach the uncertainty cannot be reduced, since two different interaction regions with potentially different angles between ion and laser beam are used. The former estimation is still valid and can be seen as the most pessimistic case which would occur if there is no angle in one interaction region and the maximal possible angle in the other interaction region.

2.2.6 Divergent beams

Real laser and ion beams are not pencil-like beams but have a finite divergence and, hence, an angular distribution. Due to the cosine dependency of the frequency shift (compare Eq. 2.2), an angular distribution will lead to an asymmetric broadening causing a frequency shift.
A realistic description for a laser beam is the Gaussian beam approach where the energy and the spacial distribution are limited compared to the more ideal plane-wave approach. Here, one has to differentiate between the near field in the region of the focal point which is close to a plane wave and the far field. As depicted in Fig. 2.6, the divergence is rather low in the near field while it converges to a maximal divergence angle [45]

$$\theta = \frac{c}{\pi w_0 f_\mathrm{L}} \tag{2.32}$$

in the far field with the beam waist w_0. Hence, θ can be seen as the most conservative estimation for the divergence of the laser beam. As an example, a laser with a frequency of 750 THz and a beam waist of $w_0 = 1\,\mathrm{mm}$ exhibits a half divergence angle of $\theta = 0.13\,\mathrm{mrad}$ which can be used to estimate an upper limit for the systematic uncertainty. Assuming the whole laser beam being tilted by this amount would cause a systematic deviation of only 0.02 ppm which is much smaller than the aspired accuracy and therefore negligible.
The divergence of the ion beam is usually much larger and has to be investigated experimentally, for example by measuring the beam diameter in the two diagnostic chambers using iris diaphragms. Again the tilted beam approach can be used to estimate an upper limit. But for a more realistic determination of δU_div, the angular distribution of the ion beam and the resulting asymmetric and shifted signal has to be considered in simulations. In the pump-and-probe approaches only ions with one specific velocity in laser beam direction can be optically pumped in IR1 independently from their transverse velocity component. Assuming an ideal acceleration in laser beam direction, only the longitudinal but not the transverse velocity component is affected. Hence, the total velocity change can be determined in IR2 yielding the accurate acceleration potential. Nevertheless, an ideal acceleration can only be realized, if the accelerating electric field is parallel to the ion beam direction and if the ion beam is equivalently collimated before and after the acceleration. Otherwise, some energy will be transferred into the transverse velocity component causing a systematic uncertainty. But since the first condition can be realized through a designated design of the electrodes and a proper alignment and the second condition by a careful adjustment of the ion optical components, the impact of the ion beam divergence can be reduced drastically.

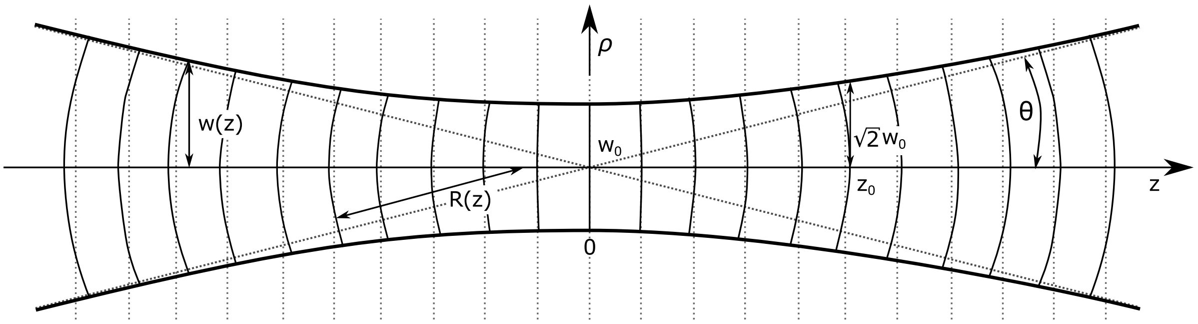

Figure 2.6: Characteristics of a Gaussian beam. At the beam waist with diameter w_0 the beam width $w(z)$ reaches its minimum and is increasing with the distance z. The beam divergence converges towards θ but is much smaller within the Rayleigh length z_0. For $z \ll z_0$ the wavefronts of the Gaussian beam with the radius of curvature R can be properly described as a plane wave (dotted lines) whereas at large distances $z \gg z_0$ they can be described as a spherical wave.

2.2.7 Phase front distortion

The Gaussian shape of the laser beam introduced in the previous chapter has another consequence on the laser-ion interaction. As depicted in Fig. 2.6, the wavefronts of a Gaussian beam deviate from the wavefronts of a plane wave and are position-dependent. This phase front distortion will cause a frequency shift experienced by moving ions.

The field strength of a Gaussian beam traveling in z-direction in a coordinate system with its center at $z = 0$, $\rho = 0$ is given by [45]

$$E(r,z) = \underbrace{A_0 \frac{w_0}{w(z)} e^{i(2\pi f_\mathrm{L} t - kz)}}_{\text{plane wave}} \underbrace{e^{-\rho^2/w^2(z)} e^{-ik\rho^2/2R(z)} e^{i\zeta(z)}}_{\text{Gaussian beam}} \tag{2.33}$$

with the Rayleigh length $z_0 = \pi w_0^2/\lambda$, the beam waist w_0, the beam radius $w(z) = w_0\sqrt{1+z/z_0}$, the radius of curvature $R = z(1 + (z_0/z)^2)$, the distance to the central axis ρ and the Gouy phase $\zeta(z) = \arctan(z/z_0)$. The Rayleigh length defines the distance where the beam size is a factor $\sqrt{2}$ larger than the beam waist. Here, the wavefront curvature reaches its maximum. Distances $z \ll z_0$ are called the near field where the wavefront shows only small deviations from a plane wave whereas at large distances $z \gg z_0$ the surfaces of constant phase are spheres centered on the waist. Furthermore, a Gaussian beam gains an additional phase shift ζ of π when passing through its focus. The half of this so-called Gouy phase shift is accumulated in the Rayleigh zone.

The total phase φ of the Gaussian beam can be extracted from Eq. 2.33 as

$$\varphi = 2\pi f_\mathrm{L} t - kz - \frac{k\rho^2 z}{2(z_0^2+z^2)} + \arctan\frac{z}{z_0}\ . \tag{2.34}$$

The frequency experienced by the moving ion corresponds to the temporal change of this phase and can be calculated as

$$f_\mathrm{ion} = \frac{1}{2\pi}\frac{\mathrm{d}\varphi}{\mathrm{d}t'} = \frac{1}{2\pi}\left(\frac{\partial\varphi}{\partial t} + \frac{\partial\varphi}{\partial z}\frac{\partial z}{\partial t} + \frac{\partial\varphi}{\partial\rho}\frac{\partial\rho}{\partial t}\right)\frac{\partial t}{\partial t'}\ . \tag{2.35}$$

With the transformation from the laboratory frame into the ion's rest frame $\partial t/\partial t' = \gamma$ and the radial as well as the axial velocity component of the ions $\partial\rho/\partial t = \beta c\sin(\alpha)$ and $\partial z/\partial t = \beta c\cos(\alpha)$ where α is the angle between ion and laser beam, this leads to a frequency in the ion's rest frame of

$$f_\mathrm{ion} = f_\mathrm{L}\gamma\left[1 + \beta\left(\cos\alpha\left(-1 + \frac{w_0^2}{2}\frac{1}{z_0^2+z^2} - \frac{\rho^2}{2}\frac{z_0^2-z^2}{(z_0^2+z^2)^2}\right) - \sin\alpha\frac{\rho z}{z_0^2+z^2}\right)\right] \tag{2.36}$$

which is valid for the collinear and the anticollinear case.
For a laser beam with a frequency of 750 THz and a beam waist of $w_0 = 1$ mm the deviation to the plane wave approach is less than 30 kHz in case of a mass 40 ion beam with 30 keV displaced by $\rho = 0.4$ mm and with a relative angle of $\alpha = 0.6$ mrad. The latter conditions correspond to the curved trajectory induced by the Lorentz force as discussed in section 2.2.6. The larger the ion velocity, displacement and angle between both beams, the larger the deviation and the impact δU_{Gauss} on the high-voltage evaluation. Furthermore, a smaller beam waist will lead to a drastic increase of the discrepancy between plane wave and Gaussian beam approach which is maximal in the Rayleigh zone. Otherwise, large distances to the focal point will decrease the deviations which become negligible for a collimated laser beam.
For converging beams ($z < 0$) and diverging beams ($z > 0$) the sign of the deviation changes. Hence, in the two-chamber approach where two different lasers are used, the resulting uncertainty increases. In the reference measurement the impact of the phase front distortion is reduced, if the probing laser is used for both measurements. Contrary, the knowledge of the exact frequency of the pumping laser is not required at all. It only needs to be constant between the reference measurements.

2.2.8 Photon recoil

Photons carry energy $E_\gamma = hf$ and momentum $p_\gamma = hf/c$. Both are transferred to the ion in the absorption process obeying the conservation laws. In the ion's rest frame ($v_0 = 0$ before the absorption) this leads to a momentum transfer of

$$\frac{hf'_{\text{L}}}{c} = m \cdot v \tag{2.37}$$

where m is the mass of the ion, v the ion velocity after the absorption and f'_{L} the laser frequency in the ion's rest frame. This obviously has two consequences on the high-voltage measurement: First, the velocity of the ion is altered which can lead to a systematic shift especially in a pump-and-probe approach. Second, a part of the photon's energy is not available for the electronic excitation, since it has been used to modify the ion's kinetic energy:

$$E_\gamma = hf'_{\text{L}} = \frac{m}{2}v^2 + \Delta E = \frac{m}{2}v^2 + hf_0 \,. \tag{2.38}$$

Only the amount ΔE can be used to drive the electronic excitation with the rest-frame transition frequency f_0. Therefore, the photon energy must be larger than the transition energy $E_\gamma > \Delta E$. Inserting Eq. 2.37 in Eq. 2.38 and solving the quadratic equation yields one physical solution for the difference between photon and real transition frequency

$$\Delta f = f'_{\text{L}} - f_0 = \frac{mc^2}{h}\left(1 - \sqrt{1 - 2\frac{hf_0}{mc^2}}\right) - f_0 \approx \frac{hf_0^2}{2mc^2} \tag{2.39}$$

which can be simplified if $f'_{\text{L}} \approx f_0$.
As an example, for an ion with $m = 40$ u and a rest-frame transition frequency of $f_0 = 350$ THz (850 nm) this would lead to a shift of $\Delta f = 7$ kHz whereas for a rest-frame transition frequency of $f_0 = 750$ THz (400 nm) this would cause a shift of $\Delta f = 30$ kHz which has to be considered in the evaluation of the high-voltage measurement from the resonance frequency to avoid a systematic uncertainty δU_{recoil}.
The second consequence mentioned above is the velocity change of the ion. Assuming only one interaction in the optical-detection region, there is no impact on the high-voltage measurement in the one-chamber approach. But depending on the properties of the ion, it can interact repeatedly with the laser and hence, a velocity change cannot be neglected anymore. In the pump-and-probe approaches usually only one interaction can take place in the optical-detection region for the ions addressed in this

thesis. The reason is that the ions will dominantly decay into a different level (Ca^+) as discussed in section 2.1.7 or that the transition rate is limited due to the long lifetime of the excited state (In^+).

This is different in the optical pumping process where the ions can interact several times with the laser. This causes a velocity change and leads to a systematic shift δU_{mult} in the two-chamber approach. Fortunately, this can be neglected in the reference-measurement approach since there all effects caused during the optical pumping cancel.

The change of the ion momentum caused by the emission of fluorescence photons will not lead to systematic shifts since its direction is not predetermined by the direction of the laser beam. Therefore, for a large ensemble of ions, the emission leads to a symmetric broadening of the velocity distribution whereas the absorption causes a systematic shift to smaller velocities in an anticollinear and to higher velocities in a collinear setup.

2.2.9 Collisions with residual gas

Collisions with residual gas atoms decelerate the ion beam and cause a systematic shift to smaller ion velocities as well as an asymmetric broadening of the velocity distribution. The mean path length $\bar{l}$ for identical particles which is an acceptable approximation, for a residual gas pressure p is [46]

$$\bar{l} = \frac{1}{p} \frac{k_{\mathrm{B}} T}{\sqrt{2} \pi d_{\mathrm{m}}^2} = \frac{1}{p} \cdot C_{\mathrm{gas}} \,. \tag{2.40}$$

Here, k_{B} is the Boltzmann constant, T the temperature and d_{m} the molecular diameter of the residual gas. For a specific gas, the second fraction can be combined into a temperature depending constant C_{gas}. In Tab. 2.1 this constant is listed for the most common gases at 273 K. Furthermore, the resulting mean free path length $\bar{l}$ is given for a residual gas pressure of $1 \cdot 10^{-8}$ mbar which is a typical value for the apparatus described in this thesis.

For any kind of gas, the ions can travel several kilometers in such an ultra-high vacuum before hitting a residual gas molecule. A beamline for collinear laser spectroscopy has a typical length of several meters. However, close to the thermal ion source the vacuum is often worse and several collisions can take place. In the one-chamber approach this is critical since it appears during the acceleration process that is used to measure the high-voltage of interest and will lead to considerable uncertainties δU_{gas}. This is completely eliminated in the pump-and-probe approaches where the complete measurement is transferred into the main ultra-high vacuum section of the beamline.

Table 2.1: Mean free path length $\bar{l}$ for different residual gases at 273 K in a $p = 10^{-8}$ mbar vacuum as well as the corresponding gas and temperature dependent constant C_{gas} (compare Eq. 2.40) [47].

gas	chemical symbol	C_{gas}/ m mbar	$\bar{l}(p = 10^{-8}\,\mathrm{mbar})$/km
Hydrogen	H_2	$11.5 \cdot 10^{-5}$	11.5
Nitrogen	N_2	$5.9 \cdot 10^{-5}$	5.9
Oxygen	O_2	$6.5 \cdot 10^{-5}$	6.5
Helium	He	$17.5 \cdot 10^{-5}$	17.5
Argon	Ar	$6.4 \cdot 10^{-5}$	6.4
Air	$N_2+O_2+\ldots$	$6.7 \cdot 10^{-5}$	6.7
water vapor	H_2O	$6.8 \cdot 10^{-5}$	6.8

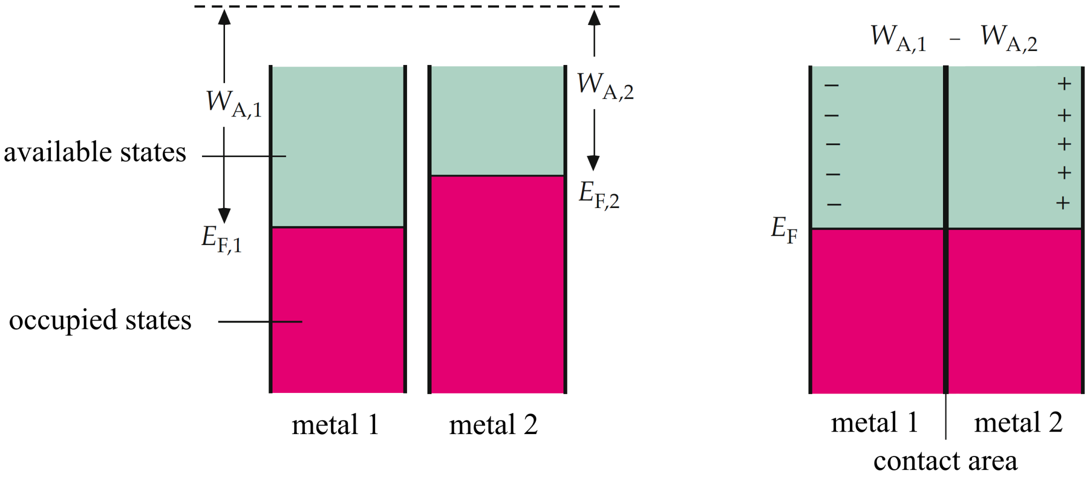

Figure 2.7: Metals with different Fermi energies E_F. The corresponding work function W_A is the difference between the Fermi energy and the energy of a free electron outside the metal. If both metals are in contact, electrons are transferred from the metal with the larger Fermi energy to the metal with the lower Fermi energy until an equilibrium is reached generating a contact voltage between both metals [48].

2.2.10 Thermal and contact potentials

While uncertainties in the determination of the ion velocities and velocity changing momenta transfer processes were discussed so far, we will now discuss effects that lead to differences between the acceleration potential experienced by the ions and the applied voltage. The most obvious of such a systematic shift of the acceleration potential is a contact potential which builds up between two materials with different work functions $W_{A,1}$ and $W_{A,2}$. When these are in contact, electrons from the metal with the larger Fermi energy are transferred to the metal with the lower Fermi energy until an equilibrium is reached (see Fig. 2.7) generating a contact voltage

$$U_{\text{contact}} = \frac{W_{A,1} - W_{A,2}}{e} \,. \tag{2.41}$$

Typical work functions of different metals are between 2 V and 6 V [48]. Hence, a significant contact voltage can affect the laser-based measurement of a high voltage, which is applied either between the ion source and the interaction region or between the two interaction regions. By using the same materials and the same manufacturing process, the contact potential can be minimized. But even small differences in the crystal structure of the materials and an accumulation of material layers on the surface originating from vapors and the ion beam inside the beamline will cause uncontrollable shifts. These potentials can be measured laser spectroscopically as mentioned in the introduction of the reference-measurement approach (section 2.1.6) and in more detail in section 4.3.1.

However, the contact potential can change over time, especially if the external conditions change. An extreme case is the one-chamber approach due to the conditions inside the source, where pressure changes, plasma effects and temperature changes lead to large uncertainties in the determination of the work function. The latter effect will additionally cause a thermoelectric voltage. Since the conditions may change quite quickly in the ion source, it is challenging to determine the contribution of the contact voltage to the acceleration potential leaving a large uncertainty $\delta U_{\text{contact}}$.

In the interaction regions IR1 and IR2, the conditions are less extreme and change only on longer time scales. The contact voltage will be nearly constant and its drifts can be determined more easily, leading to a much smaller uncertainty $\delta U_{\text{contact}}$ in the two-chamber approach. In the reference-measurement approach, the contact potential is actually measured with every reference measurement and changes will be directly recognized and canceled.

2.2.11 Starting potential in the ion source

Besides the varying contact potentials and the pressure conditions mentioned above, another disadvantage of the ion source as the starting point for the high-voltage measurement is the missing knowledge of the exact creation point of the ion inside the source. Depending on the type of ion source, heating currents, a plasma of electrons and generated ions or fringe fields of the acceleration field may lead to position-dependent voltages. The resulting energy distribution is often very broad and it is impossible to determine the absolute starting potential with an accuracy of a few 10 mV as it is required for a high-precision high-voltage evaluation. Typical uncertainties δU_{source} are of the order of several V which is the main disadvantage of the one-chamber approach. For the two-chamber-approach this uncertainty is irrelevant as discussed above.

2.2.12 Electric field penetration

An acceleration with the full voltage of interest is required if Doppler velocimetry is used for the voltage determination. This is only possible if the ions experience the complete potential drop. In particular, this means that in the interaction regions the undisturbed full potential has to be existent. This can be realized by a completely closed cage but since the ions need to enter and to leave the region, this is not feasible. If an optical signal is to be detected, also the photons have to leave the interaction region. Hence, several openings are necessary which must not be to small for efficient pumping to obtain ultra-high vacuum conditions. These openings are possible sources for field penetrations which can lead to potential changes that the ions experience. Therefore, the interaction regions have to be designed carefully. The remaining field penetration which causes the uncertainty $\delta U_{\text{penetration}}$ can be estimated properly from electrostatic field simulations.

2.2.13 Screening and space charges

Not only field penetrations can lead to a modified acceleration potential since electrostatic fields can be screened and/or superimposed by other electrostatic fields. But due to the homogeneous potential inside the interaction regions there are no electric fields inside which could be screened from residual gas particles or other ions and hence, screening will not cause uncertainties in the high-voltage evaluation. However, the ion beam itself generates an electric field which superimposes the applied acceleration potential and therefore will affect the total potential inside the interaction regions. Assuming a homogeneously, cylindrically distributed ion beam with a beam radius R_{ion} and an ion current I inside a cylindrical tube with the radius R_{tube}, the ion-beam induced space charge Φ_{ion} can be calculated as

$$\Phi_{\text{ion}} = \frac{1}{2\pi\epsilon_0}\frac{I}{v}\ln\frac{R_{\text{tube}}}{R_{\text{ion}}}\,. \tag{2.42}$$

The space charge depends on the velocity v of the ion beam and will change for different post-accelerations. Therefore, in a two-chamber approach the space charge will also contribute to the systematic uncertainties even though it is mainly compensated since the effect occurs in both interaction regions. The remaining velocity-dependent contribution δU_{charge} is of the order of some 100 µV for typical conditions in our experiment and can be disregarded at the current level of accuracy.

2.2.14 Voltage stability

A laser spectroscopic high-voltage determination takes several minutes. Therefore, it is important that the high-voltage of interest is stable over this period since fluctuations would limit the precision of the measurement. This defines the demands on the high-voltage stability to be of the same order as the aspired accuracy, otherwise δU_{HV} will contribute to the uncertainty of the high-voltage evaluation.

But not only the high-voltage of interest has to be stable. In the two-chamber and in the reference-measurement approach the voltage U_{pump} which is applied to the first interaction region, has to fulfill $\Delta U_{\mathrm{pump}}/U_{\mathrm{HV}} < 1\,\mathrm{ppm}$. Furthermore, the scan voltage U_{scan} which is applied to the second interaction region requires a stability and a linearity of $\Delta U_{\mathrm{scan}}/U_{\mathrm{HV}} < 1\,\mathrm{ppm}$. But since U_{pump} and U_{scan} are typically of about 100 V and the high-voltage of interest U_{HV} exceeds several kV, these demands are not as challenging and, hence, can be considered within δU_{HV}.

2.2.15 Fit of the experimental lineshape

After a measurement, the frequency of the laser that drives the transition of the accelerated ions has to be determined by fitting a preselected function to the transition lineshape observed with the photomultipliers. Here, insufficient statistics or an incorrect fit function can result in an inaccurate determination of the central laser frequency which can easily be of the order of 1 % of the natural linewidth. Then, this would contribute with δU_{fit} to the total uncertainty of the high-voltage evaluation.

Insufficient statistics can be avoided with a sufficiently long measurement time whereas systematic deviations emerging from the lineshape cannot be removed easily. Here, a detailed analysis is necessary to define a fit function that takes all effects into account which have an influence on the resulting lineshape. Since the lineshape strongly depends on the selected ion species and the corresponding pump-and-probe mechanism, this will be discussed in detail in section 2.4.

2.2.16 Total systematic uncertainty

Taking all effects into account, the resulting systematic uncertainty of a laser-based high-voltage evaluation with the different approaches can be quantified. In Tab. 2.2 the achievable limit of the different contributions in the well-adjusted and optimized experimental setup of ALIVE is listed for a negative (accelerating) high voltage. The (+) and (−) signs of the uncertainty correspond to the direction of the correction which compensates the systematic shifts. Furthermore, the estimated impact of the individual contributions for typical experimental conditions is given in parentheses to estimate its importance for the high-voltage measurement.

The impact of the listed systematics is largely independent from the ion species while other uncertainties that will mostly be determined by the property of the chosen ion species are not included. To these belong uncertainties arising from the ion mass, the knowledge of the rest-frame transition frequency or δU_{fit} which strongly depends on the linewidth of the transition. Furthermore, uncertainties due to the voltage stability δU_{HV} as well as the accurate frequency determination $\delta U_{\mathrm{Laser}}$ are not quantified since these infrastructural contributions have to fulfill the requirements to allow accurate high-voltage measurements.

Comparing the different approaches, the disadvantages of the one-chamber approach are obvious. But even the accuracy of the two-chamber approach can be considerably boosted by combining it with reference measurements. Hence, this will be applied in the ALIVE experiment and the further discussion will focus on this method to determine high voltages.

Table 2.2: Systematic uncertainties of collinear laser-based voltage measurements in the one-chamber, the two-chamber and the reference-measurement approach which have been discussed in detail in the sections referred to in the last column. The (+) and (−) signs correspond to the direction of the uncertainty which compensates the systematic shifts in case of a negative, accelerating high voltage. The first value for the well-adjusted experimental setup of ALIVE defines the achievable limit whereas the value in parentheses indicates the impact of the uncertainty contribution for typical conditions of a collinear laser spectroscopy setup as discussed in the text.

	one chamber / ppm	two chamber / ppm	reference measurement /ppm	discussion
δU_{Zeeman}	± 0 (3)	± 0 (6)	± 0 (1)	2.2.2
δU_{angle}	− 0.25 (25)	− <0.25 (<25)	− <0.1 (<10)	2.2.5
δU_{div}	− 0.2 (10)	± 0 (10)	± 0 (10)	2.2.6
δU_{Gauss}	± 0 (0.1)	± 0 (0.2)	± 0 (0.05)	2.2.7
δU_{recoil}	− 0 (0.1)	− 0 (<0.1)	− 0 (<0.05)	2.2.8
δU_{mult}	− 0.5	− 2	0	2.2.8
δU_{gas}	− 50	0	0	2.2.9
$\delta U_{\text{contact}}$	± 100	± 5	0	2.2.10
δU_{source}	± 100	0	0	2.2.11
$\delta U_{\text{penetration}}$	− 50	− 0.1	− 0.1	2.2.12
δU_{charge}	+ 50	+ 0.05	+ 0.05	2.2.13
δU_{total}	300	7	0.2	

2.3 Selection of the ion species

Many of the above discussed uncertainties are directly or indirectly linked to the properties of the ion species and manifest themselves in a frequency shift. Hence, by choosing an ion species where a large frequency shift will only cause a small voltage shift, the impact of the systematic uncertainties can be reduced. As introduced in Eq. 2.23, the differential voltage sensitivity $\kappa = \partial U / \partial f$ is a measure for this and can be seen as a first criteria for the sensitivity of laser-based high-voltage measurements. This differential voltage sensitivity in the non-relativistic approximation is given by

$$\kappa = \frac{\partial U}{\partial f} \approx \frac{\sqrt{2qUmc^2}}{f_0 q} \,. \tag{2.43}$$

To obtain small values for κ, an ion species with a large rest-frame transition frequency f_0 and a low mass m is favored.

Another important property is the natural linewidth Γ_0. Narrow-linewidth transitions are favorable since the resonance center can be determined precisely and small Doppler shifts can still be observed. But on the other hand, the scattering rate of the transition must still be sufficiently large for resonance fluorescence detection. Since external broadening effects (see section 2.4) will be of the order of several 100 kHz, an ultra-narrow linewidth would not lead to further improvements and a natural linewidth of about 1 MHz is desired.

The sensitivity for a high-voltage evaluation can be specified by the product $\kappa \cdot \Gamma_0$ of differential voltage sensitivity and transition linewidth. It describes the voltage shift that will lead to a shift of the resonance signal by one natural linewidth. Besides the sensitivity, even more criteria have to be considered for practical reasons: Ion production and the accessibility of the required laser light most importantly. Screening possible candidates and selecting only those which meet the latter requirements yields the list shown in Tab. 2.3. Here, the probing transitions are specified for $U_{\text{start}} = 15$ kV and $U_{\text{HV}} = -20$ kV which

Table 2.3: Suitable ion species for high-voltage measurements. Listed are wavelength and natural linewidth Γ_0 of the probing transition λ [49]. κ is the differential voltage sensitivity. The sensitivity $\kappa \cdot \Gamma_0$ represents the voltage shift which can be resolved by a shift of the resonance signal of one natural linewidth. Δf_{recoil} is the recoil shift due to the emission of a single photon. All values are calculated for $E_{\text{kin}} = 35$ keV. A * indicates that the transition does not start from the ionic ground state.

	Probing transition	λ / nm	κ/ mV/MHz	Γ_0 / MHz	$\kappa \cdot \Gamma_0$ /mV	Δf_{recoil} / kHz
$^7\text{Li}^{+*}$	$1s2s\,^3\text{S}_1 \rightarrow 1s2p\,^3\text{P}_{0,1,2}$	548.5	39.1	3.6	140.8	95
$^9\text{Be}^+$	$2s\,^2\text{S}_{1/2} \rightarrow 2p\,^2\text{P}_{1/2,3/2}$	313.2	25.3	18.0	455.4	226
$^{24}\text{Mg}^+$	$3s\,^2\text{S}_{1/2} \rightarrow 3p\,^2\text{P}_{1/2}$	280.4	37.0	40.9	1513	106
$^{27}\text{Al}^+$	$3s^2\,^1\text{S}_0 \rightarrow 3s3p\,^1\text{P}_1$	167.1	23.4	224.4	5251	265
$^{40}\text{Ca}^+$	$3d\,^2\text{D}_{5/2} \rightarrow 4p\,^2\text{P}_{3/2}$	854.4	144.9	23.4	3391	6.8
$^{115}\text{In}^+$	$5s^2\,^1\text{S}_0 \rightarrow 5s5p\,^3\text{P}_1$	230.7	66.7	0.37	24.7	33
$^{138}\text{Ba}^+$	$5d\,^2\text{D}_{3/2} \rightarrow 6p\,^2\text{P}_{1/2}$	649.9	212.8	20.1	4277	3.4
$^{171}\text{Yb}^+$	$6s\,^2\text{S}_{1/2} \rightarrow 6p\,^2\text{P}_{1/2}$	369.5	129.9	19.6	2546	9
$^{199}\text{Hg}^+$	$6s\,^2\text{S}_{1/2} \rightarrow 6p\,^2\text{P}_{1/2}$	194.3	73.5	119.4	8779	27

has been chosen close to the KATRIN voltage of −18.6 kV.

Among the different candidates, $^{115}\text{In}^+$ clearly sticks out. Due to the high mass, the UV transition and the narrow natural linewidth a sensitivity of $\kappa \cdot \Gamma_0 = 24.7$ mV is reached, being almost an order of magnitude better than that of Li^{+*}, the second-best candidate. Analyzing the different candidates further, even more advantages of indium become evident.

Indium has a melting point of 157 °C and is therefore one of the few metallic species that can be ionized in a Liquid Metal Ion Sources (LMIS). An LMIS provides high ion currents with superior beam properties since a very small emittance can be reached with beam-shaping apertures. The disadvantage of a wide energy distribution can be overcome using the pump-and-probe technique which is applicable because the level structure of $^{115}\text{In}^+$ with a nuclear spin of $I = 9/2$ allows optical pumping in the hyperfine substates. In the $^1\text{S}_0$ ground state a redistribution of the pumped population is slow since the magnetic moment is exclusively of nuclear origin and therefore small. Due to its relatively large mass, In^+ is also less susceptible to frequency shifts by the recoil of the absorbed photons than lighter elements. A disadvantage is the transition wavelength which is in the deep UV regime and requires a complex laser system based on, e.g., the fourth harmonic generation from infrared light at 922.7 nm. The price for the narrow natural linewidth is a small scattering rate. Furthermore, there is the risk that external broadening effects limit the benefits from the narrow linewidth.

The second best candidate Li^{+*} requires a more elaborate production technique since it is the metastable $1s2s\ ^3\text{S}_1$ state ($\tau = 50$ s) of the ion that is used for laser spectroscopy. The preparation of this metastable state requires a plasma discharge with production of Li^{2+} ions to populate the $^3\text{S}_1$ state through charge exchange reactions in the plasma. The excitation efficiency is limited to typically a few percent and the beam properties from such plasma sources are inferior to that of an LMIS. Hence, only a small fraction of the total beam intensity would be available for the fluorescence signal.

For beryllium, either a laser ion source or an electron impact ion source is required to generate an ionic beam, adding more complexity to the experimental setup. An advantage is the splitting of the ground state in two hyperfine levels that offers a very efficient pump-and-probe scheme. Krieger et al. used these ions to perform high-voltage measurements at ISOLDE and demonstrated relative uncertainties in the $5 \cdot 10^{-5}$ regime [21]. A drawback is the large photon-recoil shift that originates from the combination of low ion mass and the UV transition.

With a much lower sensitivity of $\kappa \cdot \Gamma_0 = 3.4$ V calcium seems inappropriate for accurate high-voltage measurements. But due to many practical advantages, e.g., the production in surface ionization sources,

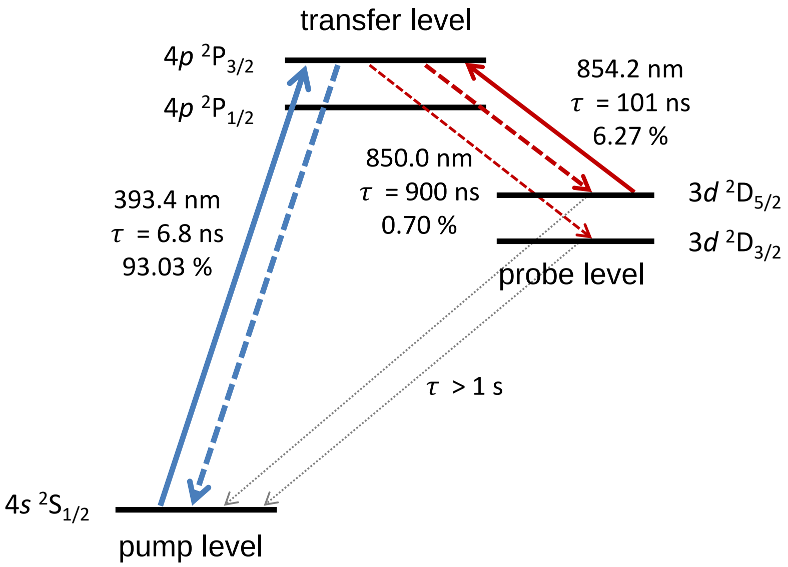

Figure 2.8: Relevant levels and transitions of $^{40}\mathrm{Ca}^+$. Exciting the ions from the $4s\ ^2S_{1/2}$ ground state to the $4p\ ^2P_{3/2}$ state (D2 transition), they will mostly decay back into the ground state. However, with a probability of 6.27 % the metastable $3d\ ^2D_{5/2}$ state is populated which has a lifetime much longer than the time of flight in the experimental setup. Hence, this state can be used to store the information of the initial ion velocity.

easily accessible transition frequencies and the efficient pump-and-probe scheme in a Λ-system, this ion species was found to be a good candidate for a proof of principle experiment. Therefore, Götte [19, 50] and later also Will [22, 51] have chosen Ca^+ ions to demonstrate laser-based high-voltage measurements.

2.3.1 Level scheme of Ca^+

To benefit from the experiences of Götte and Will, Ca^+ ions were used at the ALIVE experiment for the commissioning of the setup as well as for first high-voltage measurements. With a fraction of 97 %, $^{40}_{20}\mathrm{Ca}$ is the most abundant of the naturally occurring calcium isotopes. The nuclear spin is $I = 0$ and hence, there is no hyperfine splitting. The relevant part of the Ca^+ level scheme is shown in Fig. 2.8.

The Λ-system consisting of the $4s$ ground state and the $4p$ and $3d$ excited states which both split into two fine-structure levels, can be used for pump-and-probe experiments as discussed in section 2.1.7. By driving the $s \rightarrow p$ transition in the pumping process, the d-state will be populated with a probability of 7 % for each excitation. This level is metastable with a lifetime of 1168(9) ms [52] since a transition into the ground state requires the angular momentum to change by $\Delta l = 2$ which is forbidden for an electric dipole transition. The time of flight of the ions through the complete experimental setup is of the order of a few µs and hence, it is an ideal probe level which keeps the velocity information of the excited ions. The $d \rightarrow p$ transition can be probed after acceleration to determine the velocity change.

Ideally the $^2S_{1/2} \rightarrow {}^2P_{1/2}$ (D1) transition is used for pumping because only the $^2D_{3/2}$ will be populated in this case but a corresponding laser system was not available. Exciting the $^2P_{3/2}$ state distributes the population among both 5d fine structure levels. However, the majority of 90 % will be transferred to the $^2D_{5/2}$ state and therefore, the reduction in efficiency is marginal. The atomic mass and the $s \rightarrow p$ as well as the $s \rightarrow d$ transition frequencies are well known and are listed in Tab. 2.4. The frequency of the probing transition can be calculated as

$$f_0(^2D_{5/2} \rightarrow {}^2P_{3/2}) = f_0(^2S_{1/2} \rightarrow {}^2P_{3/2}) - f_0(^2S_{1/2} \rightarrow {}^2D_{5/2}) = 350\,862\,882.82(8)\,\mathrm{MHz}\,. \tag{2.44}$$

Table 2.4: Atomic data of Ca$^+$ used as input values for calculating the high-voltage of interest from the Doppler-shifted laser frequency. Besides the atomic mass, the relevant rest-frame transition frequencies f_0 and the natural linewidth Γ_0 are listed.

atomic mass / u	$f_0(^2\mathrm{S}_{1/2} \rightarrow {}^2\mathrm{P}_{3/2})$ / MHz	$f_0(^2\mathrm{S}_{1/2} \rightarrow {}^2\mathrm{D}_{5/2})$ / MHz	Γ_0 / MHz
39.962 590 865 (22) [53]	761 905 012.599 (82) [40]	411 042 129.776 393 0 (16) [41]	23.4 [49]

The short lifetime of 6.8 ns of the $4p\ ^2\mathrm{P}_{3/2}$ level corresponds to a natural linewidth of $\Gamma_0 = 23.4\,\mathrm{MHz}$ for the $s \rightarrow p$ and the $d \rightarrow p$ transition. While being optimal for efficient pumping and sensitive detection, it limits the precision of the voltage determination.

2.3.2 Level scheme of In$^+$

As pointed out before, indium ions yield the best sensitivity $\kappa \cdot \Gamma_0$ and seem to be the most suitable candidate to perform high-voltage measurements. The $5s^2\ ^1\mathrm{S}_0 \rightarrow 5s5p\ ^3\mathrm{P}_1$ transition is in the deep UV regime (230.7 nm) and the upper level has a relatively long lifetime of $\tau = 440\,\mathrm{ns}$ since it is an intercombination transition that is forbidden in the LS-coupling scheme of orbital and spin angular momentum but becomes increasingly allowed for heavier atoms due to an increasing strength of jj-coupling. The lifetime corresponds to a natural linewidth of $\Gamma_0 = 366\,\mathrm{kHz}$ which is nearly two orders of magnitude smaller than the natural linewidth of the transition used in Ca$^+$. Transitions to the $5s5p\ ^3\mathrm{P}_0$ and $5s5p\ ^3\mathrm{P}_2$ levels are multiply forbidden and cannot be used since their lifetime is much too long to obtain a detectable fluorescence signal in collinear laser spectroscopy.

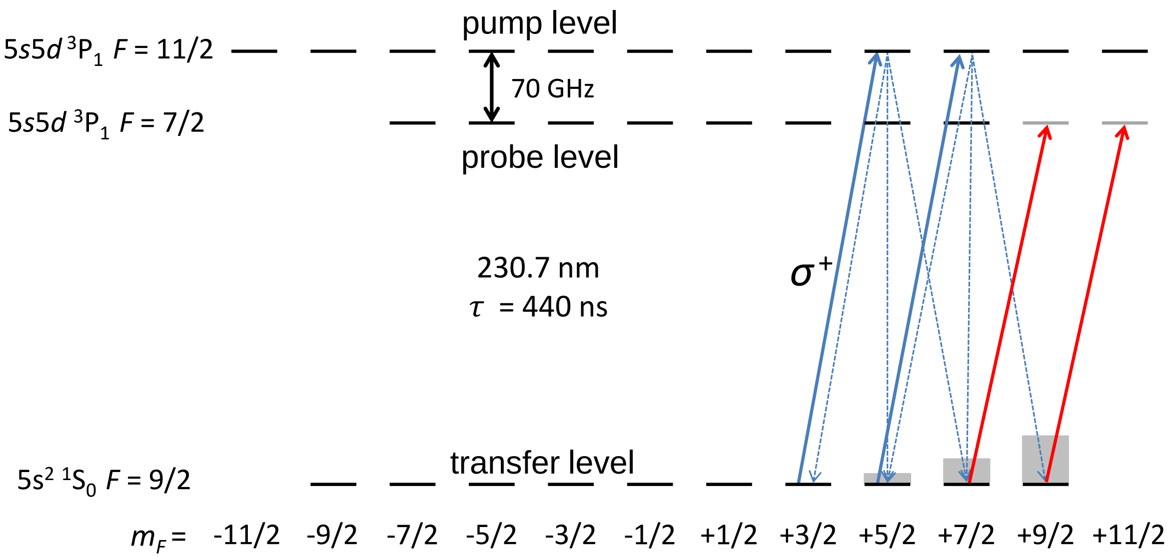

Figure 2.9: Relevant level scheme of In$^+$ with a possible realization of a pump-and-probe approach. Driving the $5s^2\ ^1\mathrm{S}_0\, F = 9/2 \rightarrow 5s5p\ ^3\mathrm{P}_1\, F = 11/2$ transition with circularly-polarized σ^+ light, the population of the magnetic substates in the ground state is shifted to high magnetic quantum numbers. After the acceleration the $^1\mathrm{S}_0\, F = 9/2 \rightarrow {}^3\mathrm{P}_1\, F = 7/2$ transition can be used for probing since the $m_F = 7/2$ and $m_F = 9/2$ substates are excluded from contributing to the resonance light leading to a dip in the resonance when scanning the velocity class manipulated during the optical pumping. For reasons of clarity only a few exemplary transition lines are depicted.

Table 2.5: Atomic data of In^+ used as input values for calculating the high-voltage of interest from the Doppler-shifted laser frequency. The rest-frame transition frequencies f_0 of the $5s^2\ ^1\mathrm{S}_0 \rightarrow 5s5p\ ^3\mathrm{P}_1$ transition are given for the center of gravity (cg) and the individual hyperfine components. The transition from the ground state with $F = 9/2$ to the excited stated with $F = 11/2$ is known with a relative accuracy of $8 \cdot 10^{-11}$ from an RF trap measurement in 2007 [54] whereas the other transitions were identified with an échelle monochromator in 1993 with much larger uncertainties [55]. Furthermore, the hyperfine constants A and B, the atomic mass and the natural linewidth Γ_0 are given.

property	value	reference
atomic mass / u	114.903 887 776 (12)	[49]
Γ_0 / MHz	0.366 (30)	[56]
$f_{0,\,\mathrm{cg}}(5s^2\ ^1\mathrm{S}_0 \rightarrow 5s5p\ ^3\mathrm{P}_1)$ / MHz	1 299 617 480 (150)	[55]
$f_0(F = 9/2 \rightarrow F = 11/2)$ / MHz	1 299 648 954. 54 (10)	[54]
$f_0(F = 9/2 \rightarrow F = 9/2)$ / MHz	1 299 610 830 (180)	[55]
$f_0(F = 9/2 \rightarrow F = 7/2)$ / MHz	1 299 578 990 (180)	[55]
A / MHz	6960 (90)	[57]
B/ MHz	−480 (420)	[57]

In contrast to $^{40}_{20}\mathrm{Ca}$, the most abundant (95.7 %) indium isotope $^{115}_{49}\mathrm{In}$ has a nuclear spin of $I = 9/2$ which leads to hyperfine structure splitting of the transition. The $5s^2\ ^1\mathrm{S}_0$ ground state does not split but the $F = 9/2$ hyperfine level is composed of 10 magnetic substates that offer the possibility to perform optical pumping in a V-system as discussed in section 2.1.7. The relevant level scheme and the most obvious approach to perform optical pumping is depicted in Fig. 2.9. Driving the $^1\mathrm{S}_0\, F = 9/2 \rightarrow {}^3\mathrm{P}_1\, F = 11/2$ transition with circularly-polarized light, the population of the magnetic substates in the ground state can be manipulated. If σ^+ light is used, the population is transferred to m_F states with larger quantum numbers whereas σ^- light will transfer the population to states with large negative m_F quantum numbers with respect to the light direction. The population transfer occurs only for the velocity classes that are in resonance and hence, this can be used to store information about the resonant interaction and velocity before the acceleration. After the acceleration, the $^1\mathrm{S}_0\, F = 9/2 \rightarrow {}^3\mathrm{P}_1\, F = 7/2$ transition can be used for probing. Using circularly-polarized light with the same orientation will exclude the $m_F = 7/2$ and $m_F = 9/2$ substates from contributing to the resonance light since there is no appropriate $m_F = 9/2,\ 11/2$ substate in the probe level. Hence, there will be less fluorescence in case that the probe laser interacts with the same velocity class as the pump laser did before which can be observed as a spectral feature in the total resonance signal.

However, this approach has several disadvantages for a high-voltage evaluation. As shown in Tab. 2.5 where the transition frequencies from the ground state to all three hyperfine levels of the $^3\mathrm{P}_1$ state are listed, only the $^1\mathrm{S}_0\, F = 9/2 \rightarrow {}^3\mathrm{P}_1\, F = 11/2$ transition is sufficiently well known to perform high-voltage measurements at the ppm level. It was measured on a single ion in an RF trap in 2007 with a relative accuracy of $8 \cdot 10^{-11}$ [54]. The other hyperfine transitions are only known to $1.4 \cdot 10^{-7}$ relative accuracy from a measurement with an échelle monochromator on light emitted from In^+ ions in a hollow-cathode source in 1993 [55] which is three orders of magnitude less accurate than required. They also measured the $^1\mathrm{S}_0\, F = 9/2 \rightarrow {}^3\mathrm{P}_1\, F = 11/2$ transition which disagrees by 265 MHz from the accurate value of [54]. A similar discrepancy of 277 MHz was also observed in the $5s^2\, ^1\mathrm{S}_0 \rightarrow 5s5p\, ^3\mathrm{P}_0$ transition when comparing it to [42] which is the most recent measurement of the so-called clock transition. This raises doubts on the claimed accuracy of [55]. Hence, it seems advisable to avoid the $^1\mathrm{S}_0\, F = 9/2 \rightarrow {}^3\mathrm{P}_1\, F = 7/2$ transition until a more accurate value is available. There are intentions to perform precise trap measurements of this transition [58] but those could not be realized by now. Another drawback of this approach for optical pumping is the shift of the transition frequency by the Zeeman effect when using circularly-

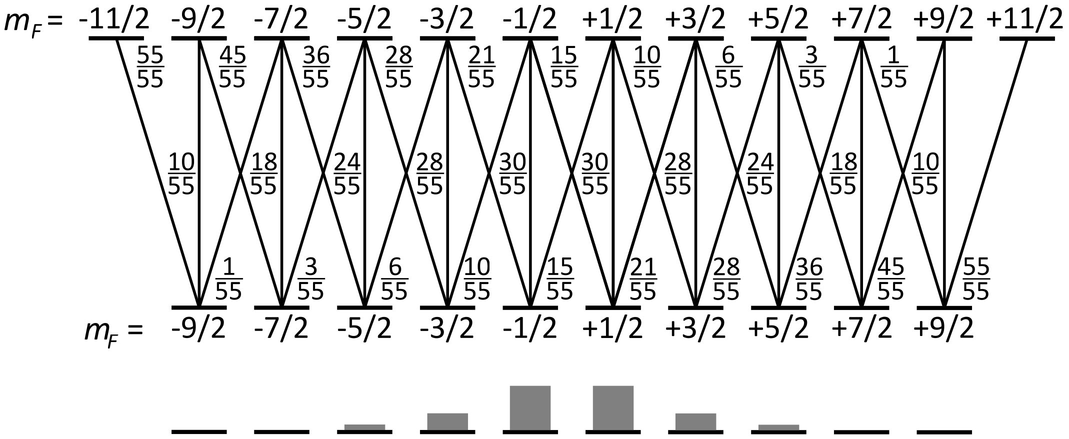

Figure 2.10: Transition strength of the $^1\mathrm{S}_0\, F = 9/2 \rightarrow {}^3\mathrm{P}_1\, F = 11/2$ transition of In$^+$ depending on the polarization of the photons and the magnetic quantum number m_F of the ground state and the excited state. Given are the quadratic Clebsch-Gordan coefficients. Performing optical pumping with linearly-polarized light will shift the ground state population to the center as indicated in gray underneath. During the probing process an additional peak can be observed since the transition strength of the manipulated velocity class is increased. The values have been calculated with the Clebsch-Gordan function implemented in Wolfram Mathematica.

polarized light (compare section 2.2.2).
To overcome these limitations, the $^1\mathrm{S}_0\, F = 9/2 \rightarrow {}^3\mathrm{P}_1\, F = 11/2$ transition can be driven with linearly-polarized light for performing optical pumping and probing. How this works can be understood by taking the transition strength between the different magnetic substates into account. As shown in Fig. 2.10 the transition strength based on different Clebsch-Gordan coefficients for linearly-polarized light is strongest for small absolute m_F quantum numbers. At large positive and negative m_F quantum numbers the linear transition is significantly weaker and the excited states will mostly decay in a way to decrease the absolute value of the magnetic quantum number. Hence, during optical pumping with linearly-polarized light the population distribution of the different m_F states will be changed to a symmetric distribution around small m values (alignment) for ions of the resonant velocity as indicated in Fig. 2.10. When probing these ions after the acceleration, the transition rates are higher compared to those which did not interact with the laser and have therefore equally populated magnetic substates. This leads to an increased fluorescence rate when probing the optically-pumped velocity class. In this approach, the transition frequency is well known and no shift due to the Zeeman effect is expected and, hence, the systematic uncertainty of a high-voltage evaluation can be drastically reduced. Additionally, the laser which drives the optical pumping transition can be used to perform the reference measurement since the same transition is used for pumping and probing. Therefore, no changes in the laser systems are necessary which allows fast changes between high-voltage and reference measurement. Hence, this approach is promising for performing accurate high-voltage measurements with In$^+$ ions.

2.3.3 Comparison of Ca$^+$ and In$^+$

The fundamental constants contributing to the high-voltage evaluation are sufficiently well known for Ca$^+$ as well as for In$^+$ and would allow measurements in the sub-ppm regime. As stated in Tab. 2.2, the uncertainties due to the experimental setup can also be reduced below the ppm level by applying the reference-measurement approach. But to reach the given limit, high requirements on the ion beam have to be fulfilled. This is hardly possible with a typical surface ionization source that is usually used for the production of Ca$^+$ ions. The In$^+$ ion beam properties are much better due to the advantages of the

LMIS. The low emittance leads to a small ion beam. Hence, the alignment and the resulting uncertainty $\delta U_{\mathrm{angle}}$ can be controlled much better. Also a good collimation of the ion beam can be achieved easier which is necessary to cancel δU_{div}. Due to the smaller differential voltage sensitivity κ, the impact of all other uncertainties occurring in frequency space is reduced by more than a factor two.

Besides the smaller systematic contributions, the resonance frequency can be identified more accurately in case of In^+ since the natural linewidth is much narrower. Here, the required precision of about 100 kHz should be feasible allowing to aim for sub-ppm accuracies in the high-voltage evaluation, if external broadening contributions are under control and the smaller scattering rate is still sufficient to allow for efficient optical pumping.

2.4 Linewidth and lineshape

The precision in laser spectroscopy is limited by the linewidth of the resonance which is often much larger than the natural linewidth since several broadening mechanisms are usually at work. While a symmetric broadening will primarily affect the precision, accuracy will suffer from asymmetric broadening. Since the lineshape becomes model-dependent in this case, a systematic uncertainty has to be added to the extracted center frequency.

In collinear laser spectroscopy, the largest contributions to the broadening of the linewidth are typically caused by effects in the ion source and strongly depend on the type of source. In hot sources the thermal velocity distribution of the ion beam leads to a large Doppler broadening. The different velocity classes are in resonance with different laser frequencies due to different Doppler shifts yielding a broad resonance signal. This effect is strongly reduced in collinear laser spectroscopy by accelerating the ions but usually still covers several 10 MHz. Potential differences inside the source and ripples on the acceleration voltage lead to additional contributions and can even break the symmetry of the velocity distribution. In field ionization sources the linewidth is dominated by the large initial energy distribution of the ions, since the point of ionization is located in the strong electrostatic field with corresponding steep variations in potential. Furthermore, bad vacuum conditions which usually come along with each type of ion production lead to an (asymmetric) broadening of the velocity distribution by elastic as well as inelastic collisions with residual gas.

However, in a pump-and-probe approach the initial linewidth is irrelevant since a new, narrow velocity class of ions is transferred into the probe level during the pumping process. Hence, the contributions due to effects in the ion source will not be discussed here in detail, but can be found in [59] and in its consequences to measurements at this setup in [60]. Nevertheless, the linewidth is still dependent on several effects but these have a smaller impact and can be described more precisely. The total linewidth is then given by the convolution of all broadening effects which have to be considered twice in a pump-and-probe experiment since the broadening will take place in the pumping as well as in the probing process.

2.4.1 Natural linewidth

The lowest limit for the linewidth of a transition is given by its natural linewidth. Applying the model of a damped harmonic oscillator to the excited atom or ion, the intensity I of the transition between two energy levels $E_2 - E_1 = hf_0$ can be described by the area normalized Lorentzian function

$$I(f) = \frac{\Gamma_0/2\pi}{(f-f_0)^2 + (\Gamma_0/2)^2} \tag{2.45}$$

where Γ_0 defines the full width of half maximum (FWHM) of the Lorentzian. It is called the natural linewidth of the transition and is related to the lifetime τ of the excited state by $\Gamma_0 = 1/2\pi\tau$. Alternatively, this correlation can also be described by Heisenberg's energy-time-uncertainty relation. The limited lifetime τ of the excited state which is linked to the Einstein coefficient for the spontaneous decay A_{21}, leads to an energy width of the transition of

$$\Gamma_0 = \frac{\Delta E}{h} = \frac{A_{21}}{2\pi} = \frac{1}{2\pi\tau} \ . \tag{2.46}$$

If more than one transition is possible, the lifetime of the excited state becomes smaller and hence, the linewidth larger

$$\Gamma_0 = \frac{1}{2\pi}\left(\frac{1}{\tau_1} + \frac{1}{\tau_2} + \ldots\right) \ . \tag{2.47}$$

Besides the natural linewidth, further contributions based on the experimental conditions will lead to an increased linewidth of a transition. Those which are important for the laser-based high-voltage evaluation will be discussed further.

2.4.2 Power broadening

For low laser intensities I, the transition rate between ground state and excited state as well as the excited state population increase linearly with increasing laser power. Once the rate of stimulated emission becomes a significant part of the relaxation process, it leads to a saturation of the number of excited ions. At first, the center of the resonance is saturated whereas the edges of the Lorentzian are not. Hence, the transition rate at the edges increases more strongly with increasing laser power leading to a larger linewidth which still has a Lorentzian shape.
For an ideal two level system, the saturation intensity I_S describes the laser intensity at which the rate of induced emission is equal to the spontaneous relaxation rate and depends on the natural linewidth of the transition with the lifetime τ of the upper state and the wavelength λ_0 [61]

$$I_\mathrm{S} = \frac{\pi h c}{3\lambda_0^3 \tau} \ . \tag{2.48}$$

The power-broadened Lorentzian linewidth Γ_S is given by

$$\Gamma_\mathrm{S} = \Gamma_0 \sqrt{1 + \frac{I}{I_\mathrm{S}}} \tag{2.49}$$

and increases at the saturation intensity by a factor $\sqrt{2}$.

2.4.3 Transit-time broadening

If the interaction time between ions and laser is in the similar range or even smaller than the lifetime of the excited state, transit-time broadening takes place. In this case the linewidth is not defined by the lifetime but by the interaction time. The reason is the energy-time uncertainty which limits the accuracy ΔE of an energy measurement within a given measurement time Δt to $\Delta E \cdot \Delta t \geq \hbar/2$.
In a typical setup, the ions enter the resonant laser field through a short acceleration into the interaction region. Therefore, the laser-ion interaction time T can be approximated as a rectangular function. Calculating the resulting intensity distribution of the resonance yields [59]

$$I(f) = C \, \frac{\sin^2(\pi(f - f_0)T)}{(f - f_0)^2} \ , \tag{2.50}$$

where C is a normalization constant. This $\sin^2(x)/x^2$ shaped function is symmetric and the full width at half maximum is given by [59]

$$\Gamma_{\mathrm{tof}} = \frac{5.6}{2\pi T} = \frac{5.6}{2\pi}\frac{v}{s} \approx \frac{v}{s} \; . \tag{2.51}$$

Medium-mass ions with a kinetic energy of several keV have a velocity of $v \approx 0.25\,\mathrm{m/\mu s}$. For a typical length of 25 cm of the optical-detection region, we obtain $\Gamma_{\mathrm{tof}} = 0.25\,\mathrm{m/\mu s}/0.25\,\mathrm{m} = 1\,\mathrm{MHz}$. The interaction time can be shorter, if the overlap of both beams is not ensured during the whole passage through the interaction region or if potential changes, e.g., due to contact voltages, lead to different Doppler shifts which reduces the resonant interaction time. Furthermore, if ion species with long-living excited states are used, the effective length of the interaction region is reduced. As it will be discussed in detail in section 5.3.1, most of the fluorescence light from the ions excited right after entering the interaction region can be observed. These ions have experienced a much larger transit-time broadening due to the short interaction time than the ions excited at the end of the interaction region whose fluorescence cannot be observed anymore since they leave the optical detection region before decaying. This limits the usage of forbidden transitions for collinear laser spectroscopy since the width will finally be limited by transit-time broadening.

2.4.4 Zeeman broadening

As discussed in chapter 2.2.2, an external weak magnetic field B will lead to Zeeman splitting of the formerly degenerated magnetic substates

$$\Delta E_{\mathrm{Zeeman}} = g m \mu_B B \; . \tag{2.52}$$

with the Landé factor g, the quantum number m of the magnetic substates and the Bohr magneton μ_B. For the earth magnetic field, this splitting is of the order of some 100 kHz and hence, cannot be resolved. This leads to a broadening and a deformation of the initial lineshape since the resulting transition width is the superposition of all individual lines. However, the resulting lineshape stays symmetric and its consequence on the lineshape strongly depends on the relation between Zeeman splitting and natural linewidth.

2.4.5 Spectral width of the laser and voltage ripples

Applying the post-acceleration voltage and the scan voltage for Doppler tuning leads to an acceleration of the ions. If there are fluctuations on these voltages, the former narrow velocity class will be broadened since different ions experience different accelerations at different times. Typically, the noise induced from a high-voltage power supply is of the order of $10^{-4} - 10^{-5}$ of the applied voltage. For a post-acceleration voltage of $U_{\mathrm{HV}} = 10\,\mathrm{kV}$ this leads to fluctuations of 100 mV - 1 V and can cause a broadening of several MHz. Therefore, an ultra-low noise device with only $20\,\mathrm{mV_{pp}}$ at 50 Hz will be used for generating the high-voltage of interest.

Although all effects before and during the pumping cancel in the reference-measurement approach, a ripple on the voltage U_{pump} applied to the pumping section will also lead to a broadening. When leaving the pumping region, the ions will be accelerated to the next section. Hence, U_{pump} defines the starting potential of the optically-pumped ions and a ripple on this voltage would lead to a broadening of the corresponding velocity class. Since here only voltages of about 100 V are required a standard high-voltage power supply with $15\,\mathrm{mV_{pp}}$ noise is used.

Also the laser itself can contribute to the resulting linewidth since its spectral width will be convoluted with the linewidth of the transition to the observable linewidth. The typical spectral width of the laser systems used at the ALIVE experiment is in the order of some 100 kHz, depending mainly on the stabilization scheme and the technical noise on the system. If the second harmonic or even the fourth harmonic of the fundamental laser light is generated, the resulting absolute spectral width will increase by a factor of $\sqrt{2}$ or 2, respectively [62].

2.4.6 Doppler compression

As already discussed in section 2.1.1, the acceleration of the ion beam will compress the velocity distribution. Since it is the width of the velocity class of the ions in the probe state that defines the transition linewidth, it will be reduced during the post-acceleration.
The compression factor K can be directly calculated when comparing the differential voltage sensitivity (see section 2.2.1 and 2.3)

$$\kappa(U, f_0) = \frac{\sqrt{2qUmc^2}}{f_0 q} \,. \tag{2.53}$$

before and after the post-acceleration $K = \kappa(U_{\text{start}})/\kappa(U_{\text{start}} + U_{\text{HV}})$. Especially if different post-acceleration voltages are applied, this will lead to different probing linewidths and has to be considered in the analysis.
Using different transition frequencies f_0 for pumping and probing will affect the resulting linewidth equivalently.

2.4.7 Other contributions to the lineshape

Besides the Doppler compression, the post-acceleration will deform the lineshape, since the faster end of the velocity class is less compressed than the slower part due to the energy-velocity relation. This effect was simulated for typical acceleration voltages at the ALIVE setup in [63]. The shift of the line center turned out to be in the regime of several Hz when using a Lorentzian or Voigtian profile for fitting.
Also a divergent laser beam can cause a small asymmetry. Simulating the resulting lineshape for typical conditions lead to a deviation in the frequency determination of the order of 1 kHz when applying a Lorentz or a Voigt fit [63]. At the current level of accuracy these effects can be disregarded.
A much larger asymmetric deformation of the resulting lineshape is caused in case of a strongly-structured initial velocity distribution. During optical pumping this underlying structure will influence the distribution of ions transferred into the probe state and becomes largest, if the structure is of the order of the transition linewidth. After analyzing the experimental conditions, the remaining uncertainty can be quantified and will be discussed in section 4.2.4 for Ca^+ and in section 5.3.3 for In^+.
The recoil of the fluorescence photon emitted when the ion is transferred into the probe level causes a broadening as discussed in section 2.2.8. Depending on the amount of laser-ion interactions, the ion mass and the wavelength of the emitted photon, the linewidth is increased by several kHz.

2.4.8 Resulting lineshape

Taking all effects into account, the total linewidth and shape can be estimated and an appropriate fit function defined. Performing pump-and-probe measurements, the linewidth and shape of both, the pumping and the probing transition have to be considered since the resulting lineshape will be a convolution of both transitions. In particular this means that the total linewidth will be broader than the width expected just from the probing transition because the probed velocity class has a certain distribution depending on the linewidth of the pumping transition.
In Tab. 2.6 the contributions of the different broadening effects discussed in the previous sections are summarized for typical settings. These are laser powers of 1 mW for the optical pumping and 0.5 mW for the probing with 4-mm^2 sized laser beams in case of Ca^+. For In^+, a laser power of 1 mW and a beam size of 2 mm^2 are assumed. The spectral width before frequency doubling of all lasers is estimated to be

Table 2.6: Contributions to the resulting lineshape of the pumping and probing transitions of Ca^+ and In^+ for a starting energy of 15 keV and a post-acceleration voltage of −20 kV. In case of Ca^+, a laser power of 1 mW was estimated for the optical pumping in a 1.2-m long drift tube whereas the probing took place in a 0.25-m long interaction region with a laser power of 0.5 mW. The 4-mm^2 sized laser beams are expected to have a spectral width of 200 kHz before frequency doubling. For In^+, a laser power of 1 mW and a 2-mm^2 sized beam are assumed for pumping and probing. The transit-time broadening of In^+ has been simulated explicitly to consider the long-lived excited state and the limited length of the optical detection region which is discussed in section 5.3.1. Due to the Zeeman effect, several slightly shifted transitions occur. Here, the number of transitions and their distance in frequency space is stated. In both cases asymmetric contributions due to the underlying initial velocity distribution are considered (compare section 4.2.4 and section 5.3.3).

	Ca^+ pumping	Ca^+ probing	In^+ pumping	In^+ probing	shape
Transition wavelength	393.4 nm	854.2 nm	230.7 nm	230.7 nm	
Natural linewidth	23.4 MHz	23.4 MHz	366 kHz	366 kHz	Lorentzian
Transit-time broadening	220 kHz	1.6 MHz	130 kHz	2.1 MHz	$\sin^2(x)/x^2$
Power broadening factor	1.22	1.88	3.74	1.81	
Zeeman broadening	2; 440 kHz	2; 90 kHz	10; 180 kHz	10; 180 kHz	
Laser linewidth	400 kHz	200 kHz	800 kHz	800 kHz	Gaussian
Photon recoil	32 kHz	-	33 kHz	-	Gaussian
Voltage ripple	350 kHz	140 kHz	350 kHz	300 kHz	Gaussian
Asymmetry contributions	± 150 kHz	-	± 10 kHz	-	asymmetry
Width reduction factor K_λ	0.46	-	-	-	
Width reduction factor K_{HV}	0.65	-	0.65	-	
Total width reference	13.2 MHz	56.1 MHz	2.3 MHz	4.8 MHz	
Total width HV	8.6 MHz	50.6 MHz	1.4 MHz	4.9 MHz	

200 kHz. All values are calculated for an initial acceleration voltage of $U_{start} = 15$ kV, a post-acceleration voltage of $U_{HV} = 20$ kV, a 1.2-m long pumping section and a 25-cm long probing region.

The natural linewidth represents the narrowest limit that can be achieved for vanishing laser power and no further broadening effects. With higher laser power, the linewidth is increased by power broadening as discussed in section 2.4.2. The broadening factor has been calculated using Eq. 2.48 which is only valid for a two-level system like In^+. On the contrary, this relation is not valid for the Λ-system of Ca^+ anymore. But by considering all decay channels and applying the reduced lifetime, this can still be seen as an acceptable approximation to get an estimate for the power broadening. In case of the probing transition of In^+, it is not the natural linewidth that defines the transition width but the width resulting from the short interaction time. The determination of this transit-time broadening which also takes the long lifetime of the excited state and the movement of the ion through the optical detection region into account, is explained in section 5.3.1.

Due to the Zeeman effect, the degeneracy of the magnetic substates is lifted and the individual $m \rightarrow m'$ transitions have different energies. In Tab. 2.6 the number of transitions in case of linearly-polarized laser light is stated and the frequency shift between two lines is calculated for the earth magnetic field. Since the energy difference is smaller than the linewidth, the individual Zeeman transitions cannot be resolved and the superposition of all transitions with a respective line broadening will be observed. For Ca^+ this contribution is negligible compared to the natural linewidth and will not affect the lineshape. Contrary, in In^+ it is a major contribution due to the large amount of possible transitions.

The lineshape is affected asymmetrically during the optical pumping process, the acceleration and the interaction with a divergent laser beam. While the latter effects are negligibly small, optical pump-

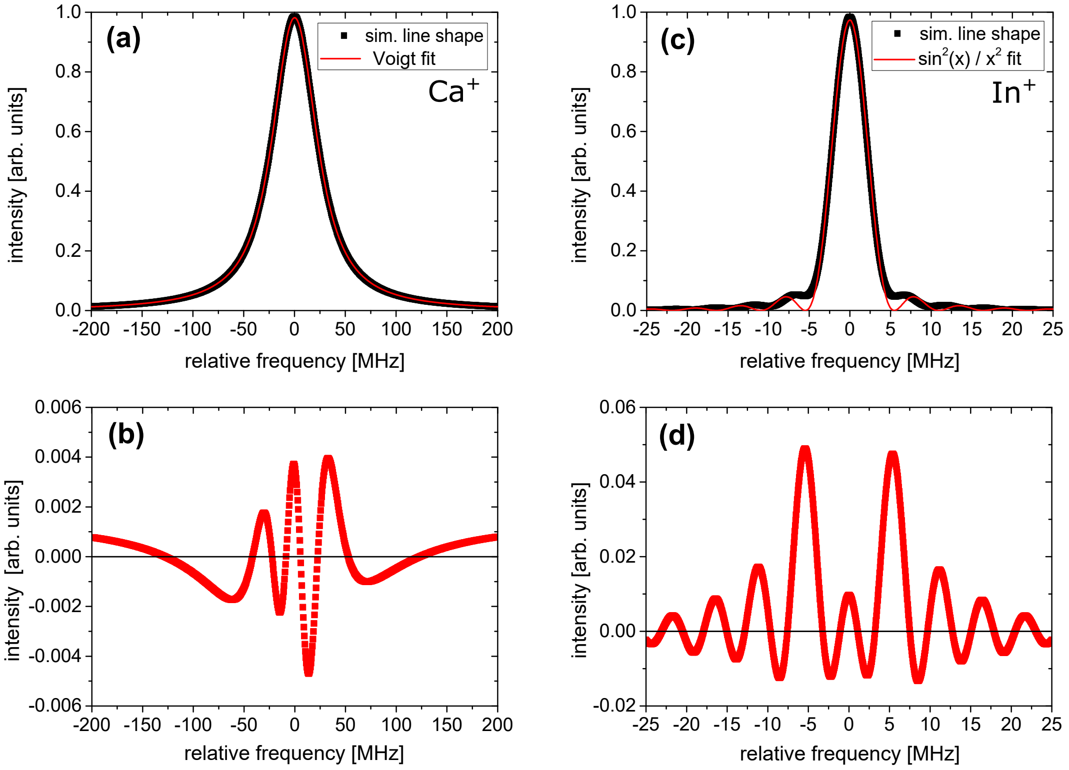

Figure 2.11: Simulation of the resulting lineshape of the probing transition of Ca^+ (a) and In^+ (c). The simulated lineshape of Ca^+ can be well described by a Voigt function while the lineshape of In^+ is described by a $\sin^2(x)/x^2$ function due to the large transit-time broadening contribution. (b) and (d) show the residuals between the simulated shape and the symmetric fit function. The lineshape is slightly asymmetric due to an underlying structure of the initial velocity distribution (compare section 4.2.4 and section 5.3.3).

ing into a strongly-structured initial velocity distribution can cause a significant deformation. In the reference-measurement approach the consequences due to this asymmetry is reduced when comparing the high-voltage measurement with the reference measurement but it can still lead to an uncertainty in the high-voltage evaluation in the 1-ppm regime.

Taking all effects into account, shape and width of the optically-pumped velocity class can be identified as a convolution of the initial velocity distribution, the transition lineshape for optical pumping, the spectral width of the laser and the voltage ripple. This velocity class will be compressed during the post-acceleration by the width compression factor $K_{HV}(20\,\mathrm{kV}) = 0.65$ introduced in section 2.4.6. The width is compressed even further for Ca^+ since two different transitions are used for pumping and probing and the differential voltage sensitivity κ is much larger for the probing transition. Hence, an additional width compression of $K_\lambda = \kappa(393\,\mathrm{nm})/\kappa(854\,\mathrm{nm}) = 0.46$ reduces the width of the optically-pumped velocity class in total to 1/3 of the initial width. In case of a reference measurement where no post-acceleration voltage is applied K_{HV} is not applicable. The lineshape detected when probing the ions results from the convolution of the compressed velocity class with the lineshape of the probing transition, the spectral width of the corresponding laser and the ripple of the voltage applied to the second interaction region.
Simulating the resulting lineshape (more details in appendix A) for the former discussed input parameters yields the profiles depicted in Fig. 2.11. As illustrated in (a), the lineshape of Ca^+ can be well described by a Voigt profile ($\Gamma_{FWHM} = 51\,\mathrm{MHz}$) with a large Lorentzian (45 MHz) and a small Gaussian (16 MHz) contribution. The linewidth is dominated by the power broadening of the probing transition. Hence, changes in the laser power or in the laser beam diameter can lead to significant changes in the

width of the observed signal. Since the direction of the asymmetric contribution is not predetermined, a symmetric Voigt function is used for fitting. This can lead to deviations of about 100 kHz corresponding to an uncertainty in the high-voltage evaluation of up to 0.5 ppm.

When probing In^+, an additional peak will be observed on top of the resonance signal. In Fig. 2.11c only this spectral feature is shown. The lineshape is dominated by the $\sin^2(x)/x^2$-like shape due to the transit-time broadening which has also been used for fitting. Even though there is additional broadening due to the Zeeman effect, the spectral width of the laser and the voltage ripple, the transition lineshape can be well reproduced yielding a width of $\Gamma_{\mathrm{FWHM}} \approx 5\,\mathrm{MHz}$ for the high-voltage and the reference measurement. The Doppler compression is more than compensated by the larger transit-time broadening in case of the post-accelerated beam ($\Gamma_{\mathrm{tof}}(35\,\mathrm{keV}) = 2.13$ MHz compared to $\Gamma_{\mathrm{tof}}(15\,\mathrm{keV}) = 1.55$ MHz) which is discussed in more detail in section 5.3.1. Due to the small linewidth of the pumping process and a broader initial velocity distribution, the asymmetric contribution is much smaller and can be neglected.

For both ion species the linewidth is increased significantly compared to their natural linewidth. In case of Ca^+, a broadening by a factor of 2.2 is expected, reducing the sensitivity for the high-voltage evaluation to $\kappa \cdot \Gamma(\mathrm{Ca}^+) = 7.3\,\mathrm{V}$. Due to the immense transit-time broadening, the linewidth of In^+ is increased by a factor of 13. Hence, its main advantage cannot be fully exploited and the adapted sensitivity is $\kappa \cdot \Gamma(\mathrm{In}^+) = 0.32\,\mathrm{V}$ which is still more than one order magnitude better than in case of Ca^+.

3 Experimental setup

A nearly 7-m long ultra-high vacuum beamline for collision-free ion transport is the most essential part of the ALIVE experiment. It contains all important components for a laser-based high-voltage measurement like the ion source, the post-acceleration section and two interaction regions whereof one is equipped with an optical-detection unit. Although developed for this purpose, this apparatus is not limited to high-voltage measurements but can be seen as a multi-purpose beamline for collinear laser spectroscopy in general [35].

In Fig. 3.1 an overview of the beamline, which can be separated in four vacuum sections, is shown. At first, the ions are produced in a source floated on a positive potential of typically 15 kV which defines the starting energy. Since the source is placed in a separate vacuum section, it can be easily exchanged while the ultra-high vacuum is preserved in the interaction regions yielding a high flexibility in the choice of the ion species. The produced ions are then accelerated towards the beamline at ground potential, collimated by an einzel lens and directed by a horizontal and vertical deflector. With an electrostatic bender the ions are superimposed with the laser beams. These laser beams can be irradiated in collinear as well as in anticollinear direction but the setup is currently optimized for the anticollinear case.

Further ion optics in form of a quadrupole doublet and another steerer can be used for ion beam collimation and adjustment to establish and optimize the overlap of ion and laser beam. This superposition can be checked in two diagnostic chambers, one right after the second steerer and one at the end of the beamline. Both chambers are equipped with dedicated beam diagnostic elements allowing us to ensure a good superposition in between the two diagnostic chambers, where the first interaction region IR1, the post-acceleration stage and the second interaction region IR2 with the fluorescence detection system are located. At the end of the beamline the ions are deflected into a beam dump, which allows an online monitoring of the ion current.

In this chapter, the most important sections of the beamline will be discussed in detail and the laser system as well as the conventional method to measure high voltages based on a voltage divider serving as reference for the laser-based measurements, will be presented.

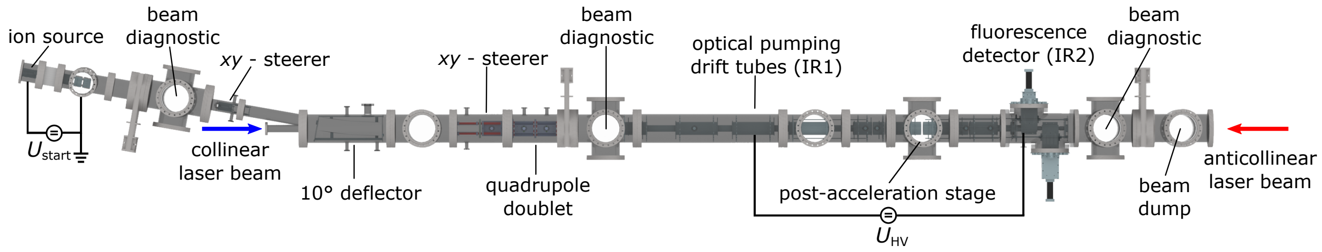

Figure 3.1: Overview of the ALIVE beamline. In the nearly 7-m long ultra-high vacuum beamline several ion-optical devices can be used to achieve a good superposition of ion and laser beam. Except of the ion source, the vacuum chambers are on ground potential. However, several inner sections, e.g., the interaction regions and the post-acceleration stage can be floated on a high potential which allows to apply the high-voltage of interest U_{HV} to accelerate the ions before the second laser-ion interaction in IR2.

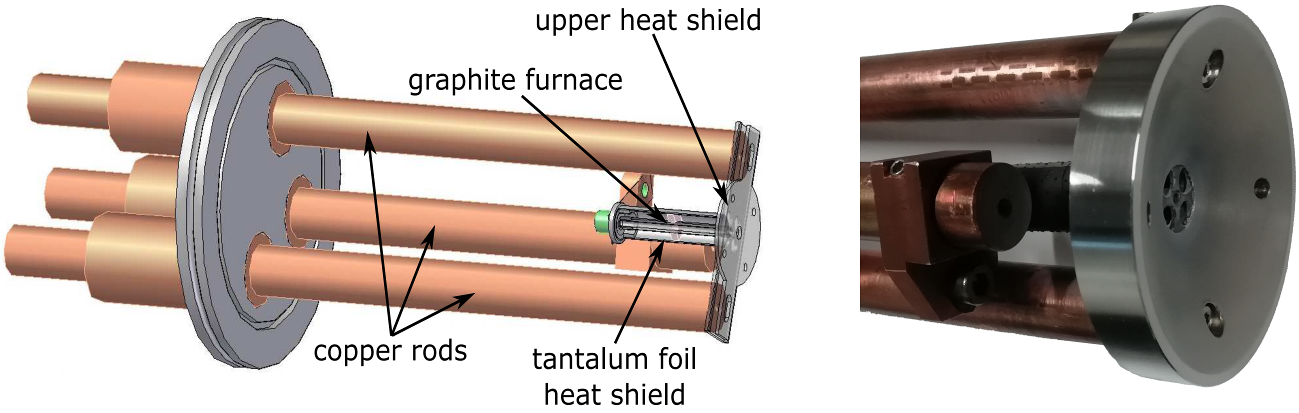

Figure 3.2: Surface ionization source consisting of a heated graphite furnace with tantalum heat shields. Heating currents of up to 100 A can be applied through three massive copper rods [64]. A Pierce-shaped electrode (right) was attached to generate a well-shaped ion beam.

3.1 Surface ionization source

Singly-charged ions from elements with small ionization potentials like alkaline and earth-alkaline elements can be produced in surface ionization sources. Since those consist basically only of a hot crucible, they are easy to manufacture and uncomplicated in operation. Hence, this type of ion source is the ideal candidate for the production of Ca^+ ions.

The ion source used at the ALIVE experiment was formerly constructed and employed at the TRIGA-Laser experiment in Mainz [64] and is based on a design from [65]. As shown in Fig. 3.2, it consists of three massive copper rods to apply the heating current to a 50-mm long and 4.3-mm diameter graphite tube with a 2-mm diameter bore. With additional tantalum heat shields, temperatures far above 2000 °C are accessible in the crucible which can be necessary for the ion production from elements with a low vapor pressure. The relation between the applied heating current and power, respectively, and the resulting temperature is plotted in Fig. 3.3a.

Through collisions with the surface, the vaporized atoms can be ionized. The probability of this process strongly depends on ionization energy E_{IP} of the atoms, the work function W_{A} of the furnace material and the temperature T. The ratio of emitted atoms n_0 and ions n_+ can be estimated from the Saha-Langmuir equation [66]

$$\frac{n_+}{n_0} = \frac{g_+}{g_0} \exp\left(\frac{W_{\mathrm{A}} - E_{\mathrm{IP}}}{k_{\mathrm{B}} T}\right) \tag{3.1}$$

with the Boltzmann constant k_{B} and the statistical weights of ions g_+ and atoms g_0. Since the ionization energy of calcium $E_{\mathrm{IP}} = 6.1\,\mathrm{eV}$ is larger than the work function of graphite $W_{\mathrm{A}} = 4.6\,\mathrm{eV}$ [67] the ionization efficiency is only about 0.02 % for temperatures of 2000 K. However, ion currents of a few nA can be generated which is sufficient for collinear laser spectroscopy.

To improve the ion beam properties, the upper heat shield was replaced with a Pierce-shaped electrode. Since it is the last electrode floated on the starting potential, its shape defines the electric field towards a flat extractor electrode on ground potential in a distance of 25 mm and hence, the shape of the resulting ion beam. After passing the extractor electrode, the ion beam can be collimated with an einzel lens before guiding it into the beamline. At the first diagnostic station an adjustable iris diaphragm is used to cut off the most divergent part of the ion beam to improve the ion-beam emittance.

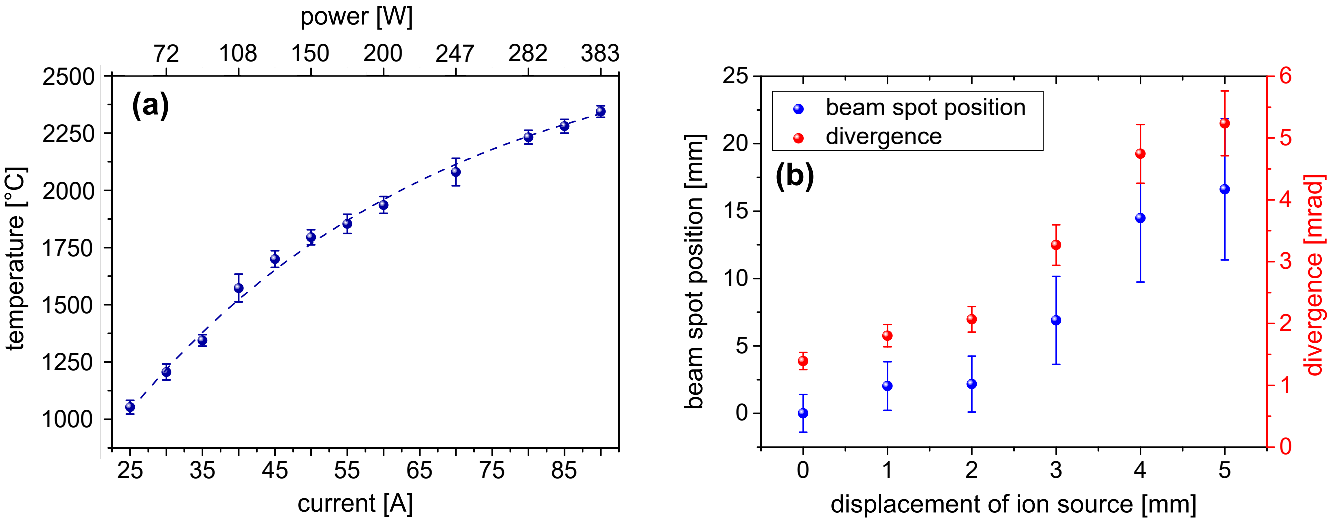

Figure 3.3: (a): Current-temperature dependence of the surface ionization source taken from [64]. Temperatures up to 2300 °C are accessible allowing the production of a variety of ion species. The power deposition for some heating currents is indicated on top.
(b): Simulated consequences of a misaligned ion source: The divergence of the ion beam increases with larger displacement of the source even though the einzel lens was optimized for each case. Furthermore, the beam position deviates from the central axis and the beam diameter, represented by the error bars, increases. These values are calculated at the position of the first xy-steerer.

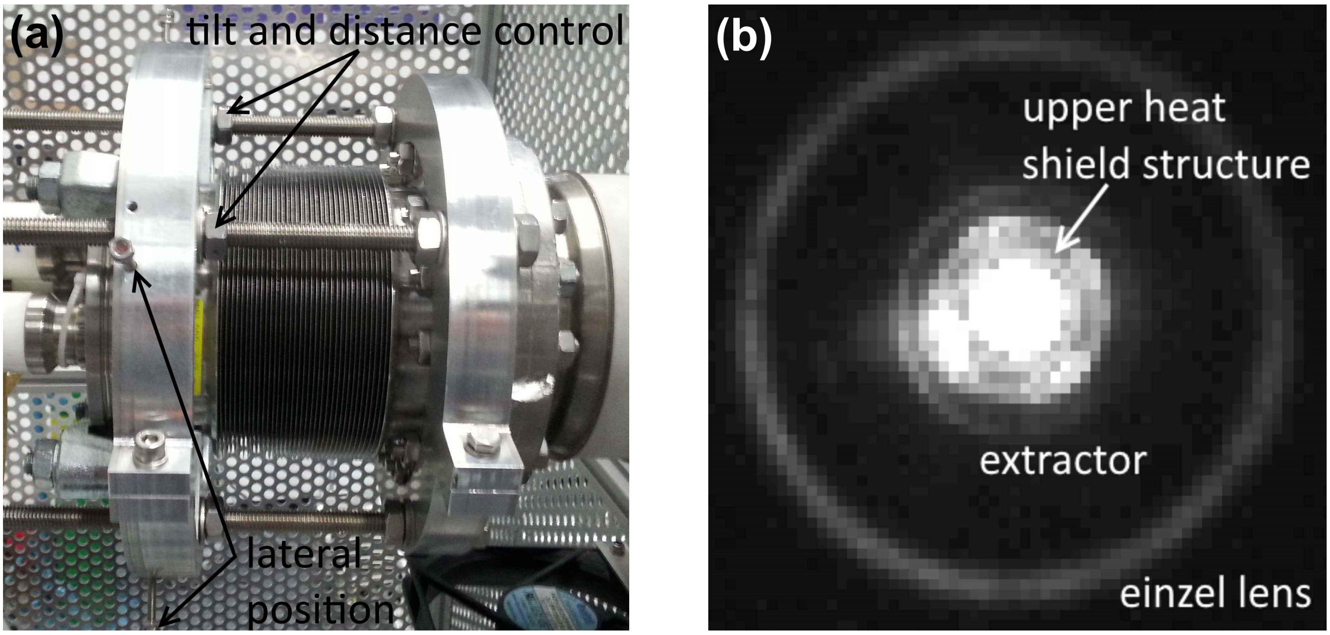

Figure 3.4: (a): Adjustment unit for the surface ionization source. Based on a welded bellow all translational and angular degrees of freedom can be controlled with several adjustment screws.
(b): Looking with the camera of DK1 at the heated furnace, the alignment of the source relative to the extractor and the einzel lens can be controlled.

3.1.1 Alignment of the surface ionization source

With the improved setup it becomes possible to generate a collimated ion beam if appropriate voltages for the einzel lens are chosen. In ion beam simulations with the software SIMION[1] it was shown that the required einzel lens voltage is about half of the high voltage U_{start} applied to the ion source to define the starting energy of the ions. This dependency could be confirmed in the experiment. However, some significant discrepancies were observed. In particular, the shape and the angle of the ion beam towards the central axis differed from the expectations. Further simulations pointed out that the position of the furnace relative to the center of the einzel lens is extremely crucial. A systematic analysis of the consequences of a shifted source on the ion beam diameter and the transverse deviation from the central axis at the first steerer as well as on the divergence is depicted in Fig. 3.3b. In these simulations the einzel lens voltage was adapted for each case to achieve the best possible collimation. As indicated in the diagram, even a small misalignment of the ion source increases the divergence of the ion beam and leads to a deflection. Displacements of more than 2 mm will cause large deviations from the central axis and considerable beam deformations occur, which cannot be fully corrected with ion-optical elements along the beamline. This diminishes the efficiency and accuracy of pump-and-probe experiments.

To enable a precise alignment, an adjustable unit based on a welded bellow was developed and installed between the ion source and the insulator to provide control of all translational and angular degrees of freedom. A picture of this adjustment unit is shown in Fig. 3.4 combined with a camera image of the view into the well-adjusted and heated furnace. The cloverleaf-like structure of the upper heat shield (compare Fig. 3.2) can be identified as well as the apertures of the extraction electrode and of the einzel lens which allows a positioning of the surface ionization source with a precision better than 0.5 mm.

3.2 Liquid Metal Ion Source

Liquid Metal Ion Sources (LMIS) can generate total emission currents of up to several mA [68]. Due to this high brightness, a low emittance can be reached with beam-shaping apertures while still ion currents of several nA are available which makes a LMIS the most suitable source for the production of singly-charged indium ions. The LMIS used at the ALIVE experiment was developed and constructed at the TU Dresden [69]. A technical drawing is shown in Fig. 3.5 and a short description of its components is given.

Applying a current to the heating wire enclosing the reservoir in the center, the indium which has a melting point of only 156.6 °C, becomes liquid. Capillary forces drag it to the top of a fine capillary. The reservoir and the capillary are floated on a high voltage whereas the extractor electrode which is only a few millimeters apart, is on ground potential. The small dimensions of the 150-µm thick capillary with a bore of 50 µm in diameter restrict the size of the Taylor cone which forms in the strong electric field. The emerging jet of atoms experiences a field strength of up to 10^8 V/cm [70] leading to field ionization of the evaporating beam. The resulting ion beam is strongly divergent due to the strong electric field and high space-charge effects yielding a normalized emittance of some $1000\,\pi\,\mathrm{mm\,mrad}\,\sqrt{\mathrm{eV}}$ [71, 70].

However, by cutting off the ions emerging under large angles with a 2-mm diameter aperture in a distance of 200 mm, a very low emittance can be achieved at the ALIVE setup. During this process the main part of the ion beam is lost as shown in Fig. 3.6. In typical operation conditions 4.86 kV are applied to the emitter leading to a total current of 10 µA. With a transmission efficiency of only 0.02 % an ion beam current of 2 nA is sent into the beamline.

With increasing high voltage the total emitted ion current increases linearly but the transmitted ion current saturates due to an increasing emittance of the emitted beam. This behavior is in good agreement with measurements on the current-dependent beam divergence on a similar indium LMIS performed in [72]. Taking the divergence angles determined in their measurement, the emittance of the ion beam

---

[1] SIMION™8.0 © 2003-2006 Scientific Instrument Services, Inc.

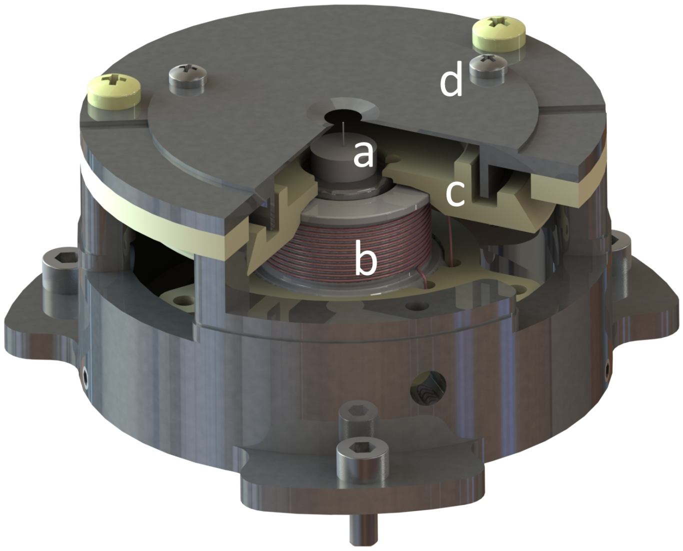

Figure 3.5: Design of the liquid metal ion source to be mounted on a CF100 flange [74].
(a): The emitter module consists of an indium-filled reservoir and a tiny capillary which are both floated on a high potential. Liquefied indium ascends the capillary where it forms a Taylor cone. Due to the strong electric field at the needle tip, a beam of singly-charged In^+ ions is emitted.
(b): The ceramic enclosing the emitter can be heated by a constantan wire. Temperatures of 220 °C are necessary to avoid a solidification of the indium at the top of the capillary.
(c): Peek insulator which isolates the extractor plate from the LMIS housing. A coating with indium is prevented by the special form of the insulator.
(d): Extractor plate of the LMIS which is only a few millimeter apart from the capillary. It has a Pierce-shaped opening for beam shaping. Furthermore, the extractor is isolated allowing to measure the current of impinging ions or to apply a negative voltage repelling secondary electrons.

after the aperture can be estimated to be about 10-50 π mm mrad $\sqrt{\text{eV}}$. Other ion sources have typically an emittance of some 100 π mm mrad $\sqrt{\text{eV}}$ [73] which demonstrates that a high-quality ion beam can be extracted in the described way.

3.2.1 Operation and alignment of the LMIS

To select the central part of the ejected ions, a small aperture had to be installed in front of the source. Since back-scattered electrons affect the stability of the LMIS quite strongly [75, 76] and to be able to select a small solid angle, a large distance of 200 mm was chosen. Additionally, the extractor plate of the LMIS (see Fig. 3.5 d) was floated on −300 V to deflect the electrons generated in collisions of the In^+ ions with the aperture material. The aperture was designed as an iris diaphragm movable in x and y direction and adjustable in size [77]. Therefore it becomes possible to align LMIS, aperture and the einzel lens which follows after an acceleration gap. The adjustable unit and a camera image of the aligned components are shown in Fig. 3.7. The adjustment process is facilitated by a faint light that is emitted from the top of the capillary under operation.
LMIS and aperture are floated on an additional voltage to increase the starting energy of the ions. The corresponding acceleration takes place between the aperture and the einzel lens which is the same as used for the surface ionization source. But due to the different geometry, here only 25 % of the total starting voltage of the ions has to be applied to collimate the ion beam. This configuration enables to run the LMIS itself in constant-current mode while the total ion energy is stabilized with the additional voltage yielding excellent conditions for laser spectroscopic experiments.

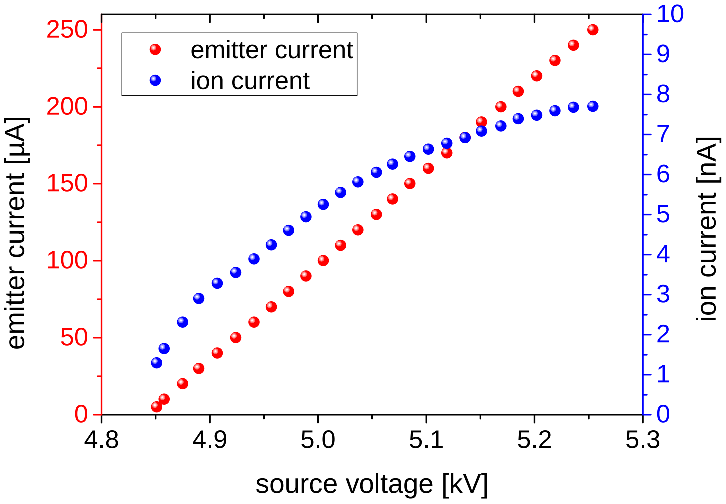

Figure 3.6: Dependency of the LMIS ion current from the applied high voltage for typical operation conditions. A potential difference of at least 4.85 kV is needed to generate an electric field, which is sufficient for field ionization. Running the ion source in constant-emitter-current mode, the required source voltage fluctuates only by several 100 mV and shows long-term drifts of the order of some V. After passing a 2-mm diameter aperture, the ions are accelerated by an additional high voltage to 15 keV and are measured with a Faraday cup. While the emitter current increases linearly with higher source voltages, the ion current behind the aperture saturates. This is due to the rising divergence of the emitted ion beam leading to higher losses at the aperture [72]. For emitter currents above 250 µA, the source voltage becomes less stable. During the experiment the LMIS was operated at an emitter current of 10 µA corresponding to an ion beam current of nearly 2 nA.

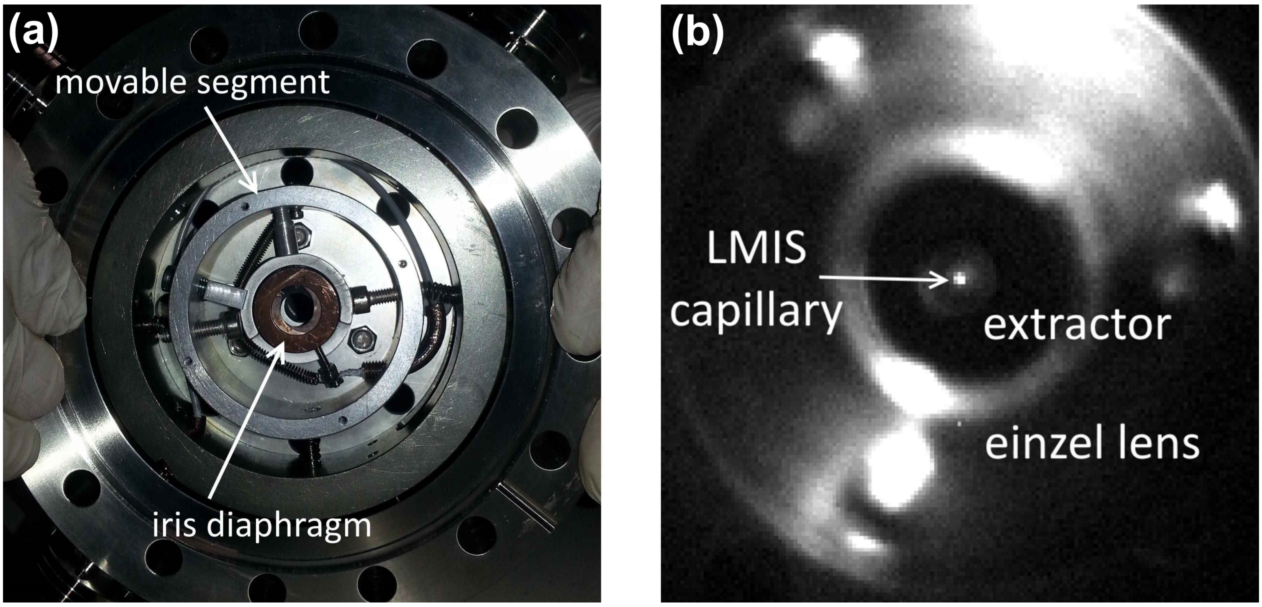

Figure 3.7: (a): Adjustable iris diaphragm without front cover. The horizontal and vertical position as well as the opening of the diaphragm can be controlled with three linear feedthroughs which allows to adjust LMIS, aperture and einzel lens. (b): Camera image of the aligned components.

To avoid uncertainties in the high-voltage measurement due to an angular misalignment, the position of the ion as well as of the laser beam has to be controlled precisely. Hence, in the ALIVE experiment three dedicated diagnostic chambers are equipped with different detectors to measure, adjust and control the beams. The first diagnostic chamber is placed right behind the einzel lens at the ion source (compare Fig. 3.1) whereas the other two diagnostic chambers are installed in front of the first interaction region and behind the second interaction region.

As depicted in Fig. 3.8, each diagnostic chamber is equipped with an iris diaphragm which can be opened or closed from outside. The position of the aperture is fixed and defines the central axis of both beams. Furthermore, all ion-optical elements were adjusted to this axis with an accuracy better than 0.5 mm. This is especially important for the post-acceleration stage since misaligned electrodes operated at high voltages have a large impact on the ion trajectory.

To ensure a proper alignment of the ion beam, a Faraday cup mounted on a vertical adjustment slide can be placed behind the iris aperture. By closing the aperture and monitoring the ion current, the ion beam can be precisely positioned. The standard Faraday cups have been replaced in 2018 by segmented Faraday cups with one inner and four outer electrodes, providing additional spatial resolution of the ion beam which allows to control the beam shape [78]. Alternatively, the beam shape can be monitored with a phosphor screen, which is also mounted on the adjustment slide. Since it is tilted by 45°, a camera placed outside the vacuum can observe the light generated by the impinging ions. The phosphor screen can also be used for the alignment of an anticollinear laser beam. In this case, the laser passes the iris aperture before hitting the backside of the phosphor screen. Since the thin phosphor layer is coated on a glass plate, the scattered laser light can be observed with the camera. The superposition of ion and laser beam can be checked easily by irradiating the screen simultaneously with both beams. In the first diagnostic chamber, the phosphor screen is replaced by a mirror to monitor and precisely adjust the ion source as shown in Fig. 3.4 and 3.7.

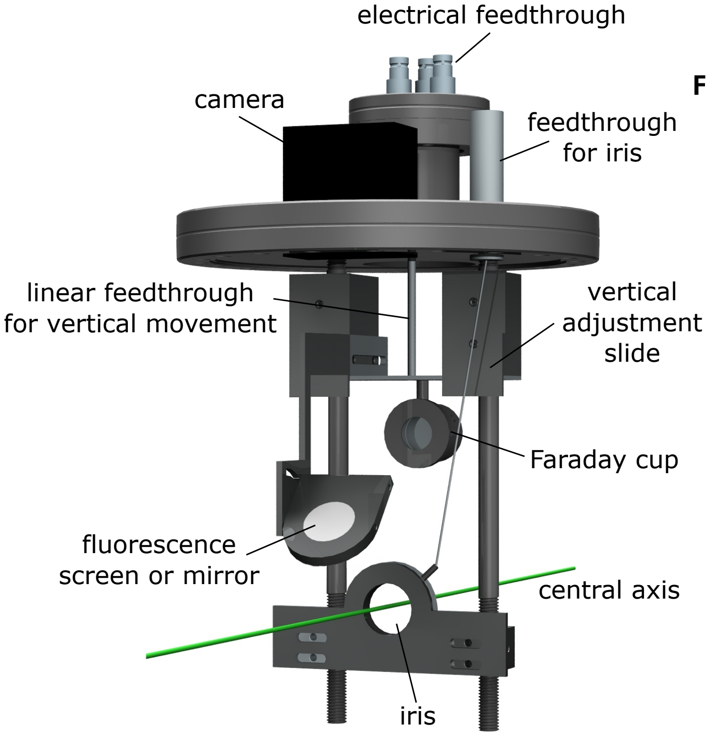

Figure 3.8: Beam diagnostic with iris diaphragm, Faraday cup and phosphor screen. The diaphragm is permanently installed in the beamline and its diameter can be changed from outside. It defines the central axis of the beams and all ion-optical elements are adjusted to this axis. Faraday cup and phosphor screen are mounted on a vertical adjustment slide. The cup can be positioned at the central axis to measure the ion current and position. The tilted phosphor screen allows to monitor the beam shape with a camera from outside the vacuum when placed at the central axis. Furthermore, it can be used for the alignment of an anticollinear laser beam.

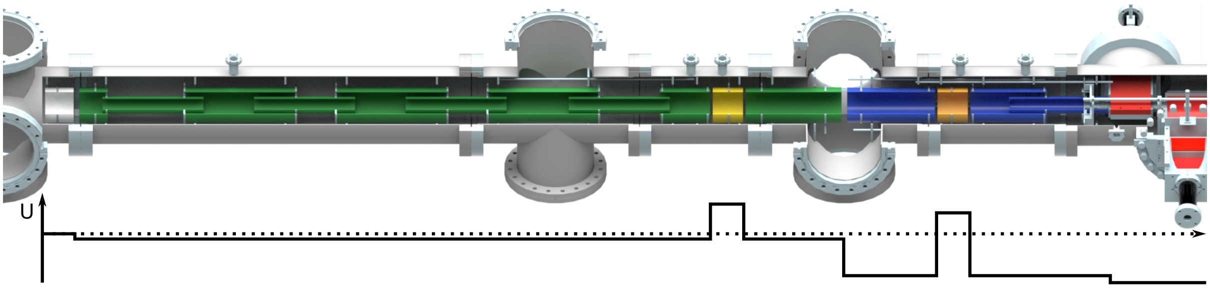

Figure 3.9: Interaction and post-acceleration regions. To ensure a long pumping region with a constant potential, a 1.2 m long array of drift tubes (green) floated on a potential of about $-100\,\mathrm{V}$ with respect to the beamline is installed. In front of the first drift tube for optical pumping another drift tube (white) with the same shape but on ground potential is placed to ensure a homogeneous electric field along the beam direction that is accelerating the ions into the drift tube. An einzel lens (yellow) in front of the acceleration gap and behind (orange) can be used as an ion-optical telescope to preserve the ion beam collimation. The drift tubes (blue) in front of the second interaction chamber (red) are floated on a potential close to the high-voltage of interest. Hence, the ions experience nearly the full acceleration but cannot interact with the laser beam before they enter the second interaction region with the optical-detection unit.

3.4 Optical pumping section (IR1)

In the first interaction region one velocity class is transferred into a dedicated state through optical pumping. A constant ion velocity inside the optical pumping chamber is substantial to avoid influences on the lineshape, broadening and shifts. Hence, the potential inside the tube needs to be homogeneous. Therefore, a 1.2-m long drift tube is installed at the ALIVE experiment, which consists of several shorter tubes with alternating diameters that overlap as shown in Fig. 3.9. To avoid optical pumping elsewhere, this drift tube is floated on a small negative potential of about $U_{\mathrm{pump}} \approx -100\,\mathrm{V}$ with respect to the beamline at ground potential. The field penetrations through the gaps have been simulated and the potential variation inside were found to be less than 0.1 ppm. The geometry has been chosen to allow for sufficiently low pressure by large pumping diameters along the drift tube to minimize energy shifts by inelastic collisions with residual gas. Compared to the 1.2-m length for optical pumping within the drift tube, the short distance of a few cm in the fringe field where the ions can already interact with the laser beam within three times the linewidth can be safely neglected.

3.5 Post-acceleration stage

The acceleration with the high-voltage of interest takes place in the post-acceleration section which is placed between both interaction regions. Since the high voltages are in the kV regime and can easily exceed the initial acceleration voltage, this post-acceleration will strongly affect the ion trajectory. A displacement of the ion beam due to an inclined electrical field can be avoided, when the electrodes have a proper shape and are well aligned with respect to the central axis. But even then, the strong electric field will influence the ion beam since the acceleration with the high voltage will lead to a strong focus and hence, to a non-collimated ion beam causing a systematic shift in the high-voltage measurement.

To preserve the collimation, two einzel lenses can be used as an ion-optical telescope. Placing one einzel lens in front and one behind the acceleration gap and choosing the right potentials, a 1 : 1 projection of the ion beam can be achieved as shown in a simulation in Fig. 3.10. Each of the einzel lenses consists of three electrodes whereof the central one can be floated with a variable voltage. The outer electrodes

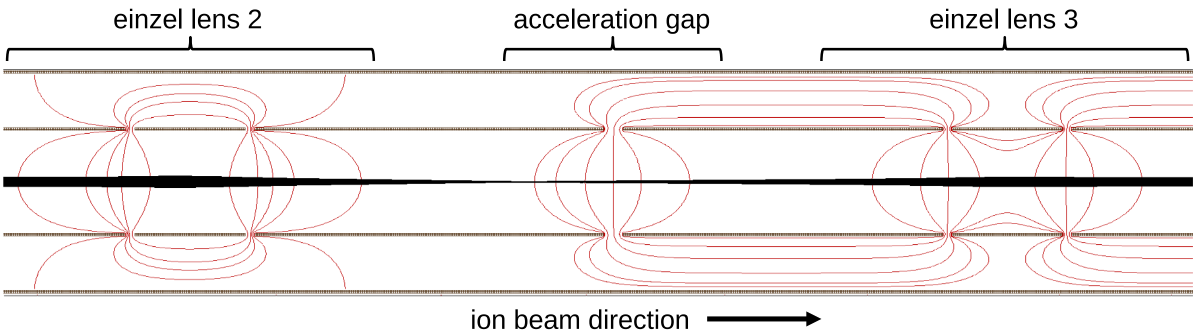

Figure 3.10: Ion-optical telescope to preserve the collimation of the ion beam while accelerating it with the high-voltage of interest. The voltages applied to the einzel lenses in front and behind the acceleration gap have to be adapted for each specific acceleration potential.

of the first lens are on the potential of the pumping region whereas those of the second lens are floated with the high-voltage of interest increased by a small offset voltage $U_{\mathrm{electr.}} = U_{\mathrm{HV}} + 24\,\mathrm{V}$ delivered by batteries. Therefore, the main acceleration takes place between the einzel lenses but laser interactions with the ions in the probe state can be avoided before they enter the second interaction region. Only there, they will experience the full acceleration potential and are probed optically. The voltages applied to the einzel lenses have to be adapted individually for each acceleration voltage to ensure a collimated ion beam for the specific acceleration voltage.

3.6 Probing and optical detection (IR2)

The second interaction region is floated with the high-voltage of interest and is equipped with an optical-detection unit to observe the fluorescence signal while a laser scan or Doppler tuning is applied. Since the potential difference relative to the last drift tube is small (24 V), the ions experience only a small acceleration when entering which causes a negligible focusing of the ion beam.

To achieve a reasonable fluorescence signal, a large solid angle has to be covered while the stray light should be suppressed in order to increase the signal-to-noise ratio. Achieving both is experimentally challenging: At the ALIVE setup this is realized by two elliptical mirror sets, each equipped with a compound parabolic concentrator (CPC) and a photo multiplier tube (PMT) as depicted in Fig. 3.11. Placing one focal point of the elliptical mirrors along the ion-beam axis, the emitted fluorescence light will be guided through a viewport to the other focal point of the ellipse being placed outside the vacuum chamber where a movable slit aperture is located. On top of it the CPC is installed. The fluorescence light which enters the CPC under small entrance angles is transported to the PMT[2] which has a small opening diameter (22 mm). On the contrary, stray light which is entering under larger angles will be reflected back leading to an efficient background suppression. The PMT simply counts the number of the impinging photons. Here, a photo-cathode material is chosen with a work function $> 2\,\mathrm{eV}$ to suppress background from solar radiation. More details can be found in [79] and in [80].

Since at least two reflections are necessary to guide a fluorescence photon to the PMT in most cases, highly reflective mirrors are required. Furthermore, broad band mirrors are desirable to offer multi-purpose applications of the experimental setup. Especially the deep-UV transition of In^+ has to be covered and hence, aluminum was chosen since its plasma edge and the corresponding drop in reflectivity is far below 200 nm in contrast to other common materials like silver, copper or gold. The reflectance of a perfect aluminum surface is of about 90 % from the ultraviolet to the infrared regime [81]. However, due to its special shape, no commercial mirror system was available. A high-reflectivity coating on the machined surface produced in the mechanical workshop was also not feasible, neither the

---

[2] Sens-Tech Ltd, P25PC UV glass

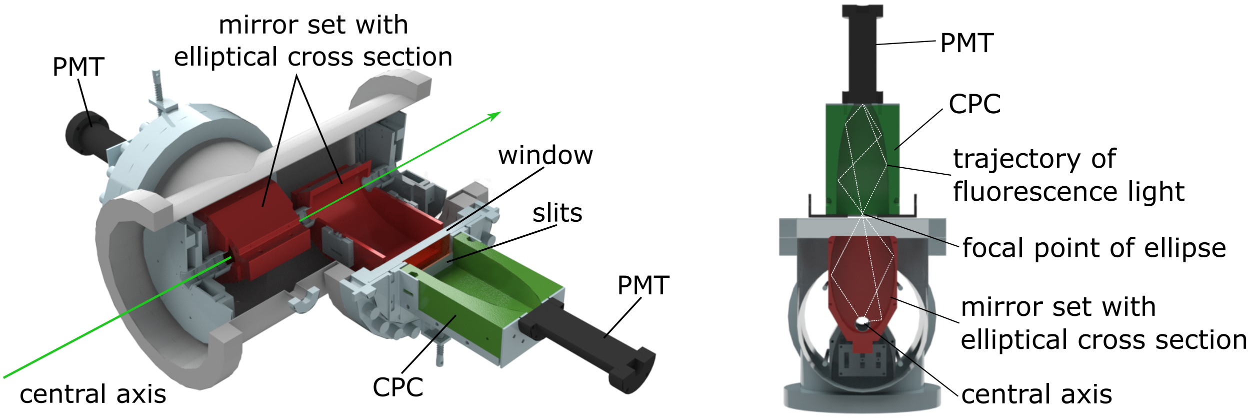

Figure 3.11: Second interaction region equipped with two optical-detection units, each consisting of an elliptical mirror set (red), a compound parabolic concentrator (CPC) (green) and a photo multiplier tube (PMT) (black). The in-vacuum parts are floated on the high-voltage of interest. To avoid field penetrations, a metallic grid is placed between the elliptical mirrors and the CPCs. Since all mirrors are made of polished aluminum, photons from the ultraviolet to the infrared regime are guided to the PMT allowing a universal usage of the optical-detection region.

attachment of thin, high reflective foils. Hence, the machined surface was polished by hand. A reflectivity of 70 % - 80 % in the UV regime could be achieved which nearly reaches the limit of 90 % of an ideal aluminum mirror. Since the polished aluminum surface can lose its high reflectivity in the UV regime through oxidation, the mirrors of the CPC which are outside the vacuum, have been coated with quartz glass.

Despite these challenges, the optical-detection unit performs very well yielding a high signal-to-noise ratio. Another characteristic number is the amount of ions needed to produce one detected fluorescence photon. In the current setup, only 60 Ca^+ ions are needed for one count per PMT in case of a 1 mW laser beam at 393 nm [79] which is an outstanding result compared to other setups. In case of In^+, $3 \cdot 10^5$ ions are needed for a 1 mW laser beam at 231 nm to generate one fluorescence count. The lower rate is mainly due to the much smaller Einstein coefficient for stimulated absorption B_{12} which is nearly three orders of magnitude smaller compared to Ca^+:

$$B_{12} = A_{21}\frac{\lambda^3}{8\pi h} \Longrightarrow \frac{B_{12}(\mathrm{In}^+)}{B_{12}(\mathrm{Ca}^+)} = \frac{2.1 \cdot 10^6\,\mathrm{s}^{-1}}{1.47 \cdot 10^8\,\mathrm{s}^{-1}} \frac{(231\,\mathrm{nm})^3}{(393\,\mathrm{nm})^3} = 0.003 \tag{3.2}$$

where A_{21} is the Einstein coefficient for spontaneous emission. Furthermore, the reflectivity of the UV light is worse than that of visible light and the quantum efficiency of the PMT drops from 27 % to 13 %. Even the amount of photons in a laser beam with similar power is reduced by a factor 1.7 which explains the huge difference in the observed fluorescence rate. But since larger currents of In^+ ions are available, this can be partially compensated.

3.7 Laser systems

To perform high-precision collinear laser spectroscopy, stable laser systems with a narrow spectral width are required. Depending on the application, also fast frequency changes have to be realized, setting high demands on the laser system.

Since the transition wavelength of measurements on Ca^+ with 393 nm and 854 nm differ drastically from the transition wavelength of In^+ at 231 nm, different laser systems have to be used and will be discussed separately. Furthermore, the stabilization scheme and the measurement of the laser frequencies will be introduced.

3.7.1 Setup for Ca^+ measurements

For performing pump-and-probe experiments in the Λ-system of Ca^+ two different laser systems are required. The optical pumping will take place at 393 nm whereas an 854-nm laser has to be employed for probing. As discussed before, the pump laser can be fixed to one frequency whereas the probe laser has to be flexible due to the different Doppler shifts caused by the different post-acceleration voltages.

For optical pumping a diode laser system has been chosen. An external cavity diode laser (ECDL) with a laser diode producing light between 780 nm and 787 nm was already available [82] and hence, the D2-transition was selected for optical pumping (see section 2.3.1). As shown in Fig. 3.12, the laser frequency can be measured and controlled with a WSU10 wavelength meter (wavemeter) from High Finesse. To generate laser light at 393 nm, the light from the ECDL is amplified and frequency doubled. The amplification is realized with a tapered amplifier TEC-400-780-2500 from Sacher Lasertechnik and the second harmonic generation (SHG) with a commercial Wavetrain system from Spectra Physics based on a lithium triborate (LBO) crystal. The SHG light possesses several side fringes due to the production process in the crystal [83], which would increase the laser-induced stray light. Therefore, the 393 nm light is sent through a mode cleaner (spatial filter) consisting of two lenses and a pinhole to guarantee a perfect Gaussian beam before guiding it directly to the beamline. For background-free laser spectroscopic experiments, an acousto-optical modulator (AOM) is placed before the beamline which offers the opportunity to block the laser for optical pumping while the ions are probed with the infrared laser [84]. But due to the already low background rates, its benefits are compensated by the longer measurement cycle and hence, the measurements described in chapter 4 were done with continuous beams. The total setup is explained in more detail in [85].

For the probing transition at 854 nm the more flexible titanium:sapphire (Ti:Sa) laser Matisse 2 TS from Sirah Lasertechnik pumped by a 20-W Millennia eV from Spectra Physics is used. The continuous-wave ring laser with several frequency-selective elements allows the production of laser light between 680 nm and 1015 nm without changing the trajectory of the ejected beam. Hence, this setup allows fast frequency changes and fulfills the requirements for driving the probing transition. A stable reference cell which controls the laser frequency with a side-of-fringe stabilization offers a narrow spectral width and a high stability. To avoid long-term drifts, the reference cell is compared to a WSU30 wavemeter from High Finesse.

This Ti:Sa laser can generate laser powers of several W and runs most stable in this condition. But since less than 1 mW is required for the experiment to avoid power broadening, only a small fraction of the generated light is separated and sent to the beamline through a single-mode fiber. In front of its entrance window the laser beams are superimposed by a dichroic mirror.

Since both lasers are stabilized directly or indirectly to wavemeters, their performance defines the laser stability and spectral width. Despite the high relative accuracy of wavemeters, external changes in temperature and pressure will induce drifts which are transferred to the laser frequency. Therefore, the wavemeters are calibrated in short intervals (1 min) by a frequency-stabilized (two-mode locking) helium-neon laser[3] (HeNe). However, this stabilization has a certain control range causing a spectral width of about 400 kHz for the probe laser and of 550 kHz for the pump laser. The spectral width of the laser for optical pumping is larger since it is increased during SHG by a factor $\sqrt{2}$ [62]. But still, the spectral width is much smaller than the natural linewidth of 23.4 MHz and will not have an impact on the lineshape.

The polarization of both laser systems is defined by the Matisse and the Wavetrain because both produce linearly-polarized light. Since the probe laser is directly sent to the beamline no fluctuations in the polarization are expected. The light of the probe laser which is guided through an optical fiber to the beamline, could experience polarization changes in the fiber. To exclude systematic shifts caused by the Zeeman effect, this was measured and no polarization fluctuations were observed even in long-term measurements.

---

[3] SIOS Meßtechnik GmbH, He-Ne-Laser SL 03, fiber coupled

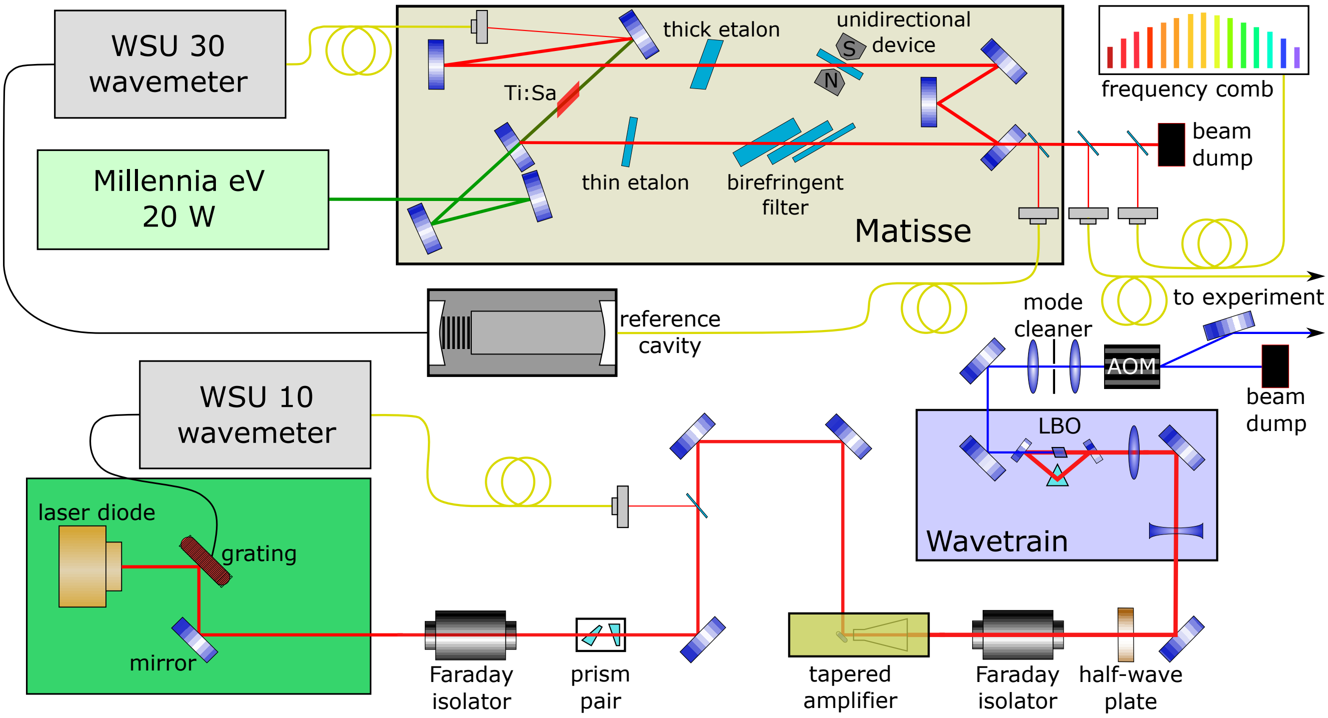

Figure 3.12: Setup of the laser system for Ca^+ measurements. A diode-laser-based system with tapered amplifier and frequency doubler with a lithium triborate (LBO) crystal is used to generate light at 393 nm for optical pumping (lower part). This laser can be blocked with an acousto-optical modulator (AOM). The 854-nm laser light for probing is produced by a titanium:sapphire (Ti:Sa) laser pumped by a Nd:YAG laser (upper part). Both systems are stabilized by wavemeters. The laser for probing can be measured additionally with a frequency comb. See text and [85] for more details.

3.7.2 Setup for In^+ measurements

The $5s^2\ {}^1S_0 \rightarrow 5s5p\ {}^3P_1$ transition of In^+ which is to be used for pumping and probing through a manipulation of the magnetic substate population, has a rest-frame transition frequency of about 231 nm. A direct production of this deep-UV light is not possible and hence, the fourth harmonic from Ti:Sa-generated laser light will be used to excite the ions conserving the flexibility of the Ti:Sa. The fourth harmonic generation (FHG) is realized with two Wavetrains installed behind a Matisse as shown in Fig. 3.13. During this process the spectral width is increased by a factor $\sqrt{2}^2 = 2$ compared to the fundamental Ti:Sa light [62] which would lead to a spectral width of 800 kHz if again the wavemeter stabilization would be used as discussed in the previous section. Since the natural linewidth is much smaller (360 kHz) this is not desired. The manufacturer of the Matisse specifies that a spectral width of less than 50 kHz is achievable with the available reference cell [86]. However, its regulation with the wavemeter which is very sensitive to temperature and pressure fluctuations, induces noise on the reference cell and increases the spectral width. On the other hand, it ensures a high long-term stability which would not be possible without this stabilization. By using the frequency comb to stabilize the reference cell instead and by decreasing the amplification factor of the reference cell piezo to the minimum, the spectral width of the Matisse could be reduced to about 100 kHz [60, 87] corresponding to 200 kHz after the FHG which is clearly below the natural linewidth. Another advantage of this regulation scheme is that the laser frequency is directly stabilized to the absolute reference and hence, can be identified very accurately. Behind the second Wavetrain a mode cleaner is installed to create a pure Gaussian beam profile and remove higher Bessel contributions from the beam shape. If the measurements are performed in

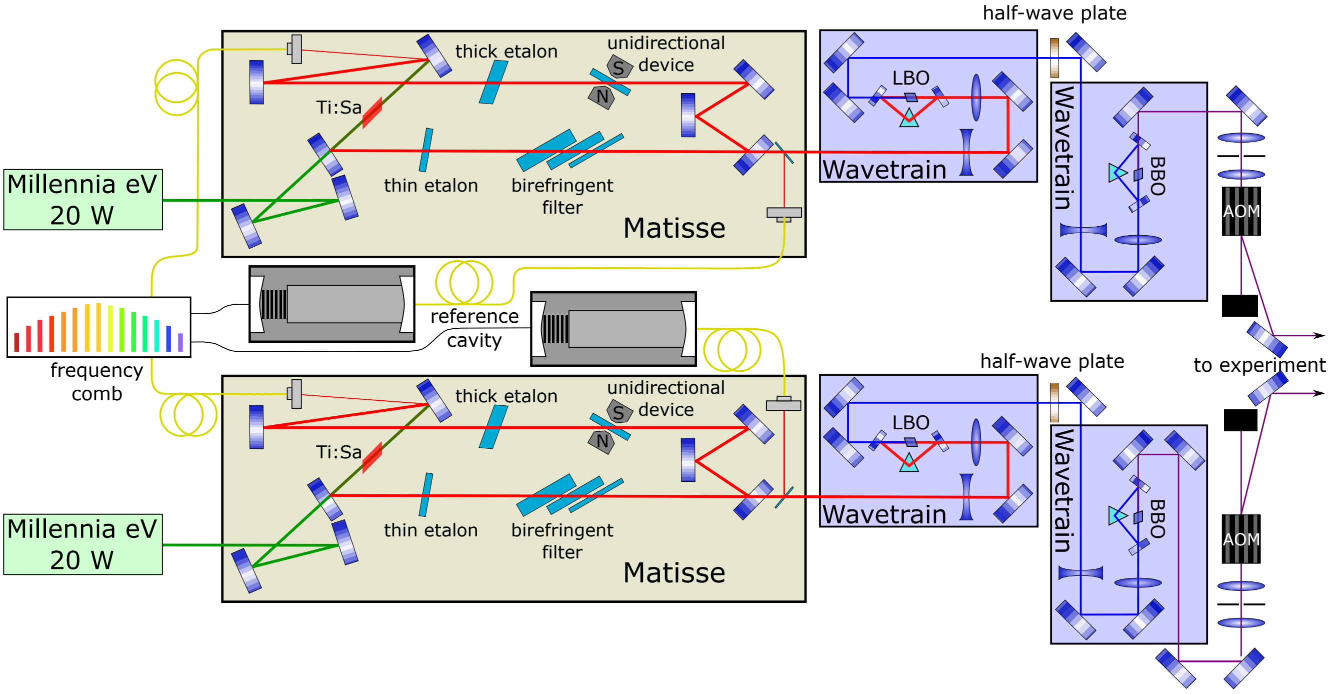

Figure 3.13: Setup of the laser system for In^+ measurements. Two Ti:Sa lasers pumped by Nd:YAG lasers, produce a 923-nm laser beam with a power of up to 3.5 W. Both lasers are stabilized on the frequency comb. Second harmonic generation with a lithium triborate (LBO) crystal in the first stage and a barium borate (BBO) crystal in the second stage produces 100 mW of the 231-nm light for optical pumping and probing. The lasers can be blocked with acousto-optical modulators (AOM) for background-free measurements. See text for more details.

a pulsed mode, the laser for optical pumping can be blocked with an AOM during the probing to reduce the laser-induced stray light. Due to the long lifetime of the excited state, it is even possible to block the probe laser while detecting the fluorescence photons if a probing tube is inserted before the optical-detection region yielding a background-free optical detection. The laser beams can be superimposed with a beam splitter plate before they are directly sent to the beamline.
The complete setup was only available for two month in summer 2018 when one Wavetrain from the COLLAPS experiment at ISOLDE/CERN was installed in Darmstadt to demonstrate efficient FHG needed for a laser-spectroscopic online experiment on exotic Sb isotopes.

3.7.3 Measurement of laser frequencies

For a flexible frequency measurement with a relative uncertainty better than 10^{-10} which is necessary for a high-voltage evaluation in the ppm regime, a frequency comb is used. Its mode-locked femtosecond laser generates a series of equidistant frequencies with the distance f_{rep} in the visible and infrared spectrum. Superimposing this light with a cw laser, a beat frequency f_{beat} in the MHz regime can be detected with a photo diode. The mode number N of the frequency-comb mode closest to the cw laser frequency can be determined through changing the repetition rate or faster, through estimating it from a wavemeter measurement

$$N \approx \frac{c}{\lambda_{\mathrm{wavemeter}}} \frac{1}{f_{\mathrm{rep}}} \tag{3.3}$$

which has to be rounded to the next integer. The accurate frequency f_{cw} of the cw laser can then be calculated as:

$$f_{\mathrm{cw}} = N \cdot f_{\mathrm{rep}} \pm f_{\mathrm{beat}} \pm 2 f_0 \, . \tag{3.4}$$

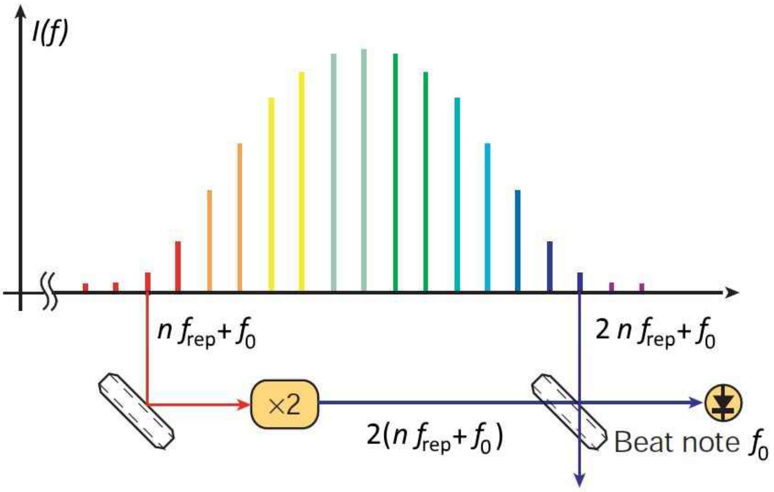

Figure 3.14: Frequency spectrum of a frequency comb generated by a mode-locked femtosecond laser. Several modes in the frequency distance f_rep are emitted in the visible and infrared regime. The carrier envelope offset frequency f_0 is determined by comparing the frequency doubled mode n with the mode $2n$ of a higher octave and is stabilized to the frequency $f_0 = 20\,\text{MHz}$. Superimposing the comb light with a cw laser, the beat frequency f_beat with the nearest mode N can be observed and allows to calculate the cw laser frequency with sub-Hertz accuracy [32] provided that the linewidth of the laser is sufficiently small.

The carrier envelope offset frequency f_0 can be identified through the comparison of a frequency-doubled mode n from the red wing with the mode $2n$ of the higher optical octave (compare Fig. 3.14) and is usually stabilized to $f_0 = 20\,\text{MHz}$. Since our application is in the near-infrared regime, the frequency-comb is frequency doubled and this offset frequency has to be considered twice. Depending on the position of the cw laser frequency relative to the closest comb mode, the signs of f_beat and f_0 vary and hence, have to be determined for each measurement. Since frequency combs can achieve sub-Hertz accuracies, the limit of the frequency determination is given by the stability of the cw-laser frequency which was discussed in the previous chapters.

During the high-voltage measurements with Ca^+ ions, the laser frequency of the probe laser was measured before and after each voltage measurement which only took some minutes. A simultaneous measurement was not possible with the current data acquisition system. The mean of both data sets obtained from the comb was taken for the laser frequency. It should be noted that the absolute frequency of the pump laser is not required in the reference-measurement approach as long as it is stable and hence, it was not measured with the comb. Instead, it was stabilized by the wavemeter which was frequently calibrated with a frequency-stabilized HeNe laser. Due to the regular harmonic fluctuations of the HeNe of about 1 MHz, several measurements have to be performed to reduce the uncertainty.

In high-voltage measurements with In^+ ions pumping and probing frequency are very close. This opens the opportunity for a simultaneous measurement of both frequencies with the frequency comb. Developments in the stabilization scheme of the Matisse allowed to stabilize the reference cell on the beat frequency which significantly improved the stability of the Matisse laser (see section 5.1.2).

3.8 Conventional high-voltage evaluation

For a comparison with the standard method of high-voltage determinations, the high-voltage of interest is measured in parallel to the laser-based approach with a conventional setup. The high voltage is broken down into the regime of some Volts with the HVA100 high-precision high-voltage divider from Julie Research. This voltage can then be read out using the 8.5-digit multimeter Keysight 3458A which is regularly calibrated to a Fluke 732B direct voltage standard. The divider was originally specified to the 10^{-4} level but after more than 30 years of aging, the resistors show only a small residual drift and a higher accuracy can be achieved if the high-voltage divider is well calibrated.

For an accurate determination of the divider ratio, the latest calibration of the HVA100 was performed in 2017 at PTB[4]. For high voltages up to 40 kV the divider showed a nearly constant divider ratio of 10000.085 ± 0.005 for positive and of 10000.031 ± 0.005 for negative voltages at a room temperature of 20 °C as shown in Fig. 3.15. Here, the uncertainties represent only the statistical deviations which are in the sub-ppm regime and demonstrate the high short-term stability of the divider. Furthermore, no significant running-in characteristics have been observed for these voltages. Also the long-term stability of the divider ratio is very satisfying since the calibration factor did not change since its last calibration in 2013 in Münster where it was compared to the KATRIN high-precision divider [13].

When applying higher voltages, the heat load is increased and the rising temperature of the resistors causes a smaller divider ratio. Hence, voltage-dependent divider ratios have to be applied for voltages above 40 kV leading to larger systematic uncertainties. Generally, the HVA100 shows a high temperature dependence. This was also investigated at PTB and showed a deviation of −2.75 ppm/K. Room temperature changes caused by the insufficiency of the air condition in the calibration hall caused drifts of several ppm, leading together with the imprecisely known temperature at the HVA100 to an absolute uncertainty of 5 ppm.

Since external temperature changes have by far the largest impact on the accuracy of the divider, a temperature controlled chamber for the HVA100 was designed. Here, the temperature fluctuations can be reduced to 0.01 K which leads to a significant increase of the relative precision. However, the absolute accuracy stays at the 5-ppm level without a new calibration of the HVA100 inside the temperature controlled chamber. The high precision is indispensable for the measurements: Since Doppler tuning is applied, high-voltage-divider-based measurements can only be realized before and after the laser-based measurement. But due to the high precision of the divider and the high stability of the Heinzinger PNChp 20000-10neg high-voltage power supply (see section 4.1.2) this does not give rise to significant systematic deviations and, hence, justifies the comparison of both methods.

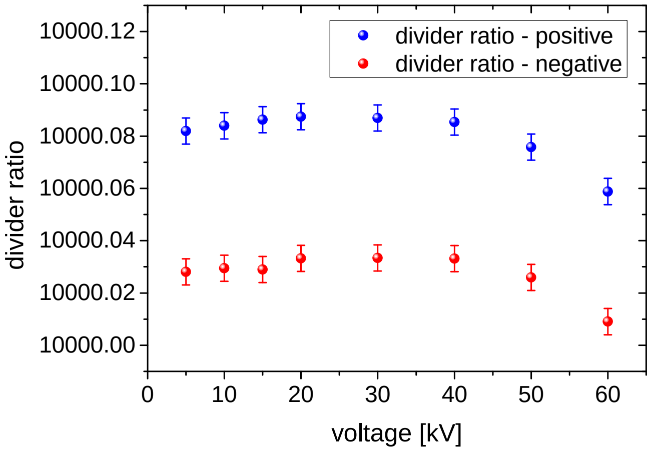

Figure 3.15: Calibration of the HVA100 high-voltage divider at PTB. For voltages up to 40 kV the divider ratio is nearly constant and could be specified to 10000.085 for positive and to 10000.031 for negative voltages at a room temperature of 20 °C with a statistical uncertainty of 0.5 ppm. For higher voltages the divider ratio changes significantly due to the larger heat load deposited in the resistors. These show a high temperature dependence of −2.75 ppm/K which is the main reason for the larger systematic uncertainty of 5 ppm.

---

[4] Physikalisch-Technische Bundesanstalt, German metrology institute

4 High-voltage determination with Ca^+ ions

For the commissioning of the experimental setup and for first laser-based high-voltage measurements Ca^+ ions have been chosen. Since this ion species was employed before to perform laser-based high-voltage measurements [19, 22], it opens the opportunity to compare the performance of our apparatus with precursor experiments. There, the high-voltage measurements were limited to uncertainties of about 100 ppm but due to the improvements in the experimental setup and in the measurement procedure described before, a higher accuracy is expected. To quantify the achieved accuracy, the laser-based high-voltage measurements are compared to measurements with a conventional 5-ppm system for high-voltage measurements based on the HVA100 voltage divider described in section 3.8. An additional 5-ppm high-voltage divider was provided by PTB Braunschweig for the measurement campaign.

4.1 Commissioning of the experimental setup

The experimental setup described in the previous chapter was assembled within this work. In a dedicated commissioning phase possible sources for uncertainties have been identified and were minimized as far as possible. The remaining contributions are quantified in this section.

4.1.1 Alignment optimization

A proper superposition of laser and ion beam is crucial since any angular misalignment will lead to a systematic deviation to smaller absolute voltages as discussed in section 2.2.5. Therefore, ion and laser beams have to be precisely adjusted to the central axis. For the laser beams, this can be realized with an uncertainty of less than 0.1 mm when sending the laser beams through the iris diaphragms of the diagnostic stations which are 2.6 m apart, while monitoring the beam shapes on the phosphor screens with the camera. On the contrary, the collimated ion beam emitted by the surface ionization source has a beam diameter of about 5 mm which limits the adjustment accuracy to 1 mm at each diaphragm leading to an uncertainty in the angular alignment of $\alpha_\mathrm{s} = 0.8\,\mathrm{mrad}$. Furthermore, the deflection by the earth magnetic field yields an additional uncertainty of $\alpha_\mathrm{B} = 0.6\,\mathrm{mrad}$.
The importance of an exact alignment also of the ion optical elements became clear after first test measurements when deviations as large as 100 ppm were observed [85]. It turned out that particularly the electrode adjustment at the acceleration gap is crucial. A misalignment of a few mm resulted in an angular deviation of 12 mrad after the acceleration which caused the large systematic offset.
The alignment of all ion optical components was improved to be better than 1 mm. In ion beam simulations its impact on the ion beam trajectory was calculated and is stated in Tab. 4.1. It turned out that, e.g., a post-acceleration by 19 kV can cause a deflection of up to $\alpha_\mathrm{i} = 1.3\,\mathrm{mrad}$. Adding the angular deviations due to the ion beam diameter and the earth magnetic field quadratically yields a total angular misalignment of up to $\alpha_\mathrm{tot} = 1.64\,\mathrm{mrad}$ which would correspond to an uncertainty of 4.7 ppm in the high-voltage evaluation. For smaller post-acceleration voltages the deflection due to ion optical elements is smaller and nearly vanishes in the reference measurement since only small voltages are applied in this case. However, angular deviations caused by the ion beam diameter and the earth magnetic field also occur in this case. Therefore, these will partially cancel in the reference-measurement approach. The reduced systematic uncertainties are stated for −5 kV, −10 kV, −15 kV and −19 kV in Tab. 4.1.

Table 4.1: Simulated systematic uncertainties of the laser-based high-voltage evaluation due to misaligned electrodes in the post-acceleration section. For a misalignment of 1 mm the ion beam is deflected by α_i relative to the laser beam. Adding the possible angular deviations due to the ion beam diameter ($\alpha_\mathrm{s} = 0.8$ mrad) and the earth magnetic field ($\alpha_\mathrm{B} = 0.6$ mrad) leads to the total uncertainty of the alignment α_tot which can cause systematic shifts of the laser-based high-voltage evaluation to smaller absolute voltages. Its impact is calculated for the applied reference-measurement approach where the contributions α_s and α_B partially cancel.

	-5 kV	-10 kV	-15 kV	-19 kV
α_i	0.2 mrad	0.5 mrad	1.0 mrad	1.3 mrad
α_tot	1.0 mrad	1.1 mrad	1.4 mrad	1.6 mrad
δU_angle	5.7 mV	16 mV	44 mV	74 mV
$\delta U_\mathrm{angle}/U_\mathrm{HV}$	1.1 ppm	1.6 ppm	2.9 ppm	3.9 ppm

4.1.2 High-voltage stability

As discussed in section 2.2.14, the high-voltage of interest and the voltage applied to the first interaction region have to fulfill high demands on their stability. In Fig. 4.1 a schematic circuit diagram of these voltages is depicted. The high voltage of interest U_HV provided by the Heinzinger PNChp 20000-10neg is floated on the scan voltage U_scan generated by the Kepco BOP500M high-voltage amplifier. It is also measured with a conventional setup for high-voltage measurements consisting of an 8.5-digit multimeter Keysight 3458A combined with the HVA100 high-voltage divider introduced in section 3.8 as a reference for the laser-based approach. However, a simultaneous measurement of U_HV with both methods is not possible if Doppler tuning is applied and fast voltage scans are performed. Hence, the conventional measurement is realized before and after a laser-based measurement. To avoid systematic deviations, the high-voltage of interest has to be stable over this period of time which typically covers several minutes. Measuring its stability electronically over several hours for a typical voltage of -10 kV yielded drifts of less than 40 mV during the total period as shown in red in Fig. 4.2. During a measurement cycle of several minutes the drifts are < 10 mV which would correspond to 1 ppm.
The voltage U_pump generated with an ISEG EBS 8030 high-voltage power supply showed a long-term stability better than 10 mV (compare Fig. 4.1 blue). Its drift is identified by regularly performing laser-based reference measurements without applied high-voltage. Here an interval of one hour is typical. Again, this corresponds to an uncertainty of 1 ppm but since these deviations are statistically distributed they can be reduced by taking several measurements. The remaining contribution is covered within the statistical uncertainty of the high-voltage evaluation.
The ion source is floated on the starting potential U_start by a Heinzinger PNChp 20000-10pos power supply which offers a similar high stability as its negative counterpart. An additional power supply Delta Elektronica SM 15-100 is placed on a high-voltage platform for furnace heating and fluctuates by 50 mV in a timescale of several minutes due to spontaneous changes in resistance. In the pump-and-probe approaches, this does not affect the high-voltage measurement directly but points out the disadvantages of the one-chamber approach which depends on the stability of the voltage applied to the ion source.
Besides the voltage stability also the linearity of the scan voltage U_scan has been investigated. It is generated by a 18-bit digital-to-analog converter (DAC) and amplified with a Kepco BOP500M high-voltage amplifier for performing Doppler tuning. The system achieves a very high linearity (see appendix B) with an amplification factor of about 50.5 and a small offset of a few 10 mV. By using similar scan voltages in the reference and the high-voltage measurement ($U_{\mathrm{scan}_\mathrm{ref}} - U_\mathrm{scan} < 20$ V) the systematic uncertainty can be limited to $\delta U_\mathrm{scan} < 0.2$ mV. To allow fast changes between high-voltage and reference measurements

Table 4.2: Stability of relevant high-voltage power supplies during usual measurement times. For a typical value of −100 V the voltage U_{pump} applied to the first interaction region showed a stability of 10 mV. A similar stability is achieved for the high-voltage of interest U_{HV} applied to the second interaction chamber during an interval of several minutes as depicted in Fig. 4.2. The broadening caused by noise of the high voltages is much smaller than the natural linewidth of 23.4 MHz.

	drift	resulting uncertainty	noise	broadening
U_{pump}	10 mV	1 ppm	15 mV	350 kHz
U_{HV}	10 mV	1 ppm	20 mV	140 kHz

a high-voltage switch[1] which accepts a software trigger, was built to apply either $U_{\mathrm{HV}} + U_{\mathrm{scan}}$ or U_{scan} only.

Besides the stability also the noise on the high voltages was measured. It increases the width of the optically-pumped velocity class and therefore causes a broadening of the transition linewidth. At IR2, a 20 mV$_{\mathrm{pp}}$ jitter is induced by the Heinzinger and the Kepco power supplies whereas the noise at IR1 is smaller than 15 mV$_{\mathrm{pp}}$. This leads to a total broadening of 140 kHz and 350 kHz, respectively, due to different differential voltage sensitivity κ, which is much smaller than the natural linewidth of the transition. All values and their consequences are summarized in Tab. 4.2.

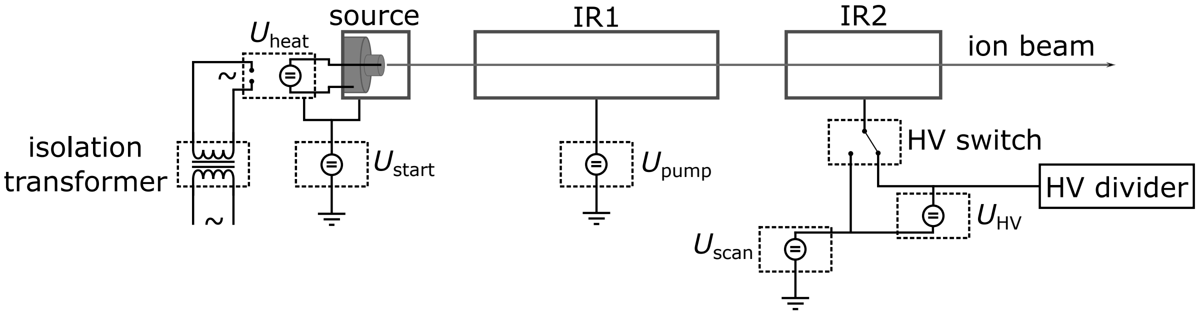

Figure 4.1: Relevant power supplies for the high-voltage evaluation. The ion source and a high-voltage platform with the power supply for heating the furnace are floated by a Heinzinger PNChp 20000-10pos power supply on typically +14 kV. The voltage $U_{\mathrm{pump}} \approx -100$ V is applied with an ISEG EBS 8030 high-voltage power supply to the first interaction region. The high-voltage of interest generated by a Heinzinger PNChp 20000-10neg is applied to the second interaction region and measured in parallel with a conventional system based on the HVA100 high-voltage divider (see section 3.8). For performing Doppler tuning it is floated on the scan voltage U_{scan} provided by a Kepco BOP500M high-voltage amplifier. A high-voltage switch enables fast changes between high-voltage ($U_{\mathrm{HV}} + U_{\mathrm{scan}}$) and reference measurements (U_{scan} only).

4.1.3 Laser stability

The stability of the laser frequency is directly linked to the statistical uncertainty of the high-voltage measurements. Especially frequency fluctuations of the laser for optical pumping which is not measured in parallel with the frequency comb, will affect the measurement.

Since both laser systems are controlled by a wavemeter, its stability is transferred to the laser systems as

---

[1] Switch is based on a GIGAVAC G25WF relay.

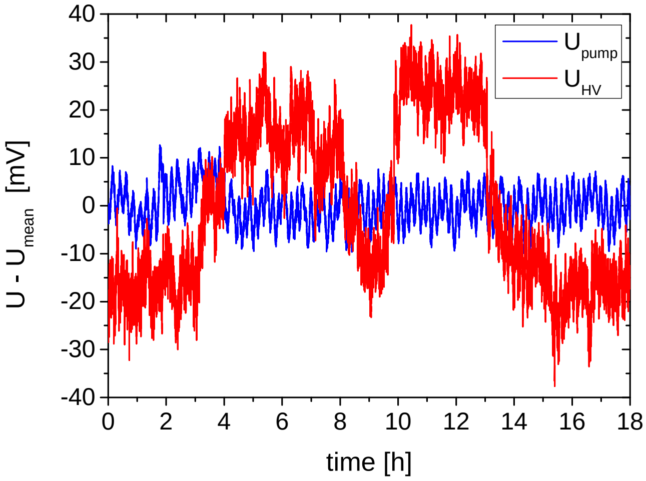

Figure 4.2: Long-term stability of high-voltage sources used for floating IR1 on $U_{\text{pump}} = -100\,\text{V}$ (blue) and IR2 on $U_{\text{HV}} = -10\,\text{kV}$ (red). Required is a high stability in an interval of several minutes for U_{HV} and of about one hour for U_{pump}. In these intervals drifts of less than 10 mV are usually observed.

is its sensitivity to external temperature and pressure changes. Pressure changes usually lead to drifts on a very long time scale whereas temperature fluctuations occur in the interval of some minutes due to the air conditioning system. The long-term drifts can be easily avoided with a regular calibration of the wavemeter on a stabilized HeNe, whereas short-term fluctuations of about 2 MHz were observed even for one calibration per minute.

To reduce the temperature drift, the wavemeters have been installed in cardboard boxes to decouple them from fast temperature changes in the laboratory. This increased the stability by a factor of two. Nevertheless, changes of up to 1 MHz are still observed when calibrating the wavemeter on the HeNe which corresponds to a 50-mV shift in the high-voltage measurement. These fluctuations are statistically distributed and the resulting uncertainty can be reduced by an increased measurement time. By averaging over a series of measurements the uncertainty contribution due to the laser stability is reduced below 10 mV which is discussed later on in section 4.3.3 and 4.3.4.

A higher stability of the laser systems can be achieved with either a more stable calibration laser and an improved temperature stabilization of the wavemeter or by stabilizing the reference cavity of the laser system directly with a stable reference laser as demonstrated in [60]. In this case the wavemeter is not needed and the stability of the laser system is solely defined by the reference laser and the stabilization feedback loop. Alternatively the laser systems can be stabilized on the frequency comb which was discussed in section 3.7.2 and will be applied for the measurements on In$^+$.

Besides the frequency stability, fluctuations of the laser power can contribute to the uncertainty of laser spectroscopic measurements: The laser generates stray light in the beamline and increases the background rate of the photomultiplier. This modulated background level affects the resulting lineshape and increases the uncertainty of the determination of the transition frequency. Such power fluctuations were observed when using a fiber to guide the 393-nm light for optical pumping to the beamline and were eliminated by a direct transport through air.

4.1.4 Background reduction

In ALIVE as well as in classical collinear laser spectroscopy, the resonance is observed optically. Hence, stray light reaching the photomultiplier has to be avoided to achieve a good signal-to-noise ratio. External light can be shielded very efficiently [79] whereas the reduction of laser-induced stray light of the same wavelength as the fluorescence light is challenging. In the optical pumping scheme of Ca$^+$ it is possible to use PMTs which do not detect the 854-nm light. Therefore, the stray light is generated only by the 393-nm laser for optical pumping.

Even though the design of the optical-detection region (compare section 3.6) is optimized to suppress the transport of scattered light to the photomultipliers, it cannot be completely avoided. The laser-induced stray light mainly originates from scattering at apertures along the beamline and will undergo multiple reflections along the beamline with its blank and shiny surfaces until a small fraction of it will eventually reach the PMTs. Creation of stray light can be minimized by the optimization of the laser beam profile. A well-collimated Gaussian laser beam is shaped and the side fringes generated in the SHG process are cut off by a spatial filter (see section 3.7.1) and sent to the beamline. By this, the background was reduced from 20 MHz to less than 1 MHz for a laser power of 100 μW.

The plane and uncoated entrance and exit windows of the beamline were identified as another source for the still high background rates. These windows have been chosen to provide flexibility in the wavelength of the laser light and to avoid changes of its polarization. But partial reflections at the surfaces cause additional stray light inside the beamline which was reduced by mounting an array of three diaphragms at the vacuum sides of the windows. The central laser beam can pass these diaphragms undisturbed whereas light scattered at the windows which is not on axis, is cut off. Together with the two adjustable iris diaphragms at the diagnostic stations, the background rate was finally reduced to an acceptable level of only some 100 kHz for a laser power of 1 mW.

Background reduction by restricting the reflectivity of the surfaces by painting them black was tried in the test experiment at TRIGA-Laser [51] and was found to be inappropriate due to changes of the surface resistance with time and accompanying changes of the contact potentials.

4.1.5 Resolution optimization of the pre-accelerated beam

The multi-purpose beamline used for the ALIVE experiment is designed for several laser spectroscopic applications. When experiments without pump-and-probe schemes are performed (see [35, 60] for the absolute frequency determination of stable Ba^+ isotopes), a narrow initial velocity distribution is crucial to avoid large Doppler broadening. But even in pump-and-probe experiments where a new velocity class is defined in the optical pumping process, it is important to know the underlying, initial distribution.

Besides the thermal energy distribution (about 0.3 eV for typical operation conditions of the ion source introduced in section 3.1) fast fluctuations of the starting potential cause an energy spread. These potential fluctuations are composed of contributions of the high-voltage power supply generating U_{start} which was measured to be 20 mV and of the power supply for heating the furnace. The latter is placed on a high-voltage platform floated on the potential U_{start} and supplied with energy by an isolation transformer (see Fig. 4.1). Measuring its voltage relative to the ground potential of the beamline yielded a 10-V_{pp} ripple at 50 Hz. Tracing down the cause, the isolation transformer could be identified. Optimizations lead to a reduction by a factor two but the breakthrough was achieved with a new transformer[2] with additional shield windings. The noise on the starting voltage could be reduced below the measurement threshold and allowed to perform laser spectroscopic measurements on Ba^+ at a level of its natural linewidth.

4.2 Optical pumping for resonant population transfer

In the high-voltage measurement procedure that is established in this chapter, the $4s\,^2\mathrm{S}_{1/2} \rightarrow 4p\,^2\mathrm{P}_{3/2}$ transition is used for optical pumping one velocity class into the $3d\,^2\mathrm{D}_{5/2}$ level. The transferred ions are probed via the $3d\,^2\mathrm{D}_{5/2} \rightarrow 4p\,^2\mathrm{P}_{3/2}$ transition with subsequent decay into the ground state as depicted in Fig. 2.8.

4.2.1 Investigation of the initial velocity distribution

For the pump-and-probe scheme, an ion beam with broad and equally populated initial velocity distribution is favored in order to avoid an influence of the underlying initial structure on the final lineshape

---

[2] Tauscher Transformatoren GmbH, HTT 1000-30

which would cause systematic uncertainties as discussed in section 2.4.7. This has been realized by applying a 500-Hz triangular voltage ramp with an amplitude of 8 V_{pp} to the furnace of the ion source leading to an artificial broadening. The resulting population density of the ions leaving the ion source region is expected to be a rectangular function with a width of 8 eV which is much broader than the linewidth of the pumping transition that has been estimated in section 2.4.8 to 29 MHz (before width compression) which corresponds to 1.3 eV for a pre-acceleration of 14 keV.

The velocity distribution of the ions can be investigated in IR2 by irradiating the 393-nm laser on a fixed frequency close to the Doppler shift corrected set point determined from Eq. 2.14 and varying the potential of the chamber (Doppler tuning). The applied scan voltage is set by the data acquisition system and amplified by a Kepco BOP500M high-voltage amplifier while the resonantly scattered fluorescence photons are counted. More detailed information about the measurement parameters can be found in appendix C. The result for a laser power of 1 mW and an ion current of 200 pA is shown by the red dots in Fig. 4.3a in the voltage space (top axis) as well as in the corresponding frequency space (bottom axis). The observed lineshape originates from the convolution of the velocity distribution with the (nearly) Lorentzian lineshape of the transition.

Based on the theoretical assumptions on the lineshape made in section 2.4.8, a spectrum based on a 8-V broad velocity distribution was simulated. In this simulation the initial velocity distribution is divided in 300 velocity classes each filled with 25000 ions. According to the transition probabilities stated in Fig. 2.8 and on the velocity-dependent laser-ion cross section due to the limited transition width that has been quantified in Tab. 2.6, the amount of laser-ion interactions and the resulting fluorescence signal is calculated in a Monte-Carlo principle. A more detailed description of this simulation can be found in appendix A.1. The result is shown as a black line in Fig. 4.3a.

The initial velocity distribution is depicted in blue and relative to the right axis. Measured and simulated data are in excellent agreement which confirms the assumptions of the rectangular-shaped initial velocity distribution. These will be the input parameter for further simulations on the optical pumping.

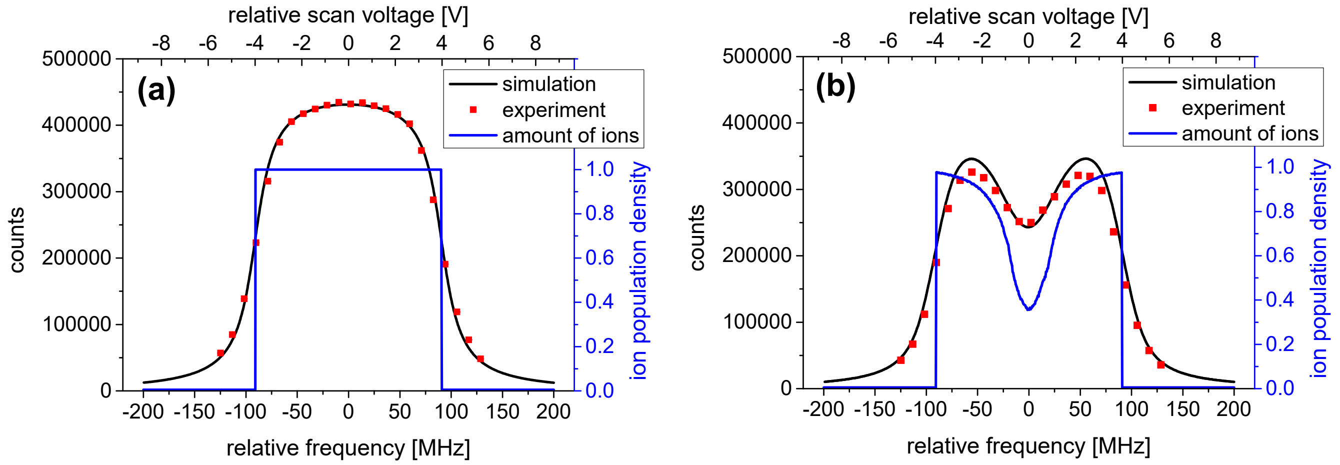

Figure 4.3: Simulated (black) and experimentally observed (red) lineshape of the interaction of the 393-nm laser and the ion beam whose initial velocity distribution was artificially broadened by a triangular voltage ramp with 8 V_{pp}. The top axis shows the scan voltage relative to the center applied to IR2, while the bottom axis represents the Doppler shift in frequency space. (a): Without optical pumping in IR1. (b): With optical pumping in IR1, enabled by floating the drift tubes on the resonant potential. Hence, one velocity class is transferred into the metastable d-state which is a dark state for the 393-nm laser. In blue the corresponding $4s^2$ population density of the velocity classes is illustrated.

4.2.2 Analysis of the optical pumping efficiency

After experimentally taking spectra as shown in Fig. 4.3a, the voltage that is needed to fulfill the resonance condition of the laser-ion interaction can be extracted as the center of the resonance structure. This voltage is then applied to the first interaction region IR1 to perform optical pumping into the probe level. The lineshape observed in IR2 will now exhibit a dip in the center since the ions that have been transferred into the probe state in IR1 cannot interact with the 393-nm laser anymore. The experimental result is shown by the red dots in Fig. 4.3b. The expected dip can clearly be observed in the fluorescence signal. Introducing the optical pumping in the Monte-Carlo simulation allows an analysis of this process. In the 1.2-m long interaction region the ions can interact with the laser several times. The amount of maximal possible excitations was varied until the best match with the experimental data was found. As shown by the black line in Fig. 4.3b, the simulation with up to 18 interactions in the first interaction region describes the experimental data well. The discrepancy in the linewidth of the dip can be explained by a larger power broadening contribution than expected in Tab. 2.6. The size of the laser beams was not measured regularly and was estimated to be 4 mm^2 for both lasers. Hence, there is a relatively large uncertainty in the laser intensity and the corresponding power broadening. The depth of the dip in the observed fluorescence signal seems limited but the resonant velocity class is depopulated by two-thirds as indicated in the simulation (blue). This demonstrates that already with a small feature in the fluorescence signal a significant amount of ions is transferred into the probe level.

Analyzing the amount of laser-ion interactions more detailed (see Fig. 4.4a) shows that most ions which have been transferred into the probe level have interacted only a few times even though up to 18 interactions are possible and a direct excitation has only a probability of 7 %. On the one hand, this is a saturation effect since already transferred ions will not interact with the laser anymore. On the other hand, ions which are slightly off resonance have a smaller interaction probability and will therefore experience less excitations.

The width of the optically-pumped velocity class was extracted from the simulation to be $\Gamma_{\mathrm{FWHM}} = 38\,\mathrm{MHz}$. This is larger than expected (29 MHz in Tab. 2.6) and can be explained by saturation effects. Since several interactions take place and the amount of ions in resonance is decreasing more rapidly than the amount of ions at the edges of the resonance, these are more pronounced in the total resonance signal. Nevertheless, this broadening will not lead to a significant loss in precision since the optically-pumped velocity class will be strongly compressed during the post-acceleration.

4.2.3 Probing of the ions

The ions transferred into the metastable d-state during optical pumping can be probed with the 854-nm laser in IR2. The laser is set to the expected frequency and the scan voltage is varied while the fluorescence signal is recorded. The observed lineshape is the convolution of the optically-pumped velocity class with the lineshape of the probing transition.

For estimating the count rate in the simulation, the transition rates stated in Fig. 2.8 as well as the transition probability for stimulated absorption

$$B_{12} = A_{21} \frac{\lambda^3}{8\pi h} \tag{4.1}$$

yielding $B_{12}(854\,\mathrm{nm})/B_{21}(393\,\mathrm{nm}) = 0.68$ and the laser intensities were considered. In Fig. 4.4b the measured spectrum is compared to the simulation based on the results of the optical pumping discussed above. During this measurement a laser power of 1 mW was used which is twice as much as in typical measurements leading to an expected linewidth of $\Gamma_{\mathrm{FWHM}}(\mathrm{sim}) = 80\,\mathrm{MHz}$ due to larger power broadening contributions. The experimental data yields a linewidth of $\Gamma_{\mathrm{FWHM}}(\mathrm{exp}) = 130\,\mathrm{MHz}$. The discrepancy can be largely explained by the larger width of the pump dip observed already in Fig. 4.3b, which was

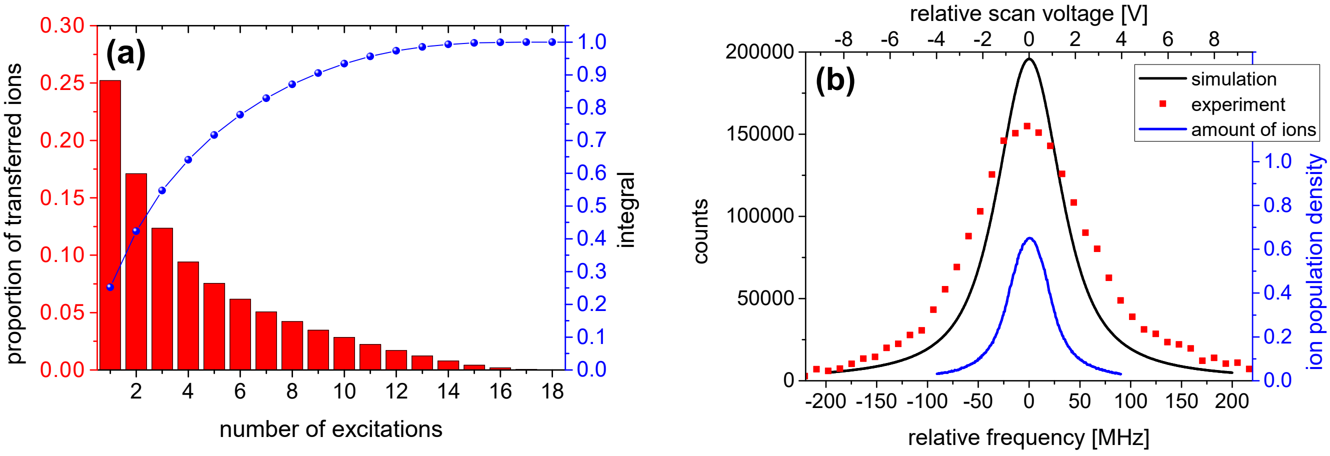

Figure 4.4: (a): Number of laser-ion interactions before the ions are transferred into the metastable d-state. The upper limit was identified by comparing the simulated and experimentally observed dip (see Fig. 4.3b).
(b): Simulated (black) and experimentally observed (red) lineshape of the probing process. The intensity is based on the number of transferred ions from the previous simulation and not adapted to the experimental data. The underlying population density of the velocity classes is illustrated in blue.

not taken into account in the simulation. Experimentally, also smaller widths of about 60 MHz were observed (see, e.g., Fig. 4.7 below). Different power broadening contributions due to different laser beam diameters most likely cause these changes in the observed linewidth. Overall, the simulation agrees reasonably well with the experimental data verifying the assumptions taken in chapter 2.4.

4.2.4 Systematic uncertainties caused during optical pumping

Since the simulation is in reasonable agreement with the experimental data, it can be exploited to investigate systematic effects. As mentioned in section 2.4.7, a systematic shift of the resonance position will occur if the voltage U_{pump} applied to the first interaction region is not chosen correctly. It has to be set in a way that the dip shown in Fig. 4.3b is exactly in the center of the spectrum. Otherwise, the long-ranging tail of the Lorentzian lineshape of the pumping transition which is still present at the edges of the velocity distribution, causes an asymmetry. Corresponding simulations show that this shifts the resonance center by some 100 kHz due to the asymmetric lineshape even for small offsets from the center of the velocity distribution as shown in Fig. 4.5. In the experiment the voltage for optical pumping can be set within an interval of ± 0.2 V relative to the central velocity class. The direction and the intensity

Table 4.3: Systematic shift of the resonance spectrum due to optical pumping 0.2 V off-center of the velocity distribution. The frequency shift is nearly constant for different post-acceleration voltages as well as for the reference measurement. Therefore, the reduced frequency dependence (compare section 2.2.1) can be applied to estimate the corresponding voltage deviation. Fluctuations of the voltage applied to the ion source which have been identified in section 4.1.2 to be 50 mV, will contribute to the statistical uncertainty of up to 5.7 mV.

	Reference	− 5 kV	− 10 kV	− 15 kV	− 19 kV	± 50 mV
δf_{asy}	122 kHz	120 kHz	118 kHz	115 kHz	113 kHz	40 kHz
δU_{asy}		2.0 mV	3.8 mV	5.6 mV	6.8 mV	5.7 mV

of this asymmetry is not predefined and hence, no universal, asymmetric function can be established for fitting the resonance spectra. In Fig. 2.11a the simulated asymmetric lineshape is shown with the corresponding residuals when comparing it to a Voigt fit.

Since the asymmetry is existent in the spectra obtained from high-voltage as well as from reference measurements, this shift partially cancels in the reference-measurement approach. This can be considered by using the reduced frequency dependence $(\partial U/\partial f)_{\mathrm{red}}$ motivated in Eq. 2.24. The corresponding voltage shifts are listed in Tab. 4.3. Additional deviations occur if the pumping position changes between high-voltage and reference measurement. In section 4.1.2, 50-mV fluctuations of the starting potential have been observed which can cause deviations in the high-voltage measurement of up to 5.7 mV contributing to the statistical uncertainty. Increasing the initial velocity distribution even further would lead to a reduction of the resulting uncertainty. On the other hand, this would decrease the amount of ions per velocity class and hence, reduce the amount of ions in the probe level. Since this would increase the statistical uncertainty due to lower count rates, this broadening was chosen as a reasonable trade-off.

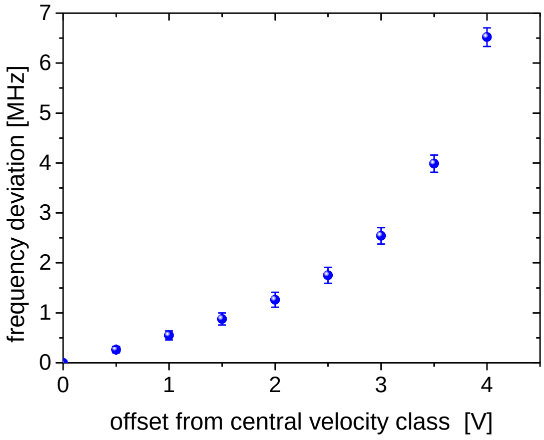

Figure 4.5: Simulated deviation of the center frequency due to an asymmetric lineshape caused through optical pumping off-center of the 8-eV broad, initial energy distribution shown in Fig. 4.3. This finite distribution does not cover the complete, long-ranging tail of the Lorentzian contribution of the lineshape. Hence, asymmetries are induced if optical pumping is performed with an offset from the central velocity class.

4.3 High-voltage measurements

After its successful demonstration, pump-and-probe measurements can be used for a laser-based high-voltage evaluation. But at first, systematic uncertainties due to contact voltages and the ion beam divergence are investigated which becomes possible with this technique.

4.3.1 Contact potential between the interaction regions

Optical pumping is performed in an array of stainless steel drift tubes whereas the probing takes place within the elliptical mirror set made of polished aluminum. Since both materials have different work functions $W_{\mathrm{Al}} = 4.3(1)\,\mathrm{eV}$ [88] and $W_{\mathrm{steel}} = 5.0(1)\,\mathrm{eV}$ [89] a contact potential U_{contact} of

$$U_{\mathrm{contact}} = \frac{W_{\mathrm{Al}} - W_{\mathrm{steel}}}{e} = -0.7(2)\,V \qquad (4.2)$$

between both interaction regions is expected. Depending on the alloy, morphology, preparation and oxidation, the work functions can vary, allowing only a rough estimate of the contact voltage from literature values.

The measurement of the contact potential is performed as follows: The 393-nm laser is set to a fixed frequency. Without artificially increasing the initial velocity distribution, a Lorentzian-like resonance can be detected in IR2 when varying the scan voltage. The resonant voltage identified in this process is then applied to IR1. To allow optical pumping, the initial velocity distribution is broadened by modulating the ion source voltage. A pump dip appears now in the spectrum which is shifted with respect to the previous position by the amount of the contact potential. The determination and comparison of both peak centers resulted in a contact voltage of −1.038(16)(28) V. The statistical uncertainty of 16 mV is mainly due to fluctuations of the laser frequency while the systematic uncertainty of 28 mV is related to peak asymmetries resulting from optical pumping off-center of the velocity distribution as discussed above. It is extracted from Fig. 4.5 for an offset of 1 V. Additionally, long-term drifts of the contact voltage have to be taken into account which cannot be quantified, if this measurement is not regularly repeated. These are not considered in the denoted uncertainty.

Since this effect cancels in the reference-measurement approach, this reveals its advantages compared to a simple two-chamber approach whose accuracy would be limited to at least 44 mV due to the uncertainty of the contact voltage determination.

4.3.2 Ion beam collimation

As discussed in section 2.2.6, the collimation of the ion beam is crucial to avoid systematic deviations. The einzel lenses and the quadrupole doublet introduced in section 3.5 can be used for adjusting the properties of the ion beam whose size can be monitored on the phosphor screens or by the Faraday cups while changing the opening diameter of the iris diaphragms. But although the transmission might be optimal, it cannot be judged, if the ion beam is really collimated.

In a converging as well as in a diverging beam the ions have an angle relative to the laser beam which will result in a reduced Doppler shift. Hence, in case of a collimated ion beam, the Doppler shift is largest which can be detected spectroscopically. By monitoring the resonance position and optimizing the einzel lenses in front of IR2, the ion beam can be collimated very precisely even with an applied post-acceleration voltage. In Fig. 4.6 an exemplary peak centroid shift during a typical optimization procedure is illustrated. In this example the last einzel lens is tuned for a post-acceleration voltage of −15 kV. Applying −6600 (300) V to the einzel lens yields the highest Doppler shift meaning the best collimation of the beam. For higher or lower voltages, the ion beam converges or diverges, respectively. The total shift of 1.5 V which would correspond to uncertainties in the 100-ppm regime demonstrates the importance of a proper collimation. On the other hand, the relative variation on the plateau between −6300 V and −6900 V is less than 10 mV which would still allow a high-voltage determination in the ppm regime.

This procedure is applied to both einzel lenses forming the ion optical telescope (see section 3.5) for each post-acceleration voltage. After few iterations the optimal settings are found which are listed in Tab. 4.4. Since this procedure is performed for the high-voltage as well as for the reference measurements and a remaining divergence would lead to smaller Doppler shifts in both cases, this uncertainty partially cancels. Due to the uncertainty in the identification of the optimal position on the plateau, a total uncertainty of 10 mV can be seen as an upper limit for the consequences of the ion beam collimation after performing the described procedure.

Table 4.4: Experimentally identified einzel-lens voltages to achieve the best ion-beam collimation for different post-acceleration voltages. The ion beam is particularly sensitive to the voltage applied to EL3 since the neighboring electrodes are floated on the high post-acceleration potential as described in section 3.5.

Post-acceleration voltage	Reference	−5 kV	−10 kV	−15 kV	−19 kV
Einzel lens EL2	+ 0.15 kV	+ 0.3 kV	+ 1.5 kV	+ 1.6 kV	0 kV
Einzel lens EL3	0 kV	− 1.4 kV	− 6.3 kV	− 10.3 kV	−13.3 kV

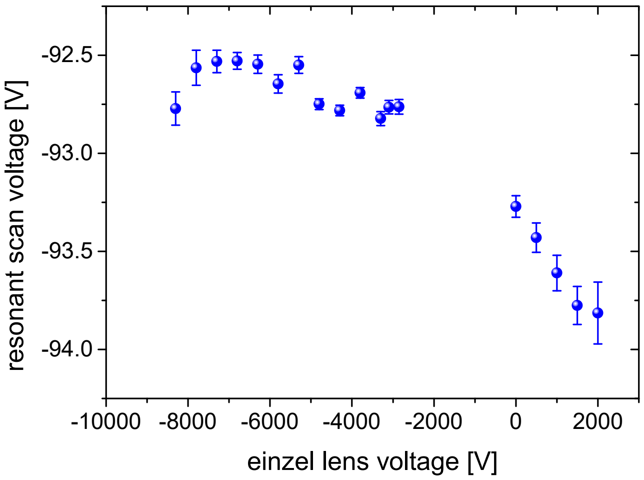

Figure 4.6: Collimation of the ion beam through adjusting the einzel lens voltages while monitoring the resonance position. A collimated beam corresponds to the most positive (decelerating) scan voltage since a diverging or converging ion beam would decrease the Doppler shift. This procedure is performed for the second and the third einzel lens and for every post-acceleration voltage. Here, the optimization of the last einzel lens with an applied high voltage of -15 kV is shown. Each data point consists of a series of several measurements to reduce the statistical uncertainty.

4.3.3 Reference measurement

After the optimization of the ion beam collimation a set of reference measurements is taken before several high-voltage measurements are realized. Afterwards, references are taken again whereof a typical spectrum is shown in Fig. 4.7a.

Even though the spectra are taken by performing Doppler tuning and hence, by varying the scan voltage $U_{\text{scan}_{\text{ref}}}$, the spectra are fitted in the corresponding frequency space to avoid systematic deviations. The center frequency of a single spectrum can usually be identified with a statistical uncertainty of less than 400 kHz corresponding to about 40 mV. When comparing a set of references which is illustrated in Fig. 4.8a, statistical fluctuations with a standard deviation of 650 kHz (60 mV) are observed. As discussed in section 4.1.3, these are mainly caused by frequency fluctuations of the laser for optical pumping. Drifts of the voltages applied to IR1 and IR2 contribute in the order of 10 mV (compare section 4.1.2). After averaging over typically 10 measurements, the resonant scan voltage $U_{\text{scan}_{\text{ref}}}$ required to drive the transition with an irradiated laser of the frequency $f_{\text{L2}_{\text{ref}}}$ can be traced down with a statistical uncertainty of the order of $\Delta U = 10\,\text{mV}$ ($\Delta f = 100\,\text{kHz}$).

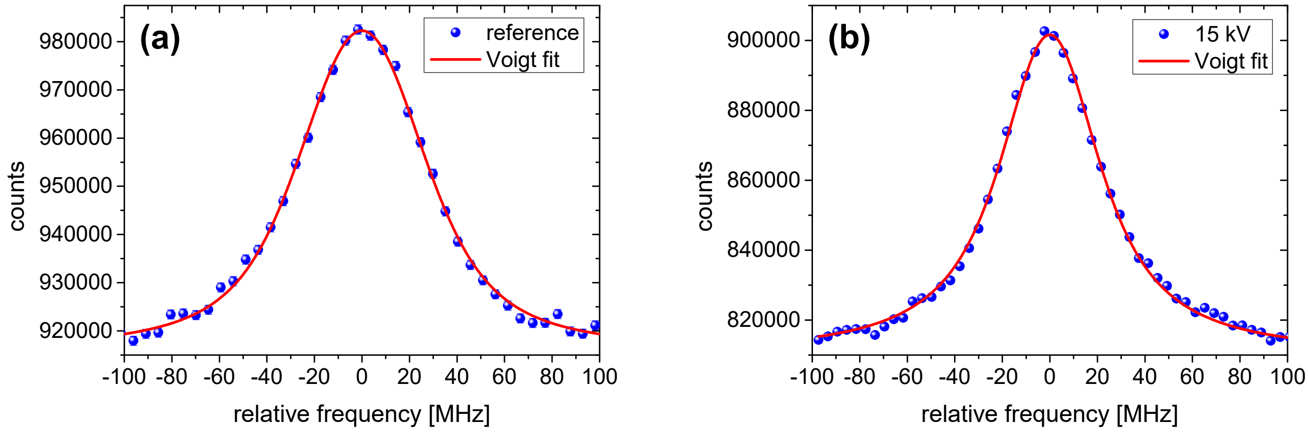

Figure 4.7: (a): Typical spectrum of a reference measurement with an experimentally observed width of $\Gamma_{\text{FWHM}} = 63$ MHz. (b): Typical spectrum of a high-voltage measurement at 15 kV. During the post-acceleration the width of the class of optically-pumped ions is reduced leading to a resulting linewidth of $\Gamma_{\text{FWHM}} = 51$ MHz in the infrared transition. In both cases the center frequency can be identified with an uncertainty of less than 400 kHz.

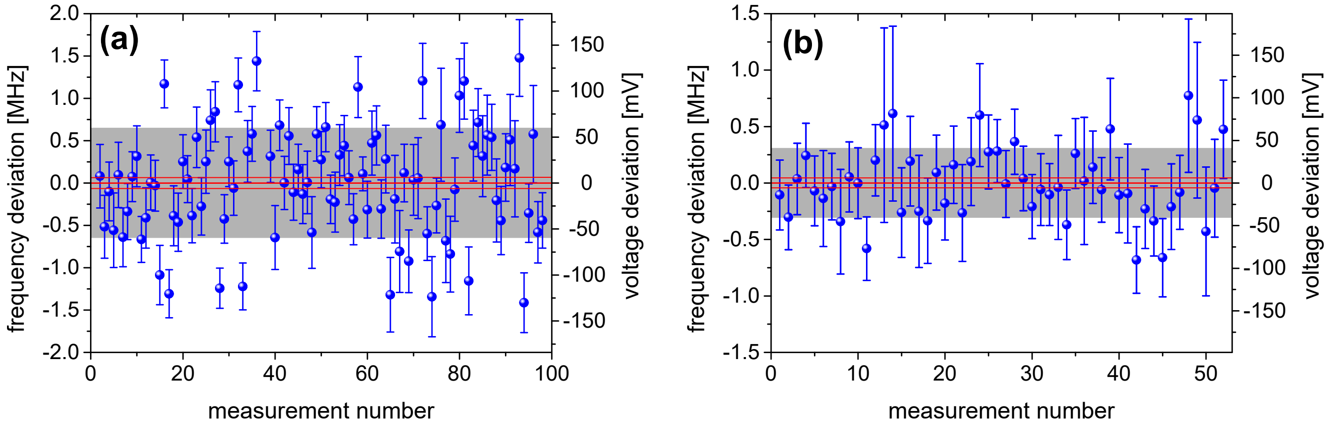

Figure 4.8: Statistical fluctuations of a series of reference (a) and 15-kV high-voltage (b) measurements. The individual measurements scatter with an amplitude of up to 100 mV mainly caused by frequency changes of the laser for optical pumping. The gray shaded area corresponds to the standard deviation interval of about ±60 mV and ±40 mV, respectively. The uncertainty of the weighted average as well as the standard deviation of the mean (red) is about 10 mV, depending on the number of measurements. A typical high-voltage evaluation consist of about 10 reference and 30 high-voltage measurements.

4.3.4 High-voltage measurements

The post-acceleration in a high-voltage measurement results in a compression of the resonance linewidth as illustrated exemplary for a 15-kV measurement in Fig. 4.7b. In this case, the width of $\Gamma_{\mathrm{FWHM}} = 51\,\mathrm{MHz}$ agrees well with the expectations presented in Tab. 2.6. Typically, a series of about 30 measurements is taken to reduce the impact of fluctuations of the laser frequency for optical pumping as shown in Fig. 4.8b. The scan voltage U_{scan} required to drive the transition of the accelerated ions with the laser frequency f_{L2} can be identified with a statistical uncertainty of less than 10 mV. Employing Eq. 2.21, the applied high voltage U_{HV} can be determined as

$$U_{\mathrm{HV}} = \frac{mc^2}{2q}\left(\frac{(f_0 - f_{\mathrm{L2}})^2}{f_0 f_{\mathrm{L2}}} - \frac{(f_0 - f_{\mathrm{L2}_{\mathrm{ref}}})^2}{f_0 f_{\mathrm{L2}_{\mathrm{ref}}}}\right) - U_{\mathrm{scan}} + U_{\mathrm{scan}_{\mathrm{ref}}}\,. \tag{4.3}$$

This procedure was carried out for high voltages of −5 kV, −10 kV, −15 kV and −19 kV. The results have been compared to the voltage measured with the HVA100 high-voltage divider and an additional high-voltage divider (PT20, relative accuracy 5 ppm) provided by the PTB as illustrated in Fig. 4.9. The gray area corresponds to the uncertainty of the high-voltage dividers whereas the error bars correspond to the uncertainty of the laser-based measurement. The origin of the systematic uncertainties like, e.g., angular misalignment inherently leads to asymmetric error bars. Taking all contributions into account, the total uncertainty of the laser-based high-voltage evaluation is about 5 ppm (compare Tab. 4.5).

The voltages obtained with the HVA100 and the PT20 high-voltage divider disagree by up to 7 ppm explaining the displacement of both data sets. The HVA100 measures systematically less negative voltages than the PT20 while the latter shows an almost constant deviation of about −5 ppm from the laser-based determination. However, since both dividers have a confidence interval of 5 ppm, these results are in excellent agreement.

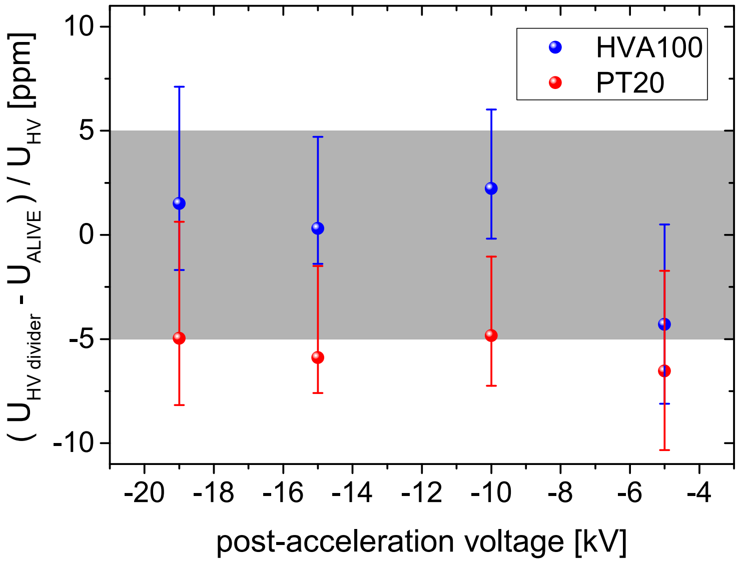

Figure 4.9: Relative deviation between the high voltages measured with ALIVE and with two conventional 5-ppm high-voltage dividers for voltages from −5 kV to −19 kV. The divider uncertainty is shown by the shaded band, whereas the uncertainties of the ALIVE measurements derived in Tab. 4.5 are represented by the error bars.

4.3.5 Discussion of the uncertainty

The statistical uncertainties as well as all considered systematic contributions are summarized in Tab. 4.5. Furthermore, the corresponding sections with a detailed discussion of the respective contribution are referenced.

Since the statistical uncertainty originates mainly from changes of the laser frequency and from fluctuations of the voltages U_{pump} and U_{HV} applied to IR1 and IR2, it is independent from the applied high voltage but depends on the number of performed reference and high-voltage measurements. Typically, 10 reference and 30 high-voltage measurements were performed. For both sets of measurements, the standard deviations of the mean of about 10 mV were taken as the uncertainty for ΔU_{scan} and $\Delta U_{\text{scan}_{\text{ref}}}$, respectively. These were added in quadrature, yielding the symmetric total statistical uncertainty of about 2 ppm.

The systematic uncertainties will preferably shift the ALIVE value towards smaller voltages. Especially the contribution δU_{angle} is responsible for this asymmetry since an angular deviation can only cause smaller Doppler shifts. For negative high voltages, this would result in shift to a less negative voltage. Hence, the applied voltage is preferably more negative than determined in this approach, leading to a one-sided uncertainty which is indicated in Tab. 2.2 by the (−) sign. Besides the angular misalignment, the ion beam divergence is a major contribution. Since this depends on the tuning of the einzel lenses as discussed in section 4.3.2, it is independent from the post-acceleration voltage. Its direction is not predefined and can change depending on the quality of the ion-beam collimation in the reference and the high-voltage measurement. The third largest contribution, the impact of asymmetric lineshapes arising from optical pumping off-center of the initial velocity distribution, was quantified in simulations as discussed in section 4.2.4. The derivation of the smaller contributions can be found in section 2.2.

Summing up all contributions leads to systematic uncertainties at the 5-ppm level which is already a 20-fold improvement in accuracy of laser-based high-voltage measurements compared to previous attempts [19, 22]. The statistical uncertainties can be even reduced below 1 ppm if a sufficient amount of measurements is taken. Further reduction of the systematic uncertainties seems possible and will be discussed later.

Table 4.5: Statistical and systematic uncertainties considered in the laser-based high-voltage evaluation with Ca^+ ions. For the different contributions refer to sections listed in the last column. In case of directed contributions, this is indicated with (+) and (−) signs. The total uncertainty of all measurements is at the 5-ppm level.

	−5 kV	−10 kV	−15 kV	−19 kV	discussion
δU_{stat}	14 mV	18 mV	13 mV	46 mV	4.1.3
$\delta U_{\mathrm{stat}}/U_{\mathrm{HV}}$	± 2.7 ppm	± 1.8 ppm	± 0.9 ppm	± 2.4 ppm	
$\delta U_{\mathrm{angle}}$	− 5.7 mV	− 16 mV	− 44 mV	− 74 mV	4.1.1
δU_{div}	± 10 mV	± 10 mV	± 10 mV	± 10 mV	4.3.2
δU_{asy}	± 2.0 mV	± 3.8 mV	± 5.6 mV	± 6.8 mV	4.2.4
$\delta U_{\mathrm{Gauss}}$	± 0.5 mV	± 0.8 mV	± 1.2 mV	± 1.5 mV	2.2.7
$\delta U_{\mathrm{penetration}}$	− 0.5 mV	− 1.0 mV	− 1.5 mV	− 1.9 mV	2.2.12
$\delta U_{\mathrm{charge}}$	+ 0.1 mV	+ 0.2 mV	+ 0.3 mV	+ 0.3 mV	2.2.13
δU_{scan}	± 0.2 mV	± 0.2 mV	± 0.2 mV	± 0.2 mV	4.1.2
δU_{f_0}	± 1.2 mV	± 2.3 mV	± 3.2 mV	± 3.9 mV	2.2
δU_{sys}	$^{+14}_{-20}$ mV	$^{+17}_{-33}$ mV	$^{+21}_{-65}$ mV	$^{+23}_{-97}$ mV	
$\delta U_{\mathrm{sys}}/U_{\mathrm{HV}}$	$^{+2.8}_{-3.9}$ ppm	$^{+1.7}_{-3.3}$ ppm	$^{+1.4}_{-4.3}$ ppm	$^{+1.1}_{-5.1}$ ppm	
$\delta U_{\mathrm{total}}/U_{\mathrm{HV}}$	$^{+3.8}_{-4.8}$ ppm	$^{+2.4}_{-3.8}$ ppm	$^{+1.7}_{-4.4}$ ppm	$^{+3.2}_{-5.6}$ ppm	

4.3.6 Collisions with residual gas

As discussed in section 2.2.9 no shifts due to collisions with residual gas are expected. To prove this hypothesis, the vacuum conditions were worsened through turning off the vacuum pumps. While the pressure increased from 10^{-8} mbar to 10^{-6} mbar, a series of reference measurements was taken. Comparing these measurements, one would expect to measure a decelerating shift. This would correspond to a more negative resonant scan voltage. As depicted in Fig. 4.10, this could not be observed, only the usual scatter due to the laser stabilization. This confirms the assumption that no systematic deviations due to the collisions have to be considered.

Contrary, S. Götte et al. observed a shift of nearly 1 V when changing their vacuum conditions from $0.6 \cdot 10^{-6}$ mbar to $2 \cdot 10^{-6}$ mbar [19]. This unexpected large impact of the vacuum conditions probably originated in an even worse vacuum near to their ion source. This can strongly affect the high-voltage evaluation in the one-chamber approach which was applied there. Furthermore, they worked with ions excited into the metastable d-state naturally in their hot cavity ion source. Since they also observed an increase of the count rate with increasing residual gas pressure, they concluded that a large amount of the ions is not excited in the source but by collisions with molecules. This also indicates even worse vacuum conditions near to the ion source.

At the ALIVE experiment, no ions in the metastable d-state were observed without populating it artificially through optical pumping in usual working conditions which demonstrates the much better conditions in this setup.

4.3.7 Conclusion and comparison with precursors

As mentioned before, S. Götte et al. and E. Will et al. also performed laser-based high-voltage measurements with Ca^+ ions. These previous attempts are dedicated for comparing the achieved accuracy and the remaining systematic uncertainties.

In the experimental setup of S. Götte et al. [19] the one-chamber approach was applied in the early

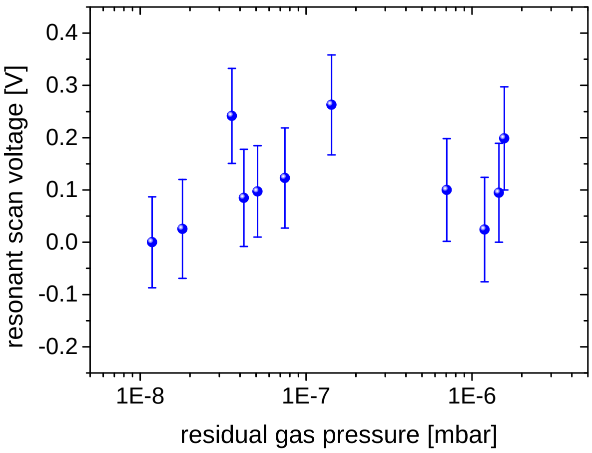

Figure 4.10: Dependency of the high-voltage measurement from the residual gas pressure. Collisions would reduce the ion velocity corresponding to a shift to a more negative resonant scan voltage. Besides the usual statistical scatter such a shift cannot be observed, which confirms the assumptions made in section 2.2.9.

2000's. As discussed in the previous chapter, the ions which where excited to the metastable d-state in the ion source were probed after an acceleration of up to 50 keV. But due to bad vacuum conditions it remained unclear if these ions were excited in the source or through collisions with residual gas. Since the latter would reduce the ion velocity, this caused a systematic uncertainty of 2.5 V. Furthermore, the starting potential in the ion source could not be determined more accurately than 2 V. Besides these, the frequency determination (0.9 V) and the angular alignment of laser and ion beam (0.4 V) were the largest contributions to the total uncertainty of about 6 V which corresponds to a relative uncertainty of the voltage determination of more than 100 ppm. Since the accuracy was mainly limited due to effects caused by the ion source, they proposed a two-chamber approach. Modifying their setup, a pseudo two-chamber approach could be realized [50]. However, due to the population of the metastable state through collisions with residual gas, it was not feasible to perform high-voltage measurements following this approach within their experimental setup.

In 2013, E. Will et al. performed high-voltage measurements in a multi-purpose beamline for collinear laser spectroscopy experiments. Measurements in the one-chamber approach were performed by exciting the ions from the ground state to the p-state. After fixing some problems with the correct determination of the mode number of the frequency comb, a 10-kV measurement with an accuracy of $2 \cdot 10^{-4}$ [51] could be realized which reproduced the results from Götte. The main contributions to the systematic uncertainty were the starting potential in the ion source and the angular alignment of laser and ion beam. Furthermore, they could establish measurements in a two-chamber approach where the same pumping and probing scheme as in the ALIVE experiment was used. Here, only high voltages of some kV could be applied since this setup was not designed for a two-chamber high-voltage evaluation. A constant offset of +1.7 V compared to a measurement with a conventional high-voltage divider was observed for all applied post-acceleration voltages (−2 kV, −3 kV and −4 kV) which was most likely caused by a contact potential between the two interaction regions. This was not investigated during the measurement campaign but half a year later where a potential of −2 V could be identified which did not solve the puzzle of the observed offset [22]. However, the relative accuracy of the different high-voltage measurements was very high which indicated the advantages of the two-chamber approach.

Applying the reference-measurement method in an ultra-high vacuum beamline, the systematic uncertainties can be further reduced as demonstrated in the ALIVE experiment. In particular, this approach cancels the unknown starting potential and the collisions with residual gas observed by Götte. Additionally, the uncertainty of the laser frequency determination is drastically reduced since a frequency comb is available. The contact potential between both interaction regions which limited Will et al. is also avoided in the reference-measurement approach since both ion-laser interactions contributing to the high-voltage evaluation are performed at the same place. Furthermore, the superposition of both beams is realized more accurately, because at the ALIVE setup dedicated beam diagnostic stations in a sufficient distance are available. This allowed to perform measurements in the 5-ppm regime with the same ion species used which corresponds to an improvement of at least a factor of 20 compared to the previous attempts for laser-based high-voltage evaluations.

The 5 ppm accuracy achieved so far is still not the limit for laser-based high-voltage measurements. After analyzing the different contributions to the total uncertainty listed in Tab. 4.5, their origin was traced down to further reduce its consequences on the high-voltage measurements.
The largest uncertainty contribution is caused by the misalignment of ion optical elements between both interaction regions. A further improvement of this mechanical adjustment is still possible after some modifications in the mounts of the electrodes (see outlook Fig. 6.1). Another large uncertainty contribution is caused by the ion beam divergence. There, an ion source emitting a beam with a much smaller emittance could help to achieve a better ion beam collimation. This would also improve the superposition of both beams which was limited through the large ion beam diameter so far. Additionally, a shielding of the earth magnetic field would decrease this uncertainty. Therefore, this approach still opens the opportunity for a further reduction of its systematic uncertainty.
Besides this, the statistical uncertainty has to be improved to establish high-voltage measurements in the 1-ppm regime. The statistical fluctuations of the measurements were mainly caused by frequency changes of the laser for optical pumping. A better stabilization of this laser or an online measurement of its frequency would reduce this scatter. Furthermore, the uncertainty in the determination of the resonant laser frequency/scan voltage could be decreased, if the transition linewidth would be minimized. Hence, improvements in the high-voltage evaluation can be achieved with narrow-linewidth ions generated in a low emittance ion source. Therefore, In^+ ions which can be produced with low emittance in a liquid metal ion source and have a suitable transition with a natural linewidth of only 360 kHz, seem to be promising.

5 Measurements with In^+ ions

In summer 2018 the liquid metal ion source for the production of a high-quality In^+ ion beam and two laser systems generating light at 230.7 nm were available for a period of two month. During this time the feasibility of high-voltage measurements with this ion species was investigated and the rest-frame transition frequencies of $5s^2\ ^1S_0 \rightarrow 5s5p\ ^3P_1$ transition were determined.

5.1 Developments in the experimental setup

After analyzing the high-voltage measurements with Ca^+ several possibilities to improve the accuracy became clear. There, the statistical uncertainty was dominated by fluctuations of the laser frequency for optical pumping whereas the largest contributions to the systematic uncertainty were caused by the superposition of ion and laser beams and the divergence of the ion beam.
Since a low-emittance ion beam is available from the liquid metal ion source (compare section 3.2), the uncertainty due to the ion beam divergence is significantly reduced in case of In^+ even for high post-acceleration voltages when applying the optimization procedure described in chapter 4.3.2. Also the uncertainty due to the alignment has been decreased by shielding the magnetic field which is discussed in the next section. However, an improved alignment of the electrodes which caused the largest uncertainty contribution in case of high post-acceleration voltages, could not be realized before the measurements but will be discussed in the outlook in chapter 6.
A direct stabilization of both laser systems to the frequency comb as discussed below prohibits frequency fluctuations and leads to less statistical scatter of the individual measurements. Additionally, the stray light was reduced further by installing an exit window which is tilted by 5 ° and most importantly by improving the laser beam properties: The size of both laser beams has been reduced to $2\,\mathrm{mm}^2$ leading to less reflections on apertures in the beamline. Furthermore, the remaining stray light is suppressed since the UV light is absorbed much stronger from the metallic surfaces than the 400-nm light in case of Ca^+. Overall, background rates on the kHz level were reached.
Besides this, a 17-cm long drift tube directly in front of the second interaction chamber was prepared to perform Doppler tuning in this section. Due to the long lifetime of the excited state, it is possible to excite the ions in the drift tube and still collect fluorescence photons in the optical detection region. By fast blocking of the laser light with an acousto-optical modulator, this enables background-free spectroscopy. For this purpose, the time-resolved data acquisition system TILDA [90, 91] was established at the ALIVE setup.

5.1.1 Shielding of external magnetic fields

Even a weak magnetic field can limit the accuracy of the laser-based high-voltage measurement since it induces a curved ion trajectory (compare section 2.2.5). Furthermore, the precision will be decreased due to an increased linewidth caused by the Zeeman effect. As shown before in Tab. 2.6, Zeeman broadening is expected to be one of the largest contributions to the resulting linewidth of the $^1S_0 \rightarrow {}^3P_1$ transition in In^+.
The first action to reduce the magnetic field was the removement of the two ion getter pumps. These induced a vertical magnetic field in IR2 five times larger than the earth magnetic field as shown in Fig. 5.1a. Measurements with a Hall probe were taken above and beneath IR2 with and without ion getter pumps. Its mean corresponds to the field inside the chamber.

Additionally, both interaction regions were shielded by two layers of Mu-metal[1] foil, a material with a very high magnetic permeability. Guiding the magnetic field lines along the foil, the field strength inside the vacuum chamber is reduced. A measurement performed with a Hall probe at the very beginning of the first interaction region (IR1) and at its high-voltage feedthrough (IR1-HV) demonstrated the reduction of the magnetic field by at least a factor of 10 as depicted in Fig. 5.1b. Since these measurements could only be taken with a hall probe placed at the edge of the shielded area, the reported shielding rates are lower limits for the real operation.

With these arrangements, the magnetic field inside the interaction chambers and its impact on the high-voltage measurements could be significantly reduced. Other sources of magnetic fields like the bearings of turbo-molecular pumps do not have a large impact. They are placed at relatively large distances from the interaction chambers, their magnetic fields are much weaker and they will also be shielded by the Mu-metal foils.

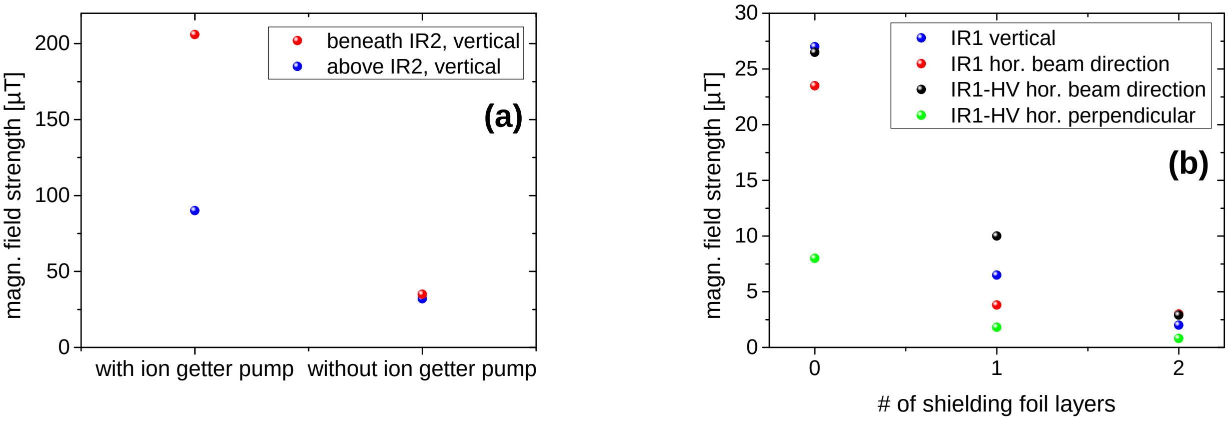

Figure 5.1: Reduction of the magnetic field inside the beamline. The ion getter pumps have been removed (a) decreasing the magnetic field in IR2 by a factor of five. The remaining earth magnetic field was shielded with two layers of Mu-metal foil (b). Measurements performed at the beginning of the first interaction region (IR1) and at its high-voltage feedthrough (IR1-HV) yielded a reduction of at least a factor of ten.

5.1.2 Stabilization of the laser frequency

To decrease the statistical uncertainty of the laser-spectroscopic measurements, a new stabilization scheme for both laser systems was established. The frequency fluctuations caused by drifts of the wavemeter and the HeNe that have been observed during the measurements with Ca^+ (compare section 4.1.3) are avoided through a direct stabilization to the frequency comb. This was realized by superimposing a fraction of light generated by the Matisse Ti:Sa laser with the frequency comb. The beat frequency is detected with a photo diode and counted with an integration time of one second before it is used to calculate the absolute laser frequency. By digitally sending this beat frequency to the laser control software "Matisse Commander" and using it to regulate the reference cavity, a stability of 80 kHz for the first Matisse and of 60 kHz for the second Matisse was achieved for the fundamental frequency. This corresponds to an improvement by a factor of 10 compared to the previous regulation scheme. During the fourth-harmonic generation (FHG) process also the amplitude of the scatter is increased leading to 231-nm lasers with a frequency stability of 310 kHz and 250 kHz as depicted in

---

[1] Mu-metal © is an alloy of nickel (80 %), molybdenum (5 %) and iron (15 %) with a relative permeability of up to $\mu_R = 10^5$.

Table 5.1: Frequency-comb-based absolute frequency determination of both frequency-quadrupled lasers. The fundamental frequency is measured with an integration time of 1 s and multiplied by a factor of four to account for the FHG. The laser frequency scatters with the given standard deviation σ_f around the central frequency f_L. One laser system is used for optical pumping and for probing in case of a reference measurement whereas the other system is used for probing post-accelerated ions.

	laser frequency f_L	standard deviation σ_f
pumping and reference	1 298 963 805. 31 MHz	0.31 MHz
probing	1 298 941 285. 19 MHz	0.25 MHz

Fig. 5.2. This is the first time that this stabilization scheme was realized for this laser system. The difference in the stability of both laser systems is caused by different electronic amplification factors of the reference-cell piezo used to adjust the length of the cavity.

Besides the much smaller fluctuations, this approach also has the advantage that the laser is indirectly stabilized to an absolute frequency standard avoiding long-term drifts. Further improvement of the stability is still possible by using even smaller amplification factors of the reference cell which can be realized by the exchange of the corresponding electronic board. Alternatively, a more stable reference cell can be used. An even larger gain in stability could be achieved by increasing the read-out rate of the beat frequency. It is 1 Hz for highest precision and cannot be changed in the software of the frequency comb. However, with an additional counter working at a higher rate, a faster regulation can be realized. This will not affect the counting accuracy since it is still several orders of magnitudes larger than the uncertainty caused by the laser fluctuations.

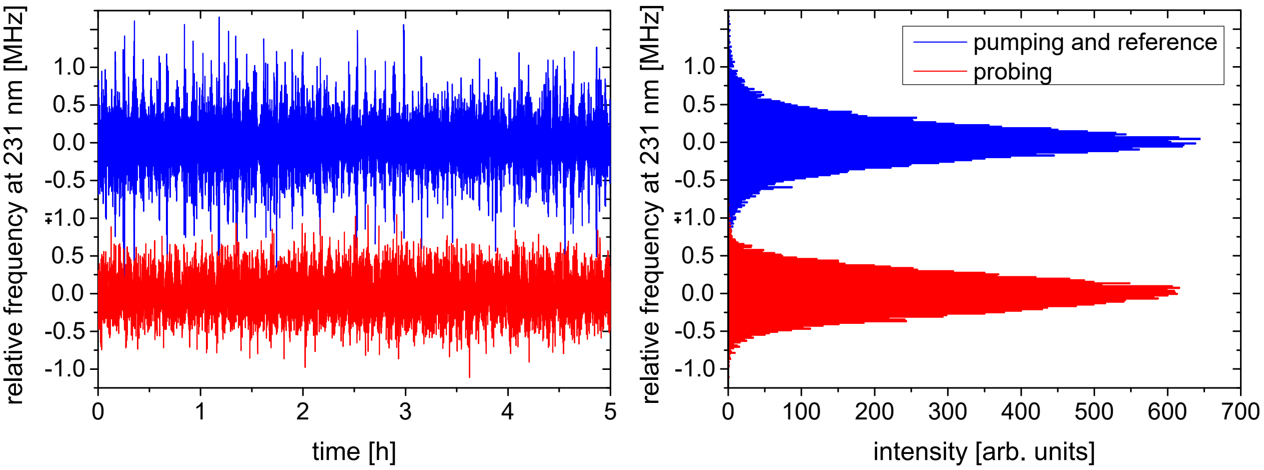

Figure 5.2: Laser stability during the high-voltage measurements with In$^+$ ions. Both lasers have been stabilized to the frequency comb eliminating long-term drifts. When measuring the frequency with an integration time of 1 s, frequency fluctuations with a standard deviation of 310 kHz after FHG were observed for the first laser system used for optical pumping and for probing in case of a reference measurement (blue). Due to a smaller amplification factor for the voltage applied to the reference-cell piezo, the fluctuations of the second laser system used for probing post-accelerated ions (red), could be reduced to 250 kHz after FHG.

The strongly reduced background allowed us to perform laser-spectroscopic measurements on the intercombination transition of In^+. As discussed in section 3.6, the ion-current normalized fluorescence rate of In^+ is a factor of 5000 smaller compared to Ca^+ mainly due to the considerably smaller A_{12} factor. The In^+ ion current was chosen to be 2 nA since the stability of the beam intensity was highest under these conditions. This corresponds to an increase by only a factor of ten compared to Ca^+.

The fluorescence rate observed for a laser power of 1 mW is of the order of 10 kHz per PMT which is relatively small compared to the former background level of several 100 kHz. As shown in Fig. 5.3, a signal-to-background ratio of 2.5:1 has been achieved with the improved conditions. There, the $5s^2\ {}^1\mathrm{S}_0\ \mathrm{F}{=}9/2 \rightarrow 5s5p\ {}^3\mathrm{P}_1\ \mathrm{F}{=}11/2$ transition was measured via a variation of the scan voltage applied to the optical detection chamber. Besides the most abundant ${}^{115}_{49}\mathrm{In}$ isotope (95.7 %) also ${}^{113}_{49}\mathrm{In}$ (4.3 %) is clearly observable.

The observed asymmetry in these measurements is ascribed to a partial overlap between ion and laser beam combined with the dynamical properties of the 10° deflector used to superimpose both beams. The deflector acts as an energy filter and distributes ions with different velocities in a direction perpendicular to the ion beam direction in the horizontal plane. A partial overlap will therefore exclude a part of the velocity distribution from the interaction with the laser light and reduce the intensity in one wing of the resonance. This asymmetry requires a careful modeling of the lineshape. Otherwise it leads to deviations of several MHz in the determination of the central frequency of the 500-MHz (22-V) broad resonance. After an improved overlap between both beams, the asymmetry was removed as is demonstrated in Fig. 5.4. This supports the explanation for the asymmetry.

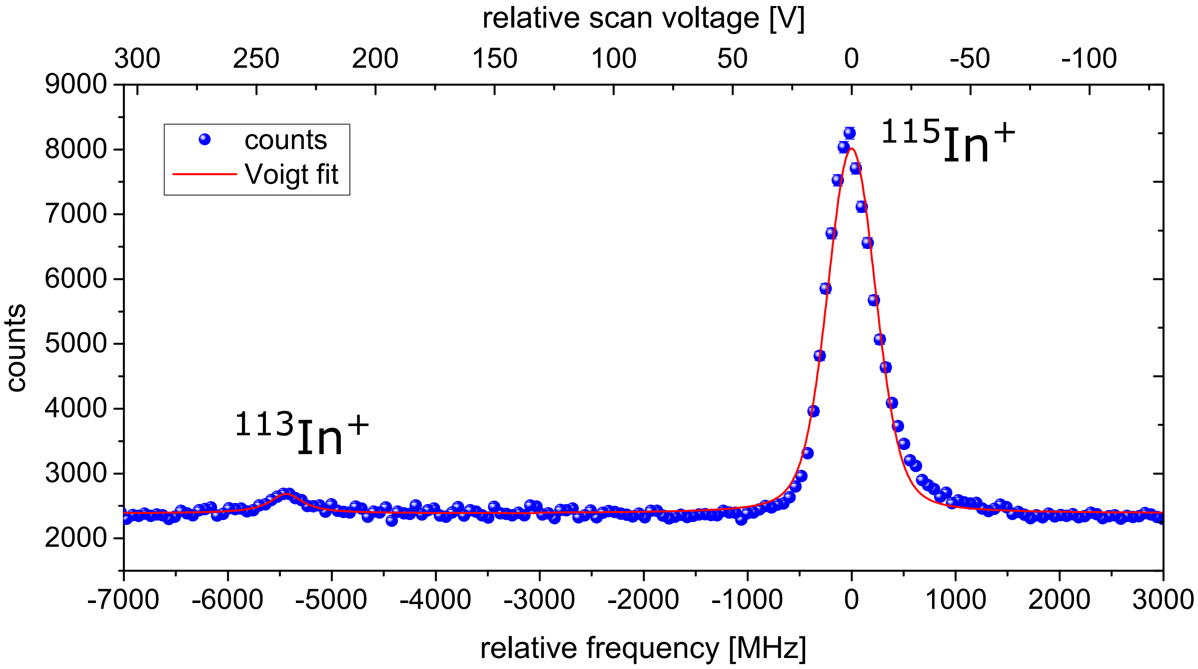

Figure 5.3: Resonance spectra of the $5s^2\ {}^1\mathrm{S}_0$ F=9/2 → $5s5p\ {}^3\mathrm{P}_1$ F=11/2 transition in ${}^{113}_{49}\mathrm{In}^+$ and ${}^{115}_{49}\mathrm{In}^+$. The top axis shows the relative scan voltage applied to IR2, while the bottom axis represents the Doppler shift in frequency space. The peak asymmetry is ascribed to a partial overlap between ion and laser beam as discussed in the text.

5.1.4 Background-free measurements

The background reduction was carried out and specified for the anticollinear operation of the beamline which is the usual mode for laser-based high-voltage measurements at ALIVE. In collinear geometry, the background rate is still a factor 25 larger than in the anticollinear case which precludes the possibility to perform (fast) measurements in both laser directions. To overcome this limitation, a 17-cm long drift tube directly in front of the optical detection region was prepared to perform Doppler tuning. The long lifetime of the excited state of 440 ns, corresponding to a flight path of 10 cm for 15-keV ions, allows us to separate laser excitation and fluorescence detection. The excitation occurs inside the drift tube, whereas the detection is performed after the laser has been quickly turned off with an AOM.

The loss of efficiency due to the delayed detection can be observed in Fig. 5.4a where Doppler tuning is performed in the drift tube and a continuous, anticollinear laser beam is used. The optical detection region was fixed at a potential far off the resonance condition whereof only the first chamber is used since the signal in the second chamber has diminished. Since the measurement parameters like ion current and laser power are similar to the conditions where the interactions took place in the optical detection region, the signal-to-background ratio of 0.35:1 can be used to estimate the relative amount of detected fluorescence photons. Assuming the background rate to be constant, the fluorescence rate dropped to 14 %. Even with this loss, the procedure has the advantage that the background from the scattered light can be completely suppressed by turning off the laser during the detection time which leads to a considerably increased signal-to-noise ratio. This has been realized for the collinear case, which has a dramatically higher background rate, with an acousto-optical modulator placed behind the quadrupling stage as described in section 3.7.2. A resonance spectrum taken under these conditions in pulsed mode and in a similar measurement time (8 min) is shown in Fig. 5.4b. The beam-on/beam-off periods were chosen as 10 µs/2 µs leading to another efficiency loss of a factor six. Hence, the total intensity in the collinear pulsed mode is much smaller but since there is very little background, a similar signal-to-noise ratio of 25:1 compared to the anticollinear continuous mode (22:1) is achieved. It turned out after the measurement that most of the remaining background light is caused by the vacuum gauges. In both cases the spectra have a width of $\Gamma_{\mathrm{FWHM}} \approx 500$ MHz and their resonance frequency can be determined with an uncertainty of approximately 4 MHz. The Voigt profile fitted to the experimental data is dominated by the Gaussian contribution which confirms the expectations on the ion production process regarding the initial velocity distribution.

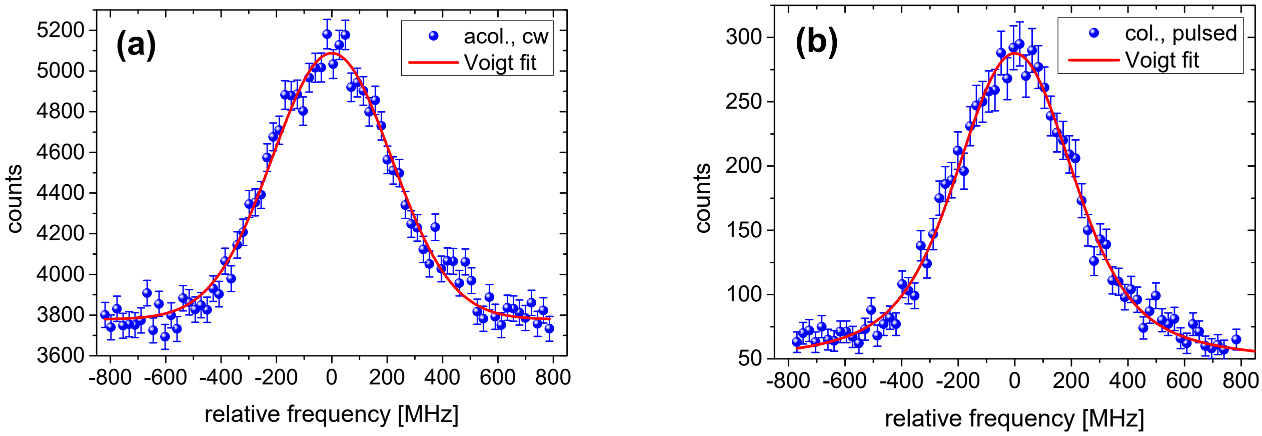

Figure 5.4: Resonance spectra of $^{115}\mathrm{In}^{+}$ obtained by varying the scan voltage applied to the drift tube in front of the optical detection chamber. (a): Continuous measurement in anticollinear geometry. (b): Background-free measurement realized with time-resolved data acquisition and a pulsed laser beam in collinear direction. In both cases the spectra are well described by a Voigt profile with a width of $\Gamma_{\mathrm{FWHM}} \approx 500$ MHz. All measurement parameters can be found in appendix C.

5.2 Determination of the rest-frame transition frequencies

The excited $5s5p\ ^3\mathrm{P}_1$ level splits into three hyperfine states separated by about 35 GHz. The transition to the $F = 11/2$ state is known with an accuracy of 100 kHz [54] from a current trap measurement whereas the most precise measurement of the transitions to the $F = 9/2$ and $F = 7/2$ hyperfine levels were performed with an échelle monochromator [55] and are reported with an uncertainty of 180 MHz. Since the high-voltage evaluation requires an accurate knowledge of the rest-frame frequency, only the $5s^2\ ^1\mathrm{S}_0\, F = 9/2 \rightarrow 5s5p\ ^3\mathrm{P}_1\, F = 11/2$ transition can be employed. However, with a collinear setup and two laser systems it is possible to precisely identify the other transition frequencies by using Eq. 2.6 as described in section 2.1.1.

For the determination of the rest-frame transition frequencies, a series of alternately performed collinear (c) and anticollinear (a) measurements with the settings described in section 5.1.4 was taken. To preclude uncertainties from unresolved long-term drifts, the applied measurement scheme was a-c-c-a. Collinear and anticollinear laser-ion interaction took place in the drift tube in front of the optical detection region whereof the first PMT was used to collect the fluorescence photons. In anticollinear geometry the measurement was performed with the laser beam continuously turned on. The beam was blocked with the AOM during fluorescence detection in the collinear case. Typical resonance spectra are depicted in Fig. 5.4.

As demonstrated in Eq. 2.6, the rest-frame transition frequency f_0 can be determined by multiplying the resonant frequencies f_c and f_a obtained in collinear and anticollinear measurements, respectively, if both are detected from an ion beam with identical velocity β. But since Doppler tuning is applied, the ion velocity is varied and this equation is not applicable as long as the two resonances do not appear at exactly the same scan voltage. This can be cured by choosing both frequencies in a way that the resonance signal appears at (nearly) the same scan voltage. The remaining small deviations of the resonant scan voltage ΔU_scan can be corrected after fitting: The difference is linearly approximated with $\delta f = \partial f / \partial U \cdot \Delta U_\mathrm{scan} = \kappa^{-1} \cdot \Delta U_\mathrm{scan}$ and one of the frequencies is corrected by this amount before Eq. 2.6 is applied. This yields

$$f_0 = \sqrt{(f_\mathrm{c} - \kappa^{-1} \cdot \Delta U_\mathrm{scan}) \cdot f_\mathrm{a}} - \Delta f_\mathrm{recoil} \, . \tag{5.1}$$

Here, also the shift due to the photon recoil Δf_recoil (see section 2.2.8) is taken into account.

Applying this method, the rest-frame transition frequencies between the ground state and all three hyperfine states of the $5s5p\,^3\mathrm{P}_1$ level were measured. The results are listed in Tab. 5.2. By taking seven pairs of collinear and anticollinear measurements for the transition to the $F = 11/2$ state and nine pairs for the other transitions, the statistical uncertainty was reduced to less than 1.5 MHz. This corresponds to the uncertainty of the weighted average that is slightly larger than the standard deviation of the mean. The systematic uncertainty is estimated to be less than 3 MHz and is discussed in detail in the next section.

In literature three groups have reported measurements on the $5s^2\ ^1\mathrm{S}_0 \rightarrow 5s5p\ ^3\mathrm{P}_1$ transition of In^+ neglecting the measurement of Paschen and Campell carried out in 1938 [92]. Most recently (2007) Wang et al. [54] measured the transition to the $F = 11/2$ level on a single ion in a radio-frequency trap. The laser frequency was measured with a frequency comb leading to a small uncertainty of 100 kHz. In the early 1990's, Peik et al. [57] also used a radio-frequency trap where they stored a cloud of In^+ ions. They referenced their laser frequency on Te lines and were limited by the nonlinearity of the laser scan and the linewidths of indium and tellurium to approximately 600 MHz. At the same time Larkins and Hannaford [55] performed measurements with an échelle monochromator on In^+ which was excited inside a neon-filled hollow-cathode lamp. Spectral lines of iron generated in another hollow-cathode lamp were used for calibration. With that technique, they claimed an accuracy of 150-180 MHz.

When comparing the literature values with our results, an excellent agreement with both trap measurements is observed. The very precise value of Wang et al. differs only by 1.2 MHz and serves as confirmation of the accuracy of our measurement. The results of Peik et al. differ by less than 90 MHz

Table 5.2: Rest-frame transition frequencies of the $5s^2\ ^1\mathrm{S}_0 \rightarrow 5s5p\ ^3\mathrm{P}_1$ transition in $^{115}\mathrm{In}^+$. The values determined laser spectroscopically in this work are in excellent agreement with the measurements performed in ion traps [54, 57]. The measurement performed with a monochromator [55] shows a systematic deviation of nearly 300 MHz indicating a wrong calibration of their apparatus. The statistical uncertainty of our measurement is less than 1.5 MHz whereas systematic contributions due to the lineshape of 3 MHz are considered. The hyperfine splitting parameters have been extracted to be $A = 6957.2(5)$ MHz and $B = -443.7(3.5)$ MHz. All values are in MHz.

	$F = 9/2 \rightarrow F = 11/2$	$F = 9/2 \rightarrow F = 9/2$	$F = 9/2 \rightarrow F = 7/2$
This work	1 299 648 955.7 (1.2) (3.0)	1 299 611 097.9 (1.4) (3.0)	1 299 579 291.4 (1.5) (3.0)
Wang [54]	1 299 648 954.54 (10)	-	-
Larkins [55]	1 299 648 690 (150)	1 299 610 830 (180)	1 299 578 990 (180)
Peik [57]	1 299 648 870 (600)	1 299 611 100 (600)	1 299 579 320 (600)

which is only a small fraction of their estimated uncertainty. Contrary, the results from Larkins and Hannaford show a systematic deviation of about 280 MHz which is nearly twice the reported uncertainty. Since a similar deviation of 277 MHz has also been observed in the $5s^2\ ^1\mathrm{S}_0 \rightarrow 5s5p\ ^3\mathrm{P}_0$ transition at 236.5 nm [42], it seems that the calibration of the monochromator was inaccurate. Taking this uncertainty into account, the rest-frame transition frequencies of the $F = 9/2 \rightarrow F = 9/2$ as well as of the $F = 9/2 \rightarrow F = 7/2$ transition are improved by nearly two orders of magnitude.

5.2.1 Discussion of the systematic uncertainty

Several contributions to the total systematic uncertainty of 3 MHz have been considered and are summarized in Tab. 5.3.

During the high-voltage measurements an angular deviation between the ions with velocity β and the laser beam caused the largest uncertainty. Again, an angle α leads to a shift of the resonant laser frequency f_L:

$$f_\mathrm{L} = f_0 \frac{1}{\gamma(1-\beta\cos(\alpha))} \,. \tag{5.2}$$

Using the iris diaphragms of the diagnostic stations to check the superposition and considering small drifts of the ion beam due to changes in the ion source, leads to an angular deviation of less than 1 mrad which is discussed in more detail in section 5.4.1. Assuming well-aligned laser beams since these can be superimposed more precisely in a longer distance, both resonance frequencies will be shifted nearly uniformly. This leads to a vanishing impact on the rest-frame transition frequency

$$f_0' = \sqrt{f_\mathrm{c}\gamma(1-\beta\cos(\alpha))}\sqrt{f_\mathrm{a}\gamma(1+\beta\cos(\alpha))} = \sqrt{f_\mathrm{c}f_\mathrm{a}} \cdot \sqrt{\frac{1-\beta^2\cos^2(\alpha)}{1-\beta^2}} \tag{5.3}$$

which experiences a shift of less than 1 kHz. Contrary, if one laser is well superimposed with the ion beam whereas the other laser is tilted, the uncertainty is maximal

$$f_0' = \sqrt{f_\mathrm{c}\gamma(1-\beta\cos(\alpha))}\sqrt{f_\mathrm{a}\gamma(1+\beta)} = \sqrt{f_\mathrm{c}f_\mathrm{a}} \cdot \sqrt{\frac{(1-\beta\cos(\alpha))(1+\beta)}{1-\beta^2}} \,. \tag{5.4}$$

The superposition of both laser beams was checked in a distance of 10 m. With an uncertainty in the adjustment of 1 mm at each position, this leads to a maximal angular deviation of 0.2 mrad and causes a

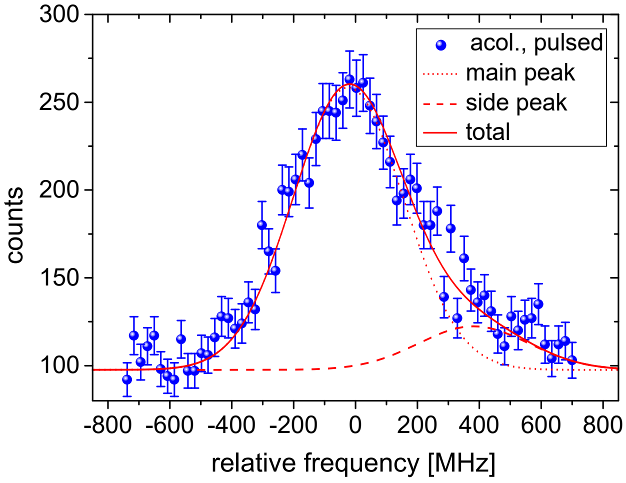

Figure 5.5: Asymmetric resonance spectrum caused by a partial overlap of laser and ion beam. Due to an energy separation in the 10° deflector, one edge is more pronounced. Considering these velocity classes with an additional side peak, a good agreement of the fit with the experimental data is achieved. The χ^2 is reduced from 1.40 in case of a symmetric fit function to 1.05 for the applied asymmetric function.

shift of 7 kHz in the determination of the rest-frame transition frequency.

Besides an angular deviation, a partial overlap of both beams can lead to systematic uncertainties due to an asymmetric resonance structure as already observed in Fig. 5.3. Since both laser beam diameters differ slightly, this asymmetry is differently distinct in both spectra and, hence, can cause different shifts when extracting the central frequency. To quantify this uncertainty, a series of collinear/anticollinear measurements was performed with a worsened overlap of both beams. The spectra were fitted with an asymmetric profile which takes an additional velocity class at the edge of the main resonance into account. An asymmetric resonance spectrum with the corresponding fit is shown in Fig. 5.5. Besides a higher statistical uncertainty (3.4 MHz), the center of the rest-frame transition frequency extracted from these measurements is shifted by 2.9 MHz compared to the results listed in Tab. 5.2. This shift is regarded as a worst-case scenario for deviations due to asymmetries caused by a partial overlap of ion and laser beams.

As discussed in section 2.2.7, the limited size of the laser beam can also lead to another systematic shift of the resonance frequency. The phase fronts of the real laser beam are distorted compared to the plane wave approach. Employing Eq. 2.36 to estimate its impact for a laser beam with a beam waist of 1 mm, which has an angle of 1 mrad relative to the ion beam and an offset of 0.2 mm, leads to a shift of up to 5 kHz, depending on the position of the interaction relative to the focal point. Since two independent lasers are used, this shift has to be considered twice.

Further systematic contributions can be identified when analyzing Eq. 5.1. The uncertainty of the determination of ΔU_{scan} which was smaller than 8 V during all measurements, is of the order of 0.1 mV due to the uncertainty in the scan-voltage amplification factor of about $1 \cdot 10^{-5}$ (compare appendix B). The resulting deviation in the rest-frame transition frequency determination is 1 kHz. The frequency shift $\Delta f_{\text{recoil}} = 33$ kHz for one laser-ion interaction is considered in the evaluation of the rest-frame transition frequency even though it is much less than our statistical uncertainty. To extract the impact of multiple excitations, the simulations done for Ca^+ have been extrapolated. This yields a fraction of below 0.1 % of In^+ ions that is excited twice. Due to the small recoil shift of 33 kHz, it causes a sub-kHz contribution to the rest-frame transition frequency determination. Since the transition frequency for circularly-polarized light is shifted due to the Zeeman effect, its fraction in the laser light was measured to be 0.5 % with a Glan-Taylor polarizer directly in front of the beamline. Due to this small fraction and the magnetic shielding, its impact is estimated to be less than 1 kHz.

The frequency of the AOM was measured with an accuracy better than 1 kHz to be 199.998 11 MHz. Systematic uncertainties arising from the measuring principle with one pulsed and one continuous laser beam were investigated by measuring the $5s^2\ {}^1\text{S}_0\ \text{F}{=}9/2 \rightarrow 5s5p\ {}^3\text{P}_1\ F = 11/2$ transition two weeks later again with both lasers operated in pulsed mode. The result of 1 299 648 956. 8 (3.1) (2.9) MHz is within the statistical uncertainties of both measurements and does not give any hint of a systematic effect due to the measuring principle.

Table 5.3: Systematic uncertainties in the determination of the $5s^2\ ^1\mathrm{S}_0 \rightarrow 5s5p\ ^3\mathrm{P}_1$ rest-frame transition frequencies of $^{115}\mathrm{In}^+$. Asymmetries in the 500-MHz broad resonance caused by a partial overlap of laser and ion beam can lead to significant deviations. The other systematic contributions are well under control enabling high-precision experiments on narrow-linewidth transitions.

Systematic effect	Contribution
Overlap of laser and ion beam	2.9 MHz
Angular deviation of laser beams	7 kHz
Angular deviation of ion beam	< 1 kHz
Phase front distortion	10 kHz
Scan voltage	1 kHz
Multiple photon recoil	< 1kHz
Zeeman effect	< 1kHz
AOM frequency	< 1 kHz

Due to the stabilization directly on the frequency comb, no systematic deviations in the determination of the laser frequencies are expected. The scatter due to the stabilization scheme is included in the statistical uncertainty.

Summing all contributions yields a total systematic uncertainty of approximately 3 MHz almost exclusively caused by the asymmetric lineshape due to a possible partial overlap of both beams. This demonstrates the capability of this setup for high-precision experiments if an ion beam with narrow energy width is available. In this case, there is almost no energy separation in the 10° deflector leading to much smaller asymmetry contributions as shown in measurements on Ba^+ [35]. A new multi-purpose ion source based on laser ablation and cooling with helium gas is under construction [93] to fully exploit this in the future.

Adding statistical and systematic uncertainties in quadrature, the total uncertainty of the rest-frame transition frequencies is about 3.3 MHz. This would lead to an uncertainty of 4 ppm in the high-voltage evaluation if not the $5s^2\ ^1\mathrm{S}_0\,\mathrm{F}{=}9/2 \rightarrow 5s5p\ ^3\mathrm{P}_1\, F = 11/2$ transition is used for the pump-and-probe measurements. By optical pumping it is possible to increase the precision of the individual measurements significantly. While using the narrow feature of the optical pumping in collinear/anticollinear measurements could in principle improve the accuracy of the transition frequency, the background in the collinear measurements and the small signal amplitude do not allow for such measurements as discussed in section 5.3.2.

5.3 Optical pumping in In$^+$

Since only the $5s^2\ ^1\mathrm{S}_0\,\mathrm{F}{=}9/2 \rightarrow 5s5p\ ^3\mathrm{P}_1\, F = 11/2$ transition is known with sufficient accuracy, it is favored for performing laser-based high-voltage measurements. Furthermore, the application of $\Delta m = 0$ transitions using linearly-polarized light has the advantage of minimizing Zeeman shifts. Optical pumping under these conditions is still possible since the transition strength between the magnetic substates varies as already discussed in section 2.3.2. The relative transition strength based on the squares of the Clebsch-Gordan coefficients is depicted in Fig. 5.6 for all three hyperfine transitions.

During ion production, all magnetic substates are populated equally. After excitation to the $F = 11/2$ level, the decay into states with small absolute magnetic quantum number m_F is favored. Hence, these substates are stronger populated after optical pumping. Since these states have a higher transition strength for an excitation with linearly-polarized light, the signal observed during the probing process is enhanced when interacting with the optically-pumped velocity class. The expected additional peak on top of the main resonance was verified in the experiment and is shown in Fig. 5.7a.

To investigate the pumping scheme further, the transition to the $F = 9/2$ and to the $F = 7/2$ states have been measured. Furthermore, circularly-polarized light has been used in the latter case as well. In Fig. 5.7b the ions were excited to the $F = 9/2$ state with linearly-polarized light causing a dip in the spectrum. Looking at the transition rates, this also matches the expectation. The central magnetic substates which are populated during optical pumping, have a low excitation rate leading to this spectral feature. In case of an excitation to the $F = 7/2$ state (Fig. 5.7c), the outer magnetic substates are preferably populated which are 'dark' states in the probing process.

More important than the absolute number of optically-pumped ions which also depends on the different transition strength to the three hyperfine levels, is the contrast between the spectral feature and the main resonance. Quantifying the experimentally obtained contrast defined as the ratio of height/depth of the feature to the total signal intensity without background and comparing it to theoretical expectations, yields a good agreement as shown in Fig. 5.8. For reasons of better comparison, the contrast was normalized to the $5s^2\,{}^1\mathrm{S}_0\,\mathrm{F}{=}9/2 \rightarrow 5s5p\,{}^3\mathrm{P}_1\,F = 11/2$ which will be taken for the high-voltage evaluation. The theoretical values are calculated by using the transition rates shown in Fig. 5.6 and allowing one laser-ion interaction during optical pumping. First, the relative amount of excited ions per substate is identified which depends on the corresponding transition strength. After the subsequent decay, the ground state population distribution is changed. Calculating the sum of all excited ions with these starting conditions and comparing it to an equally distributed population, yields the theoretically expected contrast.

During this measurement the absolute contrast when exciting the ions with 1 mW of linearly-polarized laser light to the $F = 11/2$ state, was 2.8 % which is also a typical value for the later experiments. The absolute values of the other transitions can be found in Tab. 5.4. The highest contrast is achieved by exciting the ions to the $F = 7/2$ state. Compared to the $F = 9/2 \rightarrow F = 11/2$ transition, it is increased by a factor 2.4 in case of circularly-polarized light. With linearly-polarized light a factor 1.8 is gained.

Calculating the contrast for the case that the ions are excited to the $F = 11/2$ state in the pumping process but are probed on the $F = 7/2$ transition with circularly-polarized light, yields a relative contrast of 1.45. This demonstrates that the conventional approach discussed in section 2.3.2 would not lead to large benefits and is even outperformed by using the $F = 7/2$ transition for pumping and probing.

The theoretical calculation did not consider multiple excitations. But since it yields a higher contrast even for up to one excitation, this can been seen as a good approximation. Contrary, it can even be used to estimate the amount of ions interacting during optical pumping. In case of magnetic substates with the highest transition strength, this yields a rate of about 50 % whereas the mean rate is at 35 %. This estimate is confirmed when comparing it with a rough calculation based on the experience from the measurements with Ca^+. There, about 18 interactions took place in IR1 but the scattering rate was about 300 times larger. Since the laser intensity is a factor of two higher in case of In^+, one would expect a fraction of 12 % of the ions to be excited once. When taking the much better ion beam profile into account, both estimates are in good agreement.

5.3.1 Linewidth and shape

Even though the optical pumping scheme agrees well with the expectations, the width of the spectral feature of $\Gamma_{\mathrm{exp}} = 14\,\mathrm{MHz}$ is much larger than expected from the (power-broadened) natural linewidth. A likely reason for this large linewidth is transit-time broadening (compare section 2.4.3) due to the limited length of $l = 25\,\mathrm{cm}$ of the second interaction region. Roughly estimating its impact by $\Gamma_{\mathrm{tof}} \approx v/l \approx 1\,\mathrm{MHz}$ demonstrates already that it has a larger contribution to the resulting shape than the natural linewidth. Due to the rectangular on/off resonance condition when the ions enter/leave the interaction region, the intensity distribution of the resonance is given by [59]

$$I(f) = C\,\frac{\sin^2(\pi(f - f_0)T)}{(f - f_0)^2}\,. \tag{5.5}$$

Table 5.4: Contrast between the spectral feature and the main resonance for the different $5s^2\,{}^1\mathrm{S}_0 \rightarrow 5s5p\,{}^3\mathrm{P}_1$ hyperfine transitions. In the experiment the same laser was used for pumping and probing. Taking the transition strength values given in Fig. 5.6, a theoretical value was calculated assuming a single excitation in the pumping process. Both values were normalized to the $F = 9/2 \rightarrow F = 11/2$ transition with linearly-polarized light. Additionally, a pumping scheme where the $F = 9/2 \rightarrow F = 11/2$ transition is used for pumping and the $F = 9/2 \rightarrow F = 7/2$ transition for probing was evaluated theoretically (mixed). The results are plotted in Fig. 5.8.

Transition	Laser polarization	Exp. absolute	Exp. normalized	Theory
$F = 9/2 \rightarrow F = 11/2$	linear	2.75 (0.18) %	1.0 (0.07)	1.0
$F = 9/2 \rightarrow F = 11/2$	circular	-	-	1.71
$F = 9/2 \rightarrow F = 9/2$	linear	2.68 (0.27) %	0.97 (0.10)	1.09
$F = 9/2 \rightarrow F = 9/2$	circular	-	-	0.97
$F = 9/2 \rightarrow F = 7/2$	linear	5.41 (0.24) %	1.97 (0.09)	1.82
$F = 9/2 \rightarrow F = 7/2$	circular	6.69 (0.30) %	2.43 (0.11)	2.36
mixed	circular	-	-	1.45

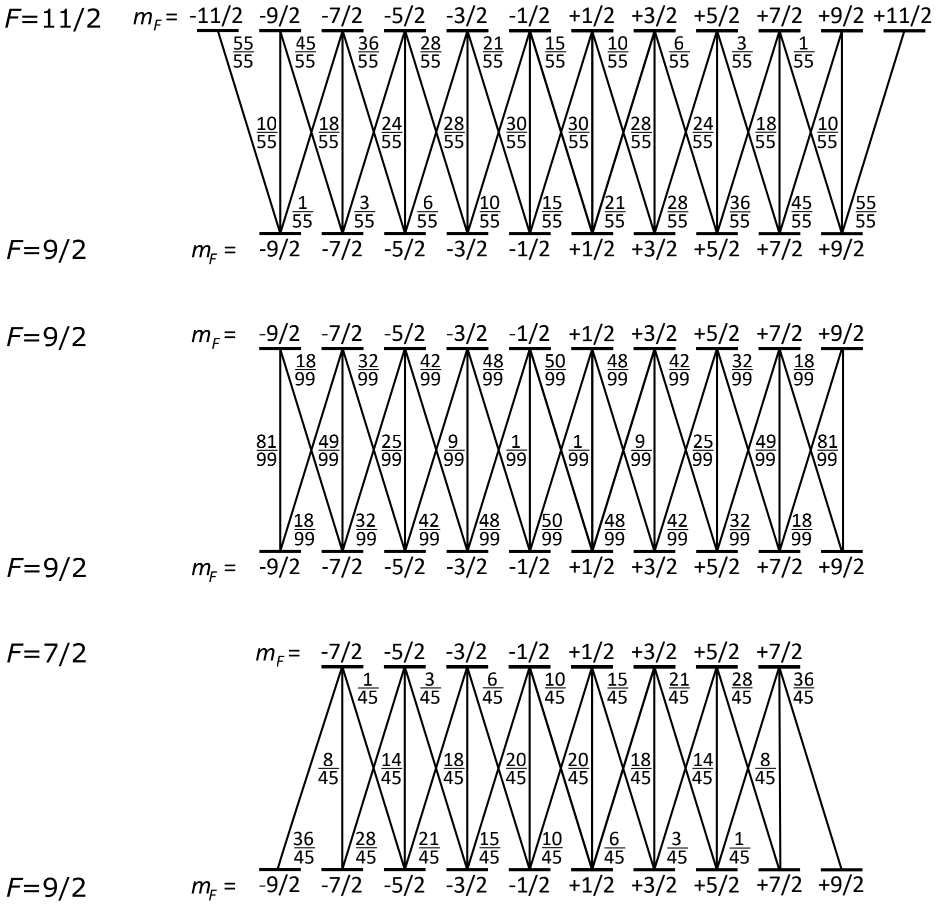

Figure 5.6: Quadratic Clebsch-Gordan coefficients for the different ${}^1\mathrm{S}_0 \rightarrow {}^3\mathrm{P}_1$ hyperfine transitions in In^+. These have been used for determining the contrast between the spectral feature and the main resonance theoretically as depicted in Fig. 5.8 and listed in Tab. 5.4. The values have been calculated with the Clebsch-Gordan function implemented in Wolfram Mathematica.

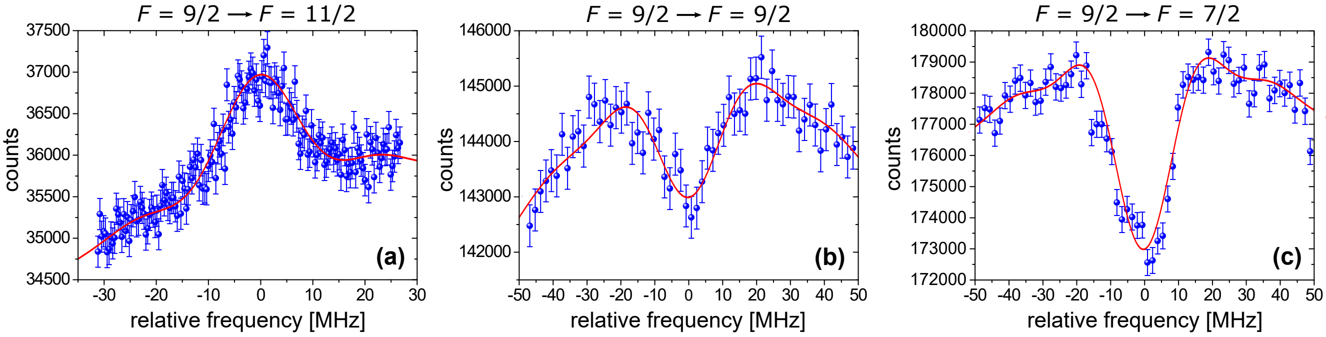

Figure 5.7: Spectral features generated by optically pumping the different $5s^2\,{}^1\mathrm{S}_0 \rightarrow 5s5p\,{}^3\mathrm{P}_1$ hyperfine transitions with linearly-polarized light. Due to the varying transition strength between the magnetic substates, an additional peak on top of the main resonance is generated when pumping and probing the $F = 9/2 \rightarrow F = 11/2$ transition (a). In case of the $F = 9/2 \rightarrow F = 9/2$ (b) and the $F = 9/2 \rightarrow F = 7/2$ transition (c), a dip appears when probing the optically-pumped velocity class. The contrast of the feature is defined as the ratio of height/depth of the feature to the total signal intensity without background. The observed width of the spectral feature is in all cases about 14 MHz. The fit (red line) is a $\sin^2(x)/x^2$ function (transit-time broadening) superimposed with a Voigtian. Its linewidth parameters are taken from the resonance without optical pumping. The resonance frequency can be extracted with an uncertainty of about 400 kHz.

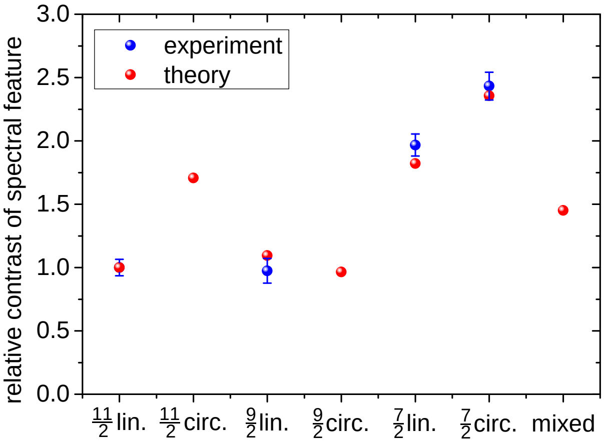

Figure 5.8: Contrast between the spectral feature and the main resonance for the different $5s^2\,{}^1\mathrm{S}_0 \rightarrow 5s5p\,{}^3\mathrm{P}_1$ hyperfine transitions measured with a single laser for pumping and probing. The contrasts determined in the experiment agree well with theoretical predictions based on the transition strength provided in Fig. 5.6 and one laser-ion interaction. The highest contrast is achieved when using the $F = 9/2 \rightarrow F = 7/2$ transition. It is even higher than in a mixed approach where the $F = 9/2 \rightarrow F = 11/2$ transition is used for pumping and the $F = 9/2 \rightarrow F = 7/2$ transition for probing which was evaluated only theoretically.

When integrating over all emitted fluorescence photons the FWHM results in

$$\Gamma_{\mathrm{tof}} = \frac{5.6}{2\pi T} = \frac{5.6}{2\pi}\frac{\upsilon}{l} . \tag{5.6}$$

However, due to the long lifetime ($\tau = 440\,\mathrm{ns}$) of the excited state which is of the order of the time of flight through the interaction region ($\upsilon = 15.87\,\mathrm{cm}/\mu\mathrm{s}$), only a part of the photons can be collected. The largest contribution to the total count rate is generated by the ions excited right at the beginning of the interaction region. There, the transit-time broadening is highest. Contrary, the ions excited at the end of the interaction region will most probably emit the fluorescence photons after they left the interaction region. This leads to a larger broadening than expected from Eq. 5.6. To get a more realistic estimate for the transit-time broadening, an effective length l_{eff} is defined in the following:
The amount of detected photons emitted by ions excited at the position x in the optical detection region with length $l = 25\,\mathrm{cm}$ is given by

$$N = N_0\left(1 - e^{-\frac{l-x}{\tau\upsilon}}\right) \tag{5.7}$$

whereof the normalization constant is chosen to be $N_0 = 1$. The mean amount of detected photons $\overline{N}$ can be calculated as

$$\overline{N} = \frac{1}{l}\int_0^l \left(1 - e^{-\frac{l-x}{\tau\upsilon}}\right) dx = 1 + \frac{\tau\upsilon}{l}\left(e^{-\frac{l}{\tau\upsilon}} - 1\right) . \tag{5.8}$$

Using this to determine the effective length yields

$$l_{\mathrm{eff}} = -\tau\upsilon \ln(1 - \overline{N}) = -\tau\upsilon \ln\left(\frac{\tau\upsilon}{l}\left(1 - e^{-\frac{l}{\tau\upsilon}}\right)\right) = 9.1\,\mathrm{cm} . \tag{5.9}$$

This yields a linewidth of $\Gamma_{\mathrm{tof}} = 1.6\,\mathrm{MHz}$ for a 15-keV ion beam and 2.1 MHz in case of a post-acceleration by 20 kV. To consider additional power broadening, the saturation intensity is adapted to this linewidth

$$I_{\mathrm{sat}} = \frac{\pi h c}{3\lambda_0^3} \cdot 2\pi\Gamma_{\mathrm{tof}} \tag{5.10}$$

yielding a total width of the probing transition of $\Gamma_{\mathrm{tof,S}}(15\,\mathrm{keV}) = 3.2\,\mathrm{MHz}$ for a 1 mW laser beam with a size of $2\,\mathrm{mm}^2$. Since the magnetic field is shielded and the laser fluctuations are reduced with the new stabilization scheme, additional contributions of only 500 kHz are expected, mainly due to noise on the voltage applied to IR2. Calculating the convolution with the optically-pumped velocity class by applying the simulation described in appendix A, yields a total linewidth of 4.2 MHz which is still a factor 3.5 smaller than observed in the experiment.
To investigate the trend of simulation and experiment, measurements with different laser powers were taken. Additionally, the ions were probed in the drift tube in front of the optical detection region. In this case, Eq. 5.6 was applied to calculate the transit-time broadening. In Fig. 5.9 the normalized results are shown. The trend of the experimental data can be well reproduced although the theoretical assumptions are underestimated by the discussed factor of 3.5. A reason for this could be contact potentials between both parts of the optical detection chamber and field penetrations. These decrease the time in resonance of the ions and hence, increase the broadening contributions. For this reason, only the first chamber of the optical detection unit will be used for the high-voltage evaluation since field penetrations can only be surly excluded in this case.

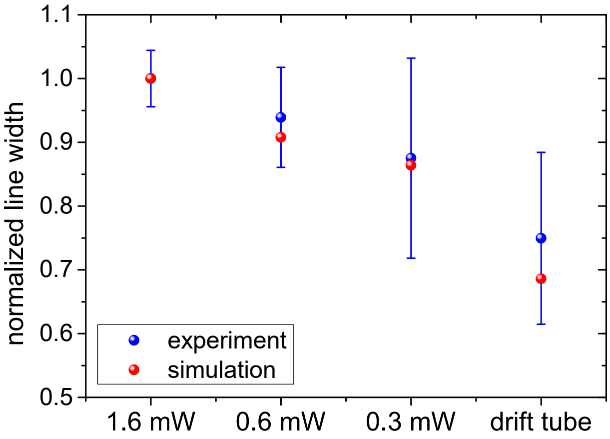

Figure 5.9: Comparison of the experimentally and theoretically determined dependency of the linewidth on transit-time and power broadening. The former was realized by using the drift tube for probing which has a nearly two times larger effective length. There, the laser power was 1.4 mW. The trend is in good agreement whereas the experimental value is a factor 3.5 larger than predicted. See text for more details.

5.3.2 Approaches for linewidth reduction

As discussed above, transit-time and power broadening are the largest contributions of the resulting linewidth. Its reduction could drastically increase the sensitivity $\kappa \cdot \Gamma$ of the high-voltage measurements. The power broadening can be reduced by using less laser power. However, since the typical laser powers are already far above the saturation intensity, they have to be drastically reduced to gain a significantly narrower linewidth. As shown in Fig. 5.9, a reduction from 1.6 mW to 0.3 mW yielded a width reduction of about 15 % with a drastically increased statistical uncertainty.

Reducing the transit-time broadening is more challenging. Using the drift tube for laser ion-interaction is one possibility. Since its effective length is about a factor 1.9 larger than the effective length of the optical detection region, this should lead to a reduction by 30 %. However, the signal rate drops to 14 % whereas the background level stays constant which also causes a much larger statistical uncertainty.

Using the AOM for background-free measurements is not feasible since the spectral feature is on top of the main resonance and has a contrast of only 3 %. To outreach the statistical scatter of the underlying main resonance in this mode would take more than one hour of accumulation time for typical conditions. This is not applicable since the high-voltage measurements have to be performed faster to resolve voltage drifts. For the same reason, it was not possible to perform absolute rest-frame transition frequency measurements on optically-pumped ions.

Another option to reduce the transit-time broadening is the extension of the interaction region which can be basically realized by using the drift tube in addition. However, the potential has to be constant over the whole distance. Since about 1 V of contact potential was measured when comparing IR1 and IR2 (see section 4.3.1), a similar potential difference is expected in this case since the drift tube is made of the same material as IR1. This would result in a deviation of the resonant frequency of 23 MHz. Due to this large discrepancy, measurements with shortened electrodes showed no reduction of the linewidth. Since Doppler tuning is performed meaning the voltage of IR2 is scanned, no additional voltage supply could be used easily to vary the potential of the drift tube relative to IR2.

For these reasons, it seemed most promising to perform high-voltage measurements in the optical detection region with cw lasers at a laser power of 0.75 mW and 0.5 mW for pumping and probing, respectively. This corresponds to the maximal power available, after beam shaping with the spatial filter (30 % transmission), the superposition of both laser beams with an UV-beam splitter (40 % transmission) and transport (90 % reflectivity at each mirror).

5.3.3 Systematic effects during optical pumping

During the investigation of the optically pumping process in Ca^+, a significant impact on the lineshape was observed if the center of the pumping position deviated from the center of the artificially broadened velocity distribution. In case of In^+, the ion source potential is not modulated since the underlying resonance structure is already several eV broad due to the production mechanism described in section 3.2. The measurements depicted in Fig. 5.4 showed a (nearly) Gaussian distribution with a width of about $\Gamma_{\mathrm{FWHM}} \approx 500\,\mathrm{MHz}$ (22 V) which confirms the expectations.

For optical pumping, the potential of IR1 is chosen in a way that the ions of the central velocity class are in resonance. The consequences of an offset from the central position are estimated with the simulation described in appendix A. It turned out that the systematic shift due to an asymmetry of the optically-pumped velocity class is less than 10 kHz even for a worst case scenario of a 10 MHz broad lineshape of the pumping transition which is 100 MHz off-center. The impact on the high-voltage measurement can therefore be neglected. Not considered in this simulation is the extraction of the resonance frequency of the additional peak on top of the main resonance. This is covered within the statistical uncertainty of the fit routine.

5.4 High-voltage measurements

To demonstrate laser-based high-voltage measurements with a 15-keV In^+ ion beam, a post-acceleration voltage of only −1 kV was chosen. The reason was the alignment issue of the post-acceleration electrodes explained in section 4.1.1. With a small acceleration potential, the influence on the ion beam direction and the accompanying systematic uncertainty stays small. Furthermore, the divergence of the ion beam is hardly affected. This is important since the limited measuring period did not allow for the time-intense optimization procedure explained in section 4.3.2. Instead both einzel lenses were grounded. They still have an influence on the ion beam collimation because the outer electrodes are (nearly) on the potential of IR1 and IR2, respectively. Extrapolating the optimal einzel lens potentials determined during the Ca^+ measurements (see Tab. 4.4), confirms that the optimal potentials for a post-acceleration of −1 kV are expected to be rather low. The disadvantage of the small post-acceleration voltage is that voltage-independent uncertainties like, e.g., the statistical uncertainty, have a larger contribution to the combined relative uncertainty of the high-voltage evaluation.

The $F = 9/2 \rightarrow F = 11/2$ transition has been used to perform laser-based high-voltage measurements in the reference-measurement approach. Since the same transition is used for pumping and probing, the reference measurement could be realized with one laser system. The second laser, required to probe the post-accelerated ions, was blocked during the reference measurements to improve the signal-to-noise ratio. Hence, the reference measurements could be realized in about 10 min each whereas it took 20 min for a high-voltage measurement. A typical spectrum is shown in Fig. 5.7a and the operational conditions are summarized in appendix C. The laser frequencies have been chosen in a way that the resonant scan voltages in reference and high-voltage measurements differ by less than 1 V which basically eliminates its systematic contribution.

During one day, seven reference measurements with typically three corresponding high-voltage measurements were taken as indicated in Fig. 5.10 by the small dotted lines. After the second and the fifth run it was made sure that optical pumping is performed at the central velocity class. The laser-based measurements were compared to electronic measurements with the high-voltage divider HVA100. These were taken directly before each measurement. The statistical uncertainty of the first individual measurements is ± 30 ppm (30 mV / 650 kHz) and is composed of the uncertainties in the determination of the resonance frequencies of high-voltage and reference measurements. The complex lineshape on top of a Voigt profile requires more degrees of freedom and the lower signal-to-noise ratio limits the accuracy to 400 kHz - 500 kHz which corresponds to 3 % of the FWHM of the spectral feature generated through optical pumping. For normal Voigt-like spectra as shown in Fig. 5.4 or in Fig. 4.7, the resonance frequency could be identified with a precision better than 1 %. It is also visible that the statistical uncertainty increased during the measurement time mainly due to decreasing laser power.

Taking the weighted average over all measurements, the deviation to the electronic measurement is 4.5 ppm. The statistical uncertainty of ± 8.2 ppm corresponds to the standard deviation of the mean which is slightly larger than the uncertainty of the weighted average (7.8 ppm). This corresponds to a

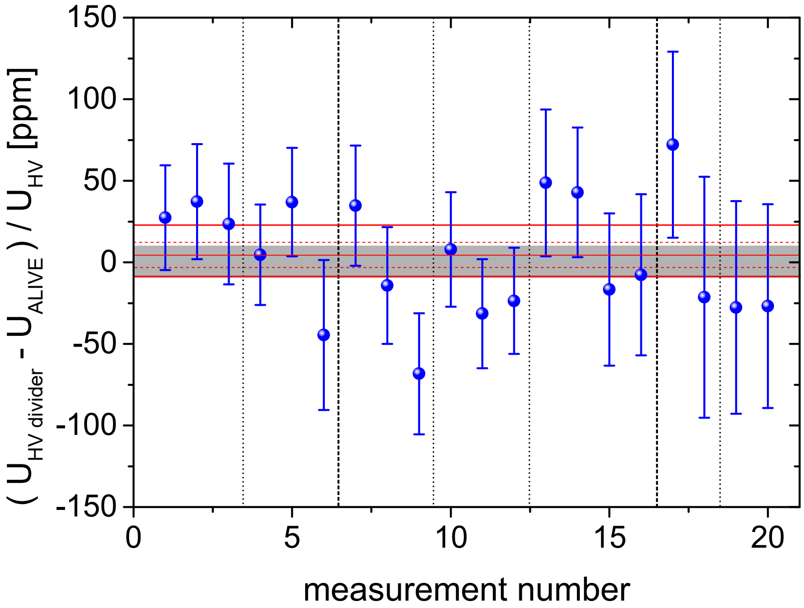

Figure 5.10: Comparison of electronic and laser-based high-voltage measurements with In^+. The gray area corresponds to the 10-ppm uncertainty of the electronic measurement for the post-acceleration voltage of −1 kV. In blue, 20 individual laser-based high-voltage measurements and their corresponding statistical uncertainty are depicted which were separated in seven runs. Taking the weighted average, the laser-based approach deviates by 4.5 ppm from the central value of the conventional measurement. The statistical uncertainty of 8.2 ppm (red dashed lines) fully covers this discrepancy. Taking the systematic contributions listed in Tab. 5.5 into account, results in the asymmetric total uncertainty interval indicated by the solid red lines.

very good agreement of both methods since the electronic measurement has a relative uncertainty of 10 ppm itself. It is larger for lower voltages since the voltage-independent offset voltage of the divider which was measured to be 1.5(3) µV, causes an uncertainty of 3 mV (3 ppm). For higher post-acceleration voltages it scales down and usually can be neglected. Additionally, voltage drifts of 2 ppm which were observed between two electronic measurements, are taken into account.

5.4.1 Discussion of the uncertainty

As shown in Fig. 5.10, the statistical uncertainty could be reduced to 8.2 ppm (8.2 mV / 180 kHz) by averaging over all individual measurements. Besides this, several systematic effects have to be taken into account which are listed in Tab. 5.5. An asymmetry of the main resonance does not contribute in this case since only the small fraction of the main peak is fitted as a baseline for the additional fit that extracts the resonant frequency of the spectral feature generated through optical pumping.
Contrary to the rest-frame transition frequency determination, angular deviations between laser and ion beam cause large systematic deviations. The superposition of both beams has an uncertainty of 1 mm at each diagnostic station which are 2.6 m apart, yielding a contribution of $\alpha_s = 0.8$ mrad. Due to the small and distinct ion beam shape, an even higher precision is possible. But since small drifts of the ion beam due to changes in the ion source have been observed, this larger uncertainty is taken to cover these effects. During the post-acceleration by 1 keV, shifts of the ion beam of 0.5 mm have been observed at the phosphor screen at DK3 which is installed in a distance of 80 cm. This leads to an additional contribution of $\alpha_i = 0.6$ mrad causing a total angular uncertainty of 1 mrad for the post-accelerated beam. As discussed in section 4.1.1, the contributions occurring in reference and high-voltage measurements will

Table 5.5: Statistical and systematic uncertainties considered in the laser-based high-voltage evaluation with In^+ ions. In case of directed contributions, this is indicated with (+) and (−) signs. A detailed discussion of each uncertainty contribution can be found in the referenced section.

	$-1\,\mathrm{kV}$	discussion
δU_{stat}	$8.2\,\mathrm{mV}$	5.4
$\delta U_{\mathrm{stat}}/U_{\mathrm{HV}}$	$8.2\,\mathrm{ppm}$	
$\delta U_{\mathrm{angle}}$	$-6.4\,\mathrm{mV}$	5.4.1
δU_{div}	$\pm 10\,\mathrm{mV}$	5.4.1
δU_{asy}	$\pm 0.02\,\mathrm{mV}$	5.3.3
$\delta U_{\mathrm{Gauss}}$	$\pm 0.5\,\mathrm{mV}$	5.2.1
$\delta U_{\mathrm{penetration}}$	$-0.1\,\mathrm{mV}$	2.2.12
$\delta U_{\mathrm{charge}}$	$+0.03\,\mathrm{mV}$	2.2.13
δU_{scan}	$\pm 0.01\,\mathrm{mV}$	5.4
δU_{f_0}	$\pm 0.14\,\mathrm{mV}$	2.2
δU_{sys}	${}^{+10.7}_{-16.7}\,\mathrm{mV}$	
$\delta U_{\mathrm{sys}}/U_{\mathrm{HV}}$	${}^{+10.7}_{-17.2}\,\mathrm{ppm}$	
$\delta U_{\mathrm{total}}/U_{\mathrm{HV}}$	${}^{+13.5}_{-19.1}\,\mathrm{ppm}$	

partly cancel, leading to a total uncertainty of 6.4 ppm. Since the deviation is larger in the high-voltage measurement, it shifts the laser-based results to less negative values, leading to a corresponding one-sided uncertainty which is indicated in Tab. 5.5 by the (−) sign.

The uncertainty δU_{div} caused by the beam divergence was taken from the Ca^+ measurements (see section 4.3.2) since there was not sufficient time to apply the optimization procedure. This can be seen as an upper limit since the ion beam properties in general are much better in this case due to the advantages of the LMIS ion source.

The asymmetry contribution due to optical pumping off-center is much smaller compared to the measurements with Ca^+ as explained in section 5.3.3. On the contrary, phase front distortions of the laser beams have a higher impact since two independent lasers are used for the high-voltage and the reference measurement. As discussed in section 5.2.1, this can cause a deviation of 10 kHz corresponding to 0.5 ppm. References to the discussion of further contributions are provided in Tab. 5.5.

Adding the total systematic uncertainty of $+10.7\,\mathrm{ppm}/-17.2\,\mathrm{ppm}$ and the statistical uncertainty of $\pm 8.2\,\mathrm{ppm}$ quadratically, leads to a total relative uncertainty of 19 ppm. This fully covers the observed deviation of 4.5 ppm relative to the electronic measurement which has an uncertainty of 10 ppm itself. Since the largest but voltage-independent contributions δU_{stat} and δU_{div} contribute less for higher post-acceleration voltages, it is possible to target the ppm-level in case of well aligned electrodes in the post-acceleration section. Further improvements can be achieved by increasing the length of the optical detection region which would reduce the linewidth of the spectral feature and hence, decrease the uncertainty in the determination of the resonance frequency. Additionally, the high-voltage evaluation with In^+ can benefit from the doubled contrast when using the $F = 9/2 \rightarrow F = 7/2$ transition which is planned to be measured in an ion trap [58].

6 Summary and outlook

Based on the ideas of Poulsen [16, 18] and the experiences from Götte [19, 50] and Will [22, 51], an improved approach for laser-based high-voltage measurements was developed and a dedicated setup designed, constructed and commissioned within this work. During this process several systematic contributions were investigated and either eliminated or at least considerably reduced.
During the measurements with Ca^+, the angular alignment of the ion and laser beam and the ion beam collimation have been identified as the largest systematic contributions. The latter could be drastically decreased with an optimization procedure based on the $\cos\alpha$ dependency of the Doppler effect. It was demonstrated that the systematic uncertainty of this contribution can be reduced below 1 ppm for well-aligned ion and laser beams. The statistical uncertainty in the first measurement campaign was slightly above the ppm level. By establishing a new stabilization scheme of both laser systems and by changing from the 23-MHz broad transition in Ca^+ to the narrow 360-kHz transition in In^+, a significant gain was expected. It turned out that large transit-time broadening and the smaller count rate due to the low scattering rate, lead only to small enhancements. Further improvements with In^+ ions are still possible by using the $5s^2\,{}^1\mathrm{S}_0\,F = 9/2 \rightarrow 5s5p\,{}^3\mathrm{P}_1\,F = 7/2$ transition instead, for which the contrast of the narrow optical pumping feature will be raised by a factor of two and by increasing the length of the optical detection region to reduce the transit-time broadening. The statistics could be potentially improved if stable operation of the ion source can be established at considerably higher beam currents of about 100 nA.
Finally, high-voltage measurements between −1 kV and −20 kV at the 5-ppm level were achieved with Ca^+ and In^+ ions, representing a 20-fold improvement compared to all previous attempts with this technique. Moreover, the potential to increase the accuracy into the sub-ppm regime was demonstrated. Since this approach is based on a frequency measurement, it is suited to become a quantum standard for high-voltage measurements.

In the next step, the high-voltage measurements with Ca^+ ions will be repeated under improved conditions. The new laser stabilization established for the indium work will significantly reduce the statistical uncertainty. Due to the improvements in the background reduction, it will become possible to use less laser power and to decrease the resulting linewidth by up to a factor of two. Besides the statistical uncertainty, also the systematic uncertainty due to the ion beam divergence will profit from this higher resolution since the ion beam can be collimated more precisely in the optimization procedure.
Compared to the first run, the time required for an individual measurement can be reduced with higher ion currents. Therefore, the graphite crucible will be replaced by a mono-crystalline tungsten furnace which has a larger work function of up to 5.4 eV [94]. This would increase the ionization efficiency by about two orders of magnitude. In this case, one could easily afford a larger modulation of the source potential to also avoid asymmetries during optical pumping. Furthermore, this would allow us to improve the ion-beam emittance by selecting the central beam with the adjustable aperture and to establish the superposition with the laser beam more precisely. Since the ion getter pumps have been removed and the earth magnetic field shielded, a deflection of the ion beam due to magnetic fields is precluded. A particular important aspect has been the improvement of the post-acceleration electrode alignment because even a slight mismatch of 1 mm influenced the ion beam drastically. In the new arrangement that is shown in Fig. 6.1, all electrodes are connected via an insulator providing a more rigid construction. The ensemble is fixed to the outer chamber at four positions and additionally stabilized by three rods. In contrast to the conditions during the In^+ measurements, no deflections were observed on the phosphor screen even for a post-acceleration voltage of −20 kV. It is expected that the systematic uncertainty due to the angular alignment can be reduced below the ppm level. This will additionally decrease secondary

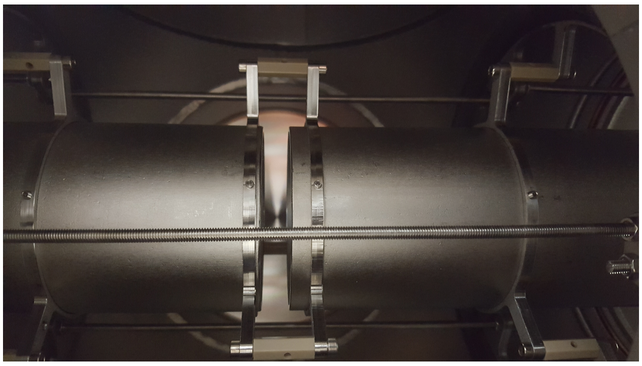

Figure 6.1: Optimized arrangement of the post-acceleration stage. All electrodes are connected via insulators to avoid the displacements which originated in the former individual mounting. First measurements demonstrated a significantly reduced impact on the ion beam trajectory even for high post-acceleration voltages. Further improvement of the adjustment can be achieved with rigid sleeves. However, this would limit the vacuum pumping efficiency.

uncertainties, e.g., caused by the phase front distortion of the laser beam and will potentially enable high-voltage measurements in the sub-ppm regime.

Besides the improvements in the experimental setup, other ion species offer the possibility to increase the accuracy of the laser-based high-voltage evaluation. $^7\mathrm{Li}^{+*}$ and $^9\mathrm{Be}^+$ offer a higher sensitivity $\kappa \cdot \Gamma_0$ for high-voltage measurements compared to Ca^+. This can further increase the accuracy of ALIVE since similar frequency uncertainties will correspond to smaller voltage deviations. However, there is the risk of transit-time broadening for these very light elements, especially in case of large post-acceleration voltages. Additionally, they are more sensitive to the photon recoil and require a similar complex laser system as was used for the In^+ measurements. On the other hand, $^{171}\mathrm{Yb}^+$ is much heavier and can be optically pumped and probed with frequency-doubled Ti:Sa lasers but still offers an increase in sensitivity. Furthermore, it should be possible to use the LMIS ion source for generating a beam based on an Yb alloy with low melting point.

Due to their larger response to an electrostatic acceleration, highly charged ions are also an alternative to increase the sensitivity. The production can be realized, e.g., with an electron beam ion source (EBIS). To demonstrate its feasibility for the production of suitable candidates, the HITRAP EBIS at GSI [95, 96] which was formerly limited to the production of gaseous elements, was upgraded within [97] allowing the production of an ion beam of basically every element for which a compound with a high vapor pressure exists (e.g. organometalics).

With these improvements it should be possible to target the sub-ppm level for laser-based high-voltage measurements. This opens the possibility for the definition of a quantum standard for high-voltage determinations which will be a great benefit for metrology and science since this is not achievable with the conventional technique. Systematic uncertainties in the complex calibration procedure of high-voltage dividers, their susceptibilities to changes of ambient conditions and the inner structure of the resistors that are causing slow changes of the divider ratio, do not allow to improve accuracy beyond the 1-ppm level. One of the world's most precise high-voltage dividers is at the KATRIN experiment in Karlsruhe [13] where an accurate high-voltage measurement at −18.6 kV is desired for the determination of the neutrino mass. This divider was calibrated to the difference of conversion electron lines of $^{83m}\mathrm{Kr}$ at the KATRIN MAC-E-Filter [27] with an uncertainty in the ppm regime which is confirmed by the comparison to the PTB dividers. In the next step, this divider will be installed at ALIVE to compare it to the laser-based measurements. On the long-term and with higher accuracies at ALIVE, these calibrations can lift the accuracy of the divider and hence, the precision of the KATRIN experiment.

Besides this, the experimental setup is dedicated for high-precision collinear laser spectroscopy experiments. As demonstrated in the absolute frequency determination of In^+ and Ba^+ [35], the systematic uncertainties can be reduced to some ten kHz if an appropriate ion beam is available. This is a similar level of accuracy as achieved in modern ion trap measurements on dipole-allowed transitions and will enable in combination with the new multi-purpose ion source [93] and an EBIS many exciting experiments in future which investigate a variety of atomic and nuclear properties. Even a direct determination of the nuclear charge radius becomes possible in frequency measurements of the $2\,^3\mathrm{S}_1 \rightarrow 2\,^3\mathrm{P}_2$ transitions in light helium-like systems [98].

Appendix A

Lineshape simulation

Contributions to the lineshape have been discussed in section 2.4 and are listed in Tab. 2.6. The resulting shape of the pumping and of the probing transition were simulated in the following way:

1. Definition of the frequency array: A frequency array with elements $f_{1,n}$ containing the relevant spectrum is defined. The central element corresponds to the Doppler-shifted resonance frequency f_c. In case of Ca^+, it covered 400 MHz with a step size of 500 kHz. For In^+, a 50 MHz wide array with 1000 elements in a distance of 50 kHz was chosen.

2. Definition of the initial population density: Due to the artificial broadening of the Ca^+ ion source potential, the population density is 1 for an 8-V wide voltage region and 0 outside. For In^+, a part of a 500-MHz wide Gaussian distribution is taken. By shifting the center of the population density relative to the frequency array with the resonant frequency in its center, systematic effects due to optical pumping at the edges of the initial distributions can be investigated.

3. Calculation of the convolution of the initial distribution with the transition lineshape of optical pumping: For each element of the frequency array the transition probability P with the Zeeman-shifted, power-broadened Lorentzians

$$P(n) = N\left(\frac{\Gamma_\mathrm{sat}/(2\pi)}{(f_{1,n}-(f_\mathrm{c}-\frac{1}{2}f_\mathrm{Zeeman}))^2+(\Gamma_\mathrm{sat}/2)^2}+\frac{\Gamma_\mathrm{sat}/(2\pi)}{(f_{1,n}-(f_\mathrm{c}+\frac{1}{2}f_\mathrm{Zeeman}))^2+(\Gamma_\mathrm{sat}/2)^2}\right) \qquad \text{(A.1)}$$

   is calculated and multiplied with the initial population. N is the normalization constant. In case of Ca^+, two Zeeman transitions in a distance of $f_\mathrm{Zeeman} = 440\,\mathrm{kHz}$ are considered whereas 10 transitions in a distance of 180 kHz are applied in a corresponding equation for In^+. After installation of the magnetic shielding (see section 5.1.1), the Zeeman shift was reduced by a factor 10.

4. Calculation of the convolution with the spectral width of the laser for optical pumping: Here, a Gaussian distribution

$$P_\mathrm{G}(n,m) = N\frac{1}{\sigma\sqrt{2\pi}}e^{-\frac{1}{2}\left(\frac{f_{1,n}-f_{2,m}}{\sigma}\right)^2} \qquad \text{(A.2)}$$

   is assumed. The width σ depends on the stabilization scheme and increases by a factor $\sqrt{2}$ during the second harmonic generation process. The convolution is realized by defining a new frequency array of identical size. For each frequency $f_{2,m}$ in this array, P_G is calculated with every frequency $f_{1,n}$ of the former array, multiplied with its corresponding intensity and finally added up.

5. Calculation of the convolution with the noise on the high voltage applied to IR1: Again a Gaussian distribution is assumed which is treated as described in step 4. The impact of the 15-mV ripple in frequency space is calculated with the corresponding differential voltage sensitivity κ yielding 350 kHz for Ca^+ and In^+.

6. Post-acceleration: This is realized by adaption of the frequency array. Each class is transformed first into voltage space

$$U = \frac{mc^2}{2e}\frac{(f_0 - f)^2}{f_0 f} \tag{A.3}$$

   and increased by the post-acceleration voltage. Then it is transformed back into frequency space by using the rest-frame transition frequency f_{0_2} of the probing transition. During this process, the distances of the elements in the array are changed which corresponds to the width compression discussed in section 2.4.6.

7. Calculation of the convolution with the noise on the high voltage applied to IR2: This is carried out similar as in step 5 but with a voltage ripple of 20 mV. Since κ changed due to the post-acceleration and a different transition is used in case of Ca^+, this results in 140 kHz and 300 kHz for Ca^+ and In^+, respectively.

8. Calculation of the convolution with the transition lineshape of the probing transition: This is performed similar as in step 3 but in case of In^+, the power-broadened Lorentzian is replaced with a $\sin^2(x)/x^2$ function to consider the significant transit-time broadening. This is discussed in detail in section 5.3.1.

9. Calculation of the convolution with the spectral width of the probe laser as described in step 4.

A.1 Multiple excitations during optical pumping

In the previous simulation the optical pumping process did not consider multiple excitations. To gain a better understanding of this process, the first steps are modified. In case of Ca^+ ions, the initial 8-eV broad energy distribution is divided in 300 velocity classes. Each class is filled with 25 000 ions and every ion is treated separately.

For each ion, the velocity-dependent transition rate is calculated using Eq. A.1 and excitation is randomized with the respective probability. In case of excitation, the ion returns with a probability 0.93 to the ground state and with 0.07 to the $3d$ level. For those ions that return to the ground state, another possible excitation is simulated until a predefined number of (possible) excitations is reached. This number was varied until the best match with the experimental data was found which occurred for a maximal number of 18 (potential) excitations as described in section 4.2.2. After re-binning, the former simulation is continued with step 4 to compute the resulting lineshape after probing.

In this approach saturation effects due to the decreasing amount of ions in the resonant velocity classes become visible. In particular, this leads to an increased linewidth of the pumping transition. Since the scattering rate for In^+ is several orders of magnitude smaller, only a small amount of ions will interact with the laser more than once during the optical pumping process. Hence, no impact on the lineshape is expected.

Appendix B

Linearity of the scan voltage

The scan voltage is set by the data acquisition system (DAQ) and converted by the 18-bit digital-to-analog converter (DAC) AD5781 from Analog Devices. The voltage signal in the interval from -10 V to $+10$ V is fed into a Kepco BOP500M high-voltage amplifier to generate voltages between -500 V and $+500$ V. Since this amplification factor directly contributes to the determination of the resonant laser frequency when Doppler tuning is applied, it is investigated regularly.

The generated and amplified voltage is measured with a Keysight 3458A voltmeter in dependency of the voltage set by the DAQ. A typical graph is shown in Fig. B.1a. The mean amplification factor of about 50.5 can be determined with an uncertainty of 10^{-5}.

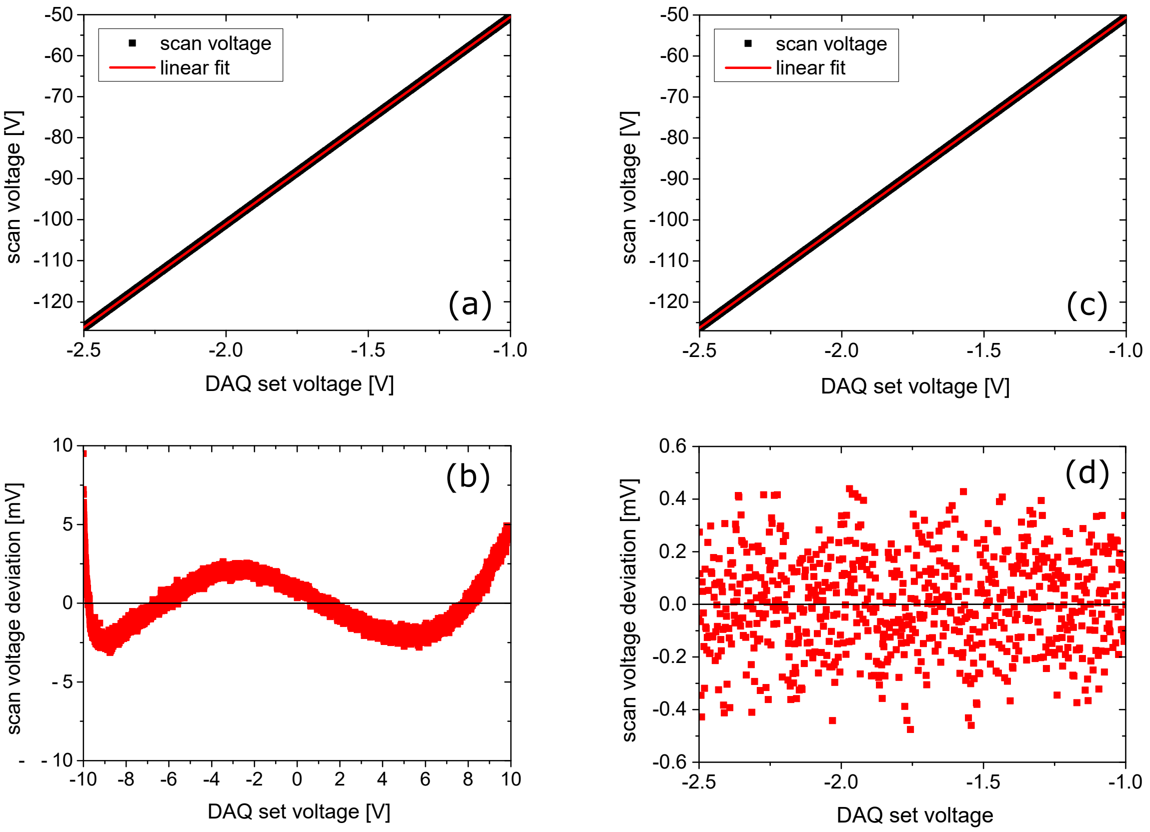

Figure B.1: Investigation of the scan-voltage linearity. (a): Applying voltages from the full range of -10 V to $+10$ V to the high-voltage amplifier and measuring the resulting voltages, yields an amplification factor of about 50.5. When comparing a linear fit to the measured data (b), deviations of up to 3 mV are observed for some DAQ-set voltages. (c): By selecting a region of interest which is defined by the several 10-V (0.2-DAQ-V) broad scan range of the experiment, the deviations can be reduced below 1 mV (d). The remaining fluctuations are caused by the limited resolution of the DAC.

However when looking at the residuals depicted in red underneath, deviations of up to 3 mV are observed for some DAQ set voltages. Since the scan range is usually of the order of a few 10 V (0.2 DAQ-V), a more accurate amplification factor can be determined by fitting only the region of interest as depicted in Fig. B.1b. In this case the deviations shown in the residual underneath are suppressed by one order of magnitude and show no systematic trend. The fluctuations mainly occur due to the limited resolution of the DAC.

The linearity of the scan voltage is investigated regularly and especially during measurement campaigns to avoid systematic uncertainties due to drifts of the amplification factor. As depicted in Fig. B.2, the high-voltage amplifier has shown a significant running-in characteristic since its installation at the end of 2015. In summer 2017 the drift became less intense. This indicates that the electronic components begin to settle but nevertheless, regular investigations of the amplification factor will still be necessary.

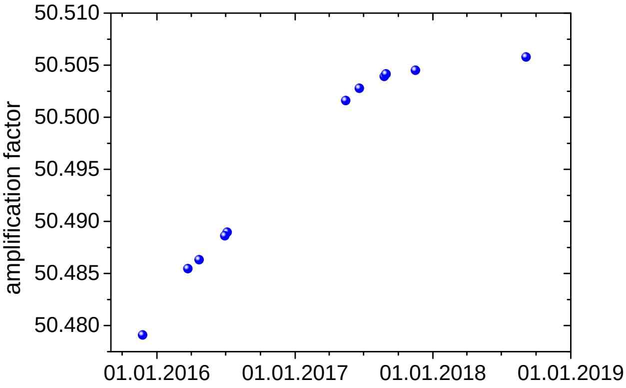

Figure B.2: Changes of the mean amplification factor since installation of the Kepco BOP500M high-voltage amplifier. Due to a significant running-in characteristic, a regular investigation of the linearity is necessary. In summer 2017 the electronic components began to settle decreasing the slope of the drift.

Appendix C

Measurement parameters

For all measurements the first photomultiplier (PMT0) has been used. The relevant parameters of the measurements with Ca^+ and In^+ are:

- Ion current: Measured with a Faraday cup with repeller to suppress secondary electrons at the end of the beamline. Since the ion transmission in the last section of the beamline is 100 %, this corresponds to the ion current inside the interaction regions.
- Laser power: Measured with a Ophir VEGA power meter with a PD300-UV photo diode sensor at the exit window.
- Laser beam size: Measured with a Thorlabs CCD camera beam profilers BC106N-UV/M and BC106N-VIS/M
- Steps: Number of data points per scan.
- Step size: Distance in voltage space between two data points.
- Scans: Number of repetitions of a scan with *steps* · data points.
- Dwell time: Sampling time for each data point at each scan.
- Settling time: Time waited after every change of the scan voltage.

For the determination of the rest-frame transition frequencies of the $5s^2\ ^1S_0 \rightarrow 5s5p\ ^3P_1$ transition in In^+, the collinear measurement was performed in pulsed mode to reduce the laser-induced background rate. Since the dwell time is limited to the short period where the laser light is blocked, several *bunches* were taken before the measurement was continued at the next step. Hence, the total accumulation time is *dwell time* · *bunches* · *scans*.

Table C.1: Parameters of high-voltage measurements with Ca^+ and In^+ ions.

Parameter	Ca^+	In^+
Ion current	0.2 nA	2 nA
Laser power pumping	1.0 mW	0.75 mW
Laser power probing	0.5 mW	0.5 mW
Laser beam size	4 mm^2	2 mm^2
Steps	50	150
Step size	500 mV	2.3 mV
Scans	50	400
Dwell time	50 ms	20 ms
Settling time	2 ms	0.1 ms

Table C.2: Parameters of the rest-frame transition frequency determination of the $5s^2\ ^1S_0 \rightarrow 5s5p\ ^3P_1$ transition in In^+.

Parameter	collinear	anticollinear
Ion current	2 nA	2 nA
Laser power	1.5 mW	0.5 mW
Laser on/off	10/2 µs	-
Laser beam size	2 mm^2	2 mm^2
Steps	75	75
Step size	940 mV	940 mV
Scans	45	250
Dwell time	0.001 ms	20 ms
Bunches	10000	-
Settling time	0.1 ms	0.1 ms

Bibliography

[1] T. Quinn, *From artefacts to atoms: the BIPM and the search for ultimate measurement standards*, Oxford University Press, New York, 2012.

[2] R. Wynands and S. Weyers, *Atomic fountain clocks*, Metrologia **42** (2005), no. 3, 64.

[3] R. Li, K. Gibble, and K. Szymaniec, *Improved accuracy of the NPL-CsF2 primary frequency standard: evaluation of distributed cavity phase and microwave lensing frequency shifts*, Metrologia **48** (2011), no. 5, 283.

[4] C. W. Chou, D. B. Hume, J. C. J. Koelemeij, D. J. Wineland, and T. Rosenband, *Frequency Comparison of Two High-Accuracy* Al^+ *Optical Clocks*, Phys. Rev. Lett. **104** (2010), 070802.

[5] N. Hinkley, J. A. Sherman, N. B. Phillips, M. Schioppo, N. D. Lemke, K. Beloy, M. Pizzocaro, C. W. Oates, and A. D. Ludlow, *An Atomic Clock with* 10^{-18} *Instability*, Science **341** (2013), no. 6151, 1215–1218.

[6] B. J. Bloom, T. L. Nicholson, J. R. Williams, S. L. Campbell, M. Bishof, X. Zhang, W. Zhang, S. L. Bromley, and J. Ye, *An optical lattice clock with accuracy and stability at the* 10^{-18} *level*, Nature **506** (2014), 71–75.

[7] C. W. Chou, D. B. Hume, T. Rosenband, and D. J. Wineland, *Optical Clocks and Relativity*, Science **329** (2010), 1630.

[8] T. Rosenband, D. B. Hume, P. O. Schmidt, C. W. Chou, A. Brusch, L. Lorini, W. H. Oskay, R. E. Drullinger, T. M. Fortier, J. E. Stalnaker, S. A. Diddams, W. C. Swann, N. R. Newbury, W. M. Itano, D. J. Wineland, and J. C. Bergquist, *Frequency Ratio of* Al^+ *and* Hg^+ *Single-Ion Optical Clocks; Metrology at the 17th Decimal Place*, Science **319** (2008), no. 5871, 1808–1812.

[9] G. Bartl, P. Becker, B. Beckhoff, H. Bettin, E. Beyer, M. Borys, I. Busch, L. Cibik, G. D'Agostino, E. Darlatt, M. Di Luzio, K. Fujii, H. Fujimoto, K. Fujita, M. Kolbe, M. Krumrey, N. Kuramoto, E. Massa, M. Mecke, S. Mizushima, M. Müller, T. Narukawa, A. Nicolaus, A. Pramann, D. Rauch, O. Rienitz, C. P. Sasso, A. Stopic, R. Stosch, A. Waseda, S. Wundrack, L. Zhang, and X. W. Zhang, *A new* $^{28}\mathrm{Si}$ *single crystal: counting the atoms for the new kilogram definition*, Metrologia **54** (2017), no. 5, 693.

[10] I. A. Robinson and S. Schlamminger, *The watt or Kibble balance: a technique for implementing the new SI definition of the unit of mass*, Metrologia **53** (2016), no. 5, A46.

[11] J. Kohlmann, R. Behr, and T. Funck, *Josephson voltage standards*, Measurement Science and Technology **14** (2003), no. 8, 1216.

[12] K.-T. Kim, S.-H. Lee, J. K. Jung, and Y. S. Song, *Method to determine the voltage coefficient of a DC high-voltage divider*, IEEE Transactions on Instrumentation and Measurement **52** (2003), no. 2, 469–473.

[13] Th. Thümmler, R. Marx, and Ch. Weinheimer, *Precision high voltage divider for the KATRIN experiment*, New Journal of Physics **11** (2009), no. 10, 103007.

[14] D. H. Kind, W. Lucas, D. Peier, and B. Schulz, *Measurements of High Voltages by Means of Electron Speed Filtering*, IEEE Transactions on Instrumentation and Measurement **32** (1983), no. 8, 8–11.

[15] W. Lucas, *Untersuchung zur Eignung supraleitender Hohlraumresonatoren als Geschwindigkeitsfilter für durch Hochspannung beschleunigte Elektronen*, Ph.D. thesis, TU Braunschweig, 1990.

[16] O. Poulsen, *Velocity and high-voltage measurements using resonant collinear, fast-beam/laser interactions*, Nuclear Instruments and Methods in Physics Research **202** (1982), 503–509.

[17] E. Riis, H. G. Berry, O. Poulsen, S. A. Lee, and S. Y. Tang, *Absolute wavelength measurement and fine-structure determination in* ^{7}Li *II*, Phys. Rev. A **33** (1986), 3023–3028.

[18] O. Poulsen and E. Riis, *Absolute Determination of High Voltages Using Fast-Beam Laser Velocimetry*, Metrologia **25** (1988), no. 3, 147.

[19] S. Götte, K.-M. Knaak, N. Kotovski, H.-J. Kluge, G. Ewald, and K. D. A. Wendt, *Test of collinear spectroscopy for precise high-voltage determination*, Review of Scientific Instruments **75** (2004), no. 4, 1039–1050.

[20] K.-M. Knaak, S. Götte, H.-J. Kluge, G. Ewald, and K.D.A. Wendt, *An evaluation procedure for scanning interferometer based wavemeters*, Optics Communications **231** (2004), no. 1, 1 – 7.

[21] A. Krieger, Ch. Geppert, R. Catherall, F. Hochschulz, J. Krämer, R. Neugart, S. Rosendahl, J. Schipper, E. Siesling, Ch. Weinheimer, D.T. Yordanov, and W. Nörtershäuser, *Calibration of the ISOLDE acceleration voltage using a high-precision voltage divider and applying collinear fast beam laser spectroscopy*, Nuclear Instruments and Methods in Physics Research Section A: Accelerators, Spectrometers, Detectors and Associated Equipment **632** (2011), no. 1, 23 – 31.

[22] E. Will, J. Ullmann, N. Frömmgen, Ch. Geppert, Ch. Gorges, M. Hammen, S. Kaufmann, A. Krieger, and W. Nörtershäuser, *Demonstration of the two-chamber approach for high-voltage measurements using collinear laser spectroscopy*, Hyperfine Interactions **227** (2014), no. 1, 157–168.

[23] K. König, Ch. Geppert, J. Krämer, B. Maaß, E. W. Otten, T. Ratajczyk, and W. Nörtershäuser, *First high-voltage measurements using* Ca^{+} *ions at the ALIVE experiment*, Hyperfine Interactions **238** (2017), no. 1, 24.

[24] J. Krämer, K. König, Ch. Geppert, P. Imgram, B. Maaß, J. Meisner, E. W. Otten, S. Passon, T. Ratajczyk, J. Ullmann, and W. Nörtershäuser, *High-voltage measurements on the 5 ppm relative uncertainty level with collinear laser spectroscopy*, Metrologia **55** (2018), no. 2, 268.

[25] Ch. Weinheimer, *KATRIN, a next generation tritium* β *decay experiment in search for the absolute neutrino mass scale*, Progress in Particle and Nuclear Physics **48** (2002), no. 1, 141 – 150.

[26] O. Rest, *Private communication*, Münster, 2018.

[27] M. Arenz et al., *Calibration of high voltages at the ppm level by the difference of* ^{83m}Kr *conversion electron lines at the KATRIN experiment*, The European Physical Journal C **78** (2018), no. 5, 368.

[28] J. Ullmann, Z. Andelkovic, C. Brandau, A. Dax, W. Geithner, Ch. Geppert, Ch. Gorges, M. Hammen, V. Hannen, S. Kaufmann, K. König, Y. A. Litvinov, M. Lochmann, B. Maaß, J. Meisner, T. Murböck, R. Sánchez, M. Schmidt, S. Schmidt, M. Steck, T. Stöhlker, R. C. Thompson, Ch. Trageser, J. Vollbrecht, Ch. Weinheimer, and W. Nörtershäuser, *High precision hyperfine measurements in Bismuth challenge bound-state strong-field QED*, Nature Communications **8** (2017), 15484.

[29] R. F. Garcia Ruiz, M. L. Bissell, K. Blaum, A. Ekström, N. Frömmgen, G. Hagen, M. Hammen, K. Hebeler, J. D. Holt, G. R. Jansen, M. Kowalska, K. Kreim, W. Nazarewicz, R. Neugart, G. Neyens, W. Nörtershäuser, T. Papenbrock, J. Papuga, A. Schwenk, J. Simonis, K. A. Wendt, and D. T. Yordanov, *Unexpectedly large charge radii of neutron-rich calcium isotopes*, Nature Physics **12** (2016), 594.

[30] A. Krieger, K. Blaum, M. L. Bissell, N. Frömmgen, Ch. Geppert, M. Hammen, K. Kreim, M. Kowalska, J. Krämer, T. Neff, R. Neugart, G. Neyens, W. Nörtershäuser, Ch. Novotny, R. Sánchez, and D. T. Yordanov, *Nuclear Charge Radius of* ^{12}Be, Phys. Rev. Lett. **108** (2012), 142501.

[31] Th. W. Hänsch, *Nobel Lecture: Passion for precision*, Rev. Mod. Phys. **78** (2006), 1297–1309.

[32] Th. Udem, R. Holzwarth, and Th. W. Hänsch, *Optical frequency metrology*, Nature **416** (2002), 233–237.

[33] W. Nörtershäuser, D. Tiedemann, M. Žáková, Z. Andjelkovic, K. Blaum, M. L. Bissell, R. Cazan, G. W. F. Drake, Ch. Geppert, M. Kowalska, J. Krämer, A. Krieger, R. Neugart, R. Sánchez, F. Schmidt-Kaler, Z.-C. Yan, D. T. Yordanov, and C. Zimmermann, *Nuclear Charge Radii of* ^{7,9,10}Be *and the One-Neutron Halo Nucleus* ^{11}Be, Phys. Rev. Lett. **102** (2009), 062503.

[34] A. Krieger, W. Nörtershäuser, Ch. Geppert, K. Blaum, M. L. Bissell, N. Frömmgen, M. Hammen, K. Kreim, M. Kowalska, J. Krämer, R. Neugart, G. Neyens, R. Sánchez, D. Tiedemann, D. T. Yordanov, and M. Zakova, *Frequency-comb referenced collinear laser spectroscopy of* Be$^+$ *for nuclear structure investigations and many-body QED tests*, Applied Physics B **123** (2016), no. 1, 15.

[35] Ph. Imgram, K. König, J. Krämer, T. Ratajczyk, R. A. Müller, A. Surzhykov, and W. Nörtershäuser, *Collinear laser spectroscopy at ion-trap accuracy: Transition frequencies and isotope shifts in the* $6s\,^2S_{1/2} \rightarrow 6p\,^2P_{1/2,3/2}$ *transitions in* Ba$^+$, Phys. Rev. A **99** (2019), 012511.

[36] K. Blaum, *High-accuracy mass spectrometry with stored ions*, Physics Reports **425** (2006), no. 1, 1 – 78.

[37] P. J. Mohr, D. B. Newell, and B. N. Taylor, *CODATA Recommended Values of the Fundamental Physical Constants: 2014*, Journal of Physical and Chemical Reference Data **45** (2016), no. 4, 043102.

[38] M. Herrmann, V. Batteiger, S. Knünz, G. Saathoff, Th. Udem, and T. W. Hänsch, *Frequency Metrology on Single Trapped Ions in the Weak Binding Limit: The* $3s_{1/2} - 3p_{3/2}$ *Transition in* ^{24}Mg$^+$, Phys. Rev. Lett. **102** (2009), 013006.

[39] F. Gebert, Y. Wan, F. Wolf, Ch. N. Angstmann, J. C. Berengut, and P. O. Schmidt, *Precision Isotope Shift Measurements in Calcium Ions Using Quantum Logic Detection Schemes*, Phys. Rev. Lett. **115** (2015), 053003.

[40] C. Shi, F. Gebert, C. Gorges, S. Kaufmann, W. Nörtershäuser, B. K. Sahoo, A. Surzhykov, V. A. Yerokhin, J. C. Berengut, F. Wolf, J. C. Heip, and P. O. Schmidt, *Unexpectedly large difference of the electron density at the nucleus in the* $4p\,^2P_{1/2,3/2}$ *fine-structure doublet of* Ca$^+$, Applied Physics B **123** (2016), no. 1, 2.

[41] H. Guan, Y. Huang, P.-L. Liu, W. Bian, H. Shao, and K.-L. Gao, *Precision spectroscopy with a single* ^{40}Ca$^+$ *ion in a paul trap*, Chinese Physics B **24** (2015), no. 5, 054213.

[42] J. von Zanthier, Th. Becker, M. Eichenseer, A. Yu. Nevsky, Ch. Schwedes, E. Peik, H. Walther, R. Holzwarth, J. Reichert, Th. Udem, T. W. Hänsch, P. V. Pokasov, M. N. Skvortsov, and S. N. Bagayev, *Absolute frequency measurement of the* In$^+$ *clock transition with a mode-locked laser*, Opt. Lett. **25** (2000), no. 23, 1729–1731.

[43] W. Demtröder, *Experimentalphysik 3*, 5th ed., Springer, Heidelberg/Berlin, 2016.

[44] T. Mayer-Kuckuk, *Atomphysik*, 5th ed., Teubner, Stuttgart, 1997.

[45] B. Saleh and M. Teich, *Fundamentals of photonics*, 2nd ed., John Wiley and Sons, Hoboken, 2007.

[46] Ch. Edelmann, *Vakuumphysik*, Spektrum Akademischer Verlag, Heidelberg/Berlin, 1988.

[47] K. Jousten, *Handbook of vacuum technology*, 2nd ed., Wiley-VCH, Weinheim, 2016.

[48] P. A. Tipler and G. Mosca, *Physik*, 7th ed., Springer, Heidelberg/Berlin, 2015.

[49] National Institute of Standards and Technology (NIST), *Atomic Spectra Database*, 2018, https://physics.nist.gov, Last accessed on 2018-10-09.

[50] S. Götte, *Aufbau und Test eines Prototypen zur Messung von Hochspannung mittels kollinearer Spektroskopie*, Ph.D. thesis, Ruprecht-Karls-Universität Heidelberg, 2002.

[51] E. Will, *Hochspannungsmessung mittels kollinearer Laserspektroskopie nach dem Zweikammerprinzip am TRIGA-LASER Experiment*, Diploma thesis, Johannes-Gutenberg Universität Mainz, 2013.

[52] A. Kreuter, C. Becher, G. P. T. Lancaster, A. B. Mundt, C. Russo, H. Häffner, C. Roos, W. Hänsel, F. Schmidt-Kaler, R. Blatt, and M. S. Safronova, *Experimental and theoretical study of the* $3d^2\mathrm{D}$*–level lifetimes of* $^{40}\mathrm{Ca}^+$, Phys. Rev. A **71** (2005), 032504.

[53] W. J. Huang, G. Audi, M. Wang, F. G. Kondev, S. Naimi, and X. Xu, *The AME2016 atomic mass evaluation*, Chinese Physics C **41** (2017), no. 3, 030002.

[54] Y. H. Wang, R. Dumke, J. Zhang, T. Liu, A. Stejskal, Y. N. Zhao, Z. H. Lu, L. J. Wang, Th. Becker, and H. Walther, *Absolute frequency and isotope shift measurements of the cooling transition in singly ionized indium*, European Physical Journal D **44** (2007), 307–311.

[55] P. L. Larkins and P. Hannaford, *Precision energies and hyperfine structures of the* $5s5p\,^3P^0_{0,1,2}$ *and* $5s6s\,^3S_1$ *levels in* In *II*, Zeitschrift für Physik D Atoms, Molecules and Clusters **27** (1993), no. 4, 313–320.

[56] L. J. Curtis, R. Matulioniene, D. G. Ellis, and C. Froese Fischer, *Predictive data-based exposition of* $5s5p^{1,3}P_1$ *lifetimes in the* Cd *isoelectronic sequence*, Phys. Rev. A **62** (2000), 052513.

[57] E. Peik, G. Hollemann, and H. Walther, *Laser cooling and quantum jumps of a single indium ion*, Phys. Rev. A **49** (1994), 402–408.

[58] T. Mehlstäubler, *Private communication*, Braunschweig, 2017.

[59] W. Demtröder, *Laser spectroscopy 1*, 5th ed., Springer, Heidelberg/Berlin, 2014.

[60] P. Imgram, *Accurate isotope shift measurement in the D1 and D2 line of* Ba^+, Master's thesis, TU Darmstadt, 2018.

[61] C. J. Foot, *Atomic Physics*, Oxford University Press, New York, 2005.

[62] W.-L. Zhou, Y. Mori, T. Sasaki, and S. Nakai, *Theoretical Analysis of Multimode Pumped Second-Harmonic Generation*, Japanese Journal of Applied Physics **34** (1995), no. 10R, 5606.

[63] P. Müller, *Simulationen und Analyse systematischer Unsicherheiten des ALIVE Experiments*, Bachelor's thesis, TU Darmstadt, 2017.

[64] N. Frömmgen, *Kollineare Laserspektroskopie an radioaktiven Praseodymionen und Cadmiumatomen*, Ph.D. thesis, Johannes Gutenberg Universität Mainz, 2013.

[65] S. Raeder, *Spurenanalyse von Aktiniden in der Umwelt mittels Resonanzionisations-Massenspektrometrie*, Ph.D. thesis, Johannes Gutenberg Universität Mainz, 2010.

[66] M. J. Copley and T. E. Phipps, *The Surface Ionization of Potassium on Tungsten*, Phys. Rev. **48** (1935), 960–968.

[67] J. Duch, P. Kubisiak, K.H. Adolfsson, M. Hakkarainen, M. Golda-Cepa, and A. Kotarba, *Work function modifications of graphite surface via oxygen plasma treatment*, Applied Surface Science **419** (2017), 439 – 446.

[68] M. Tajmar, I. Vasiljevich, and W. Grienauer, *High current liquid metal ion source using porous tungsten multiemitters*, Ultramicroscopy **111** (2010), no. 1, 1 – 4.

[69] W. Pilz, P. Laufer, M. Tajmar, R. Böttger, and L. Bischoff, *Polyatomic ions from a high current ion implanter driven by a liquid metal ion source*, Review of Scientific Instruments **88** (2017), no. 12, 123302.

[70] G.D. Alton and P.M. Read, *Emittance measurements of gallium liquid-metal ion sources*, Nuclear Instruments and Methods in Physics Research Section B: Beam Interactions with Materials and Atoms **54** (1991), no. 1, 7 – 11.

[71] D. Löffelmacher, J. Adamczewski, A. Stephan, J. Meijer, H. Röcken, H.H. Bukow, and C. Rolfs, *An emittance scanning device for liquid metal ion sources*, Nuclear Instruments and Methods in Physics Research Section B: Beam Interactions with Materials and Atoms **139** (1998), no. 1, 422 – 427.

[72] I. Vasiljevich and M. Tajmar, *The beam divergence of an indium LMIS at a distance of 50 µm as determined by plasma diagnostic measurements*, Ultramicroscopy **111** (2011), no. 8, 969 – 972.

[73] F. Hinterberger, *Physik der Teilchenbeschleuniger und Ionenoptik*, 2nd ed., Springer, Heidelberg/Berlin, 2008.

[74] P. Laufer, *Private communication*, Dresden, 2018.

[75] W. Czarczynski, *Secondary electrons in liquid metal ion sources*, Journal of Vacuum Science & Technology A **13** (1995), no. 1, 113–116.

[76] G. L. R. Mair, *On the role of secondary electrons in liquid metal ion sources*, Journal of Physics D: Applied Physics **30** (1997), no. 5, 921.

[77] P. Käseberg, *Verbesserte Strahlführungskomponenten für das ALIVE-Experiment*, Bachelor's thesis, TU Darmstadt, 2017.

[78] T. Bauer, *Design und Implementation eines ortsauflösenden Faradayschen Bechers*, Bachelor's thesis, TU Darmstadt, 2018.

[79] J. Willmann, *Characterization of a Fluorescence Detection Region for Collinear Laser Spectroscopy*, Bachelor's thesis, TU Darmstadt, 2017.

[80] B. Maaß, K. König, J. Krämer, and W. Nörtershäuser, *Optical Fluorescence Detection for Collinear Laser Spectroscopy using Non-Imaging Optics*, to be published (2019).

[81] H. A. Macleod, *Thin-Film Optical Filters*, 4th ed., CRC Press, Boca Raton, 2010.

[82] A. Krieger, *Laser systems for collinear spectroscopy and the charge radius of* ^{12}Be, Ph.D. thesis, Johannes Gutenberg-Universität Mainz, 2012.

[83] G. D. Boyd and D. A. Kleinman, *Parametric Interaction of Focused Gaussian Light Beams*, Journal of Applied Physics **39** (1968), 3597–3639.

[84] I. Metzler, *Realisierung des gepulsten Pump-Tast-Nachweises für das ALIVE-Experiment*, Bachelor's thesis, TU Darmstadt, 2017.

[85] Tim Ratajczyk, *A Laser System for ALIVE and first High-Voltage Measurements*, Master's thesis, TU Darmstadt, 2016.

[86] Sirah Lasertechnik GmbH, *Matisse 2 TS*, 2018, http://www.sirah.com/laser/cw-ring-lasers/matisse-ts, Last accessed on 2018-10-09.

[87] D. Kabuß, *Digitale Stabilisierung des Lasersystems und der Ionenquelle des ALIVE-Experiments*, Bachelor's thesis, TU Darmstadt, 2018.

[88] C. J. Fall, N. Binggeli, and A. Baldereschi, *Anomaly in the anisotropy of the aluminum work function*, Phys. Rev. B **58** (1998), R7544–R7547.

[89] L. Guo, G. Hua, B. Yang, H. Lu, L. Qiao, X. Yan, and D. Li, *Electron work functions of ferrite and austenite phases in a duplex stainless steel and their adhesive forces with AFM silicon probe*, Scientific Reports **6** (2016), 20660.

[90] C. Gorges, S. Kaufmann, Ch. Geppert, J. Krämer, R. Sánchez, and W. Nörtershäuser, *Status of the TRIGA-LASER experiment*, Hyperfine Interactions **238** (2017), no. 1, 26.

[91] S. Kaufmann, *High precision laser spectroscopy of nickel isotopes at ISOLDE-CERN with a newly developed data acquisition system for collinear laser spectroscopy*, Ph.d. thesis in preparation, TU Darmstadt, 2019.

[92] F. Paschen and J. S. Campbell, *Das erste Funkenspektrum des Indiums* In *II*, Annalen der Physik **423** (1938), no. 1, 29–75.

[93] T. Ratajczyk, V. Varentsov, and W. Nörtershäuser, *Status of a new laser ablation ion beam source for LASPEC*, GSI Scientific Report (2017).

[94] M. Seliverstov, *Highly Efficient Ion Source for Surface and Laser Ionization*, EMIS XVIII conference, Geneva (2018).

[95] G. Vorobjev, A. Sokolov, A. Thorn, F. Herfurth, O. Kester, W. Quint, Th. Stöhlker, and G. Zschornack, *Demonstration of charge breeding in a compact room temperature electron beam ion trap*, Review of Scientific Instruments **83** (2012), no. 5, 053302.

[96] Z. Andelkovic, F. Herfurth, N. Kotovskiy, K. König, B. Maaß, T. Murböck, D. Neidherr, S. Schmidt, J. Steinmann, M. Vogel, and G. Vorobjev, *Beamline for low-energy transport of highly charged ions at HITRAP*, Nuclear Instruments and Methods in Physics Research Section A: Accelerators, Spectrometers, Detectors and Associated Equipment **795** (2015), 109 – 114.

[97] J. Fischer, *Erzeugung hochgeladener Ionen von Bor, Eisen und Antimon für Experimente auf der HITRAP Plattform*, Bachelor's thesis, TU Darmstadt, 2017.

[98] V. A. Yerokhin, Patkóš V., and K. Pachucki, *Relativistic corrections to the Bethe logarithm for the* $2\ ^3S$ *and* $2\ ^3P$ *states of* He, Phys. Rev. A **98** (2018), 032503.

Acknowledgments

The completion of my dissertation would not have been possible without the support of many colleagues and friends.

Especially, I would like to thank Wilfried Nörtershäuser who offered me the opportunity to do my PhD in this exciting field. With all his experience, he was a brilliant adviser who always found the time for fruitful discussions about pressing challenges even at his most busy days.

Most time I spent with Jörg and Phillip in the lab who earn my deepest gratitude. Together we were able to overcome all experimental problems and the atmosphere never became bad although we had to undergo some frustrating experimental periods. It was always a pleasure to work with you!

Nine years ago Bernhard, Tim, Felix and I started together to study physics. During this time we had an incredible amount of fun together and really made it into the same office for our PhD. It would be understatement to say that you are the best colleagues and friends one can wish for.

Besides Bernhard, Tim and Felix, also Daniel, Max, Lydia, Christoph, Tobias and Marc made life and studies in Darmstadt a pleasant and exciting time. Thank you for the uncounted joyful evenings we spent together, the trips and projects we went for and the help in every situation.

Many thanks to all other members of the LaserSpHERe group. The atmosphere was great and there was always an expert for everything who was willing to help. Especially Christian's and Simon's support for urgent TRITON and TILDA problems cannot be overestimated.

I would like to thank Christopher Geppert who developed and designed the basic concept of the ALIVE setup. In our regular meetings he always contributed with his advices to the progress of the experiment.

I also wish to thank Thomas Walther, Robert Roth and Thorsten Kröll that they agreed to take part in my examination.

I would like to acknowledge the assistance and help in a large diversity of different challenges of Dirk Oppermann and Uwe Bonnes and their teams in the mechanical and the electronic workshop.

Thanks should also go to the colleagues at PTB Braunschweig and WWU Münster who gave a lot of advices in the appropriate work with high-voltage dividers and participated at fruitful measuring campaigns in Darmstadt.

Last but not least, I want to thank my family for their love, patience and continuous support over all the years. Thanks a lot.

Curriculum Vitae

Kristian Lars König

born 30.03.1990, Bad Nauheim
Liebfrauenstr. 63
64289 Darmstadt
kkoenig@ikp.tu-darmstadt.de

Graduation

02/2015 - 12/2018	Graduation in the group of Prof. Wilfried Nörtershäuser, Institut für Kernphysik, Technische Universität Darmstadt. Thesis title: *Laser-Based High-Voltage Metrology with ppm Accuracy* Regular participation at experiments at GSI Helmholtzzentrum für Schwerionenforschung Darmstadt and CERN European Organization for Nuclear Research Member of the Sonderforschungsbereich SFB 1245 Member of the Helmholtz Graduate School for Hadron and Ion Research Member of the Graduiertenschule Giersch Awarded with the Giersch-Excellence-Award 2017

University education

10/2009 - 12/2014	Studies of physics, Technische Universität Darmstadt
10/2013 - 12/2014	Master's thesis in the group of Prof. Wilfried Nörtershäuser, GSI Helmholtzzentrum für Schwerionenforschung Darmstadt and Institut für Kernphysik, Technische Universität Darmstadt. Thesis title: *Inbetriebnahme der Niederenergiestrahlstrecke bei HITRAP und erstmaliger Einfang hochgeladener Ionen in der SpecTrap Penningfalle*
09/2012 - 01/2013	Bachelor's thesis in the group of Prof. Thomas Aumann Institut für Kernphysik, Technische Universität Darmstadt. Thesis title: *Teilchen mit Strahlrapidität nach dem R^3B-Reaktionstarget*

School education

06/2009	Abitur at the Sankt-Lioba-Schule, Bad Nauheim

List of publications

Publications in peer-reviewed journals

Ph. Imgram, K. König, J. Krämer, T. Ratajczyk, R. A. Müller, A. Surzhykov, and W. Nörtershäuser, *Collinear laser spectroscopy at ion-trap accuracy: Transition frequencies and isotope shifts in the* $6s\,^2S_{1/2} \rightarrow 6p\,^2P_{1/2,3/2}$ *transitions in* Ba^+, Phys. Rev. A **99** (2019), 012511.

J. Krämer, K. König, Ch. Geppert, P. Imgram, B. Maaß, J. Meisner, E. W. Otten, S. Passon, T. Ratajczyk, J. Ullmann, and W. Nörtershäuser, *High voltage measurements on the 5 ppm relative uncertainty level with collinear laser spectroscopy*, Metrologia **55**, 268 (2018)

S. Schmidt, T. Murböck, Z. Andelkovic, G. Birkl, K. König, W. Nörtershäuser, R. C. Thompson and M. Vogel, *Sympathetic cooling in two-species ion crystals in a Penning trap*, J. Mod. Opt. **65**, 538-548 (2017)

J. Ullmann, Z. Andelkovic, C. Brandau, A. Dax, W. Geithner, C. Geppert, C. Gorges, M. Hammen, V. Hannen, S. Kaufmann, K. König, Y. A. Litvinov, M. Lochmann, B. Maaß, J. Meisner, T. Murböck, R. Sánchez, M. Schmidt, S. Schmidt, M. Steck, T. Stöhlker, R. C. Thompson, C. Trageser, J. Vollbrecht, C. Weinheimer, and W. Nörtershäuser, *High precision hyperfine measurements in Bismuth challenge bound-state strong-field QED*, Nat. Commun. **8**, 15484 (2017)

R. F. Garcia Ruiz, C. Gorges, M. Bissell, K. Blaum, W. Gins, H. Heylen, K. König, S. Kaufmann, M. Kowalska, J. Krämer, P. Lievens, S. Malbrunot-Ettenauer, R. Neugart, G. Neyens, W. Nörtershäuser, D. T. Yordanov and X. F. Yang, *Development of a sensitive setup for laser spectroscopy studies of very exotic calcium isotopes*, J. Phys. G: Nucl. Part. Phys. **44**, 044003 (2017)

Z. Andelkovic, F. Herfurth, N. Kotovskiy, K. König, B. Maaß, T. Murböck, D. Neidherr, S. Schmidt, J. Steinmann, M. Vogel, and G. Vorobjev, *Beamline for low-energy transport of highly charged ions at HITRAP*, Nucl. Instr. Meth. Phys. Res. A 795, 109-114 (2015)

J. Ullmann, Z. Andelkovic, A. Dax, W. Geithner, C. Geppert, C. Gorges, M. Hammen, V. Hannen, S. Kaufmann, K. König, Y. Litvinov, M. Lochmann, B. Maass, J. Meisner, T. Murböck, R. Sánchez, M. Schmidt, S. Schmidt, M. Steck, T. Stöhlker, R. C Thompson, J. Vollbrecht, C. Weinheimer and W. Nörtershäuser, *An improved value for the hyperfine splitting of hydrogen-like* $^{209}\mathrm{Bi}^{82+}$, J. Phys. B: At. Mol. Opt. Phys. **48**, 144022 (2015)

Conference contributions

K. König, C. Geppert, J. Krämer, B. Maaß, E. W. Otten, T. Ratajczyk, and W. Nörtershäuser, *First high-voltage measurements using* Ca^+ *ions at the ALIVE experiment*, Hyperfine Interactions **238**, 24 (2017)

B. Maaß, P. Müller, W. Nörtershäuser, J. Clark, C. Gorges, S. Kaufmann, K. König, J. Krämer, A. Levand, R. Orford, R. Sánchez, G. Savard, and F. Sommer, *Towards laser spectroscopy of the proton-halo candidate boron-8*, Hyperfine Interactions **238**, 25 (2017)

Z. Andelkovic, G. Birkl, S. Fedotova, V. Hannen, F. Herfurth, K. König, N. Kotovskiy, B. Maaß, J. Vollbrecht, T. Murböck, D. Neidherr, W. Nörtershäuser, S. Schmidt, M. Vogel, G. Vorobjev, and C. Weinheimer, *Status of deceleration and laser spectroscopy of highly charged ions at HITRAP*, Hyperfine Interactions **235**, 37 (2015)

R. Sanchez, J. Ullmann, J. Vollbrecht, Z. Andelkovic, A. Dax, W. Geithner, Ch. Geppert, Ch. Gorges, M. Hammen, V. Hannen, S. Kaufmann, K. König, Yu. A. Litvinov, M. Lochmann, B. Maaß, J. Meisner, T. Murböck, W. Nörtershäuser, S. Schmidt, M. Schmidt, M. Steck, Th. Stöhlker, R. C. Thompson, and C. Weinheimer, *Hyperfine Transition in* $^{209}\mathrm{Bi}^{80+}$ *- one step forward*, Phys. Scr. T **166**, 014021 (2015)

J. Vollbrecht, Z. Andelkovic, A. Dax, W. Geithner, C. Geppert, C. Gorges, M. Hammen, V. Hannen, S. Kaufmann, K. König, Y. Litvinov, M. Lochmann, B. Maass, J. Meisner, T. Murboeck, W. Nörtershäuser, R. Sánchez, S. Schmidt, M. Schmidt, M. Steck, T. Stöhlker, R.C. Thompson, J. Ullmann, and C. Weinheimer, *Laser spectroscopy of the ground-state hyperfine structure in H-like and Li-like bismuth*, J. Phys.: Conf. Ser. **583**, 012002 (2015)